Doctoral Dissertation
博士論文

Probing the Early Universe with the Evolution of Primordial Magnetic Fields

(原始磁場の時間発展から探る初期宇宙)

A Dissertation Submitted for the Degree of Doctor of Philosophy

December 2023
令和５年１２月博士（理学）申請

Department of Physics, Graduate School of Science,
The University of Tokyo
東京大学大学院理学系研究科物理学専攻

Fumio Uchida
内田 経夫

Doctoral Dissertation
博士論文

Probing the Early Universe with the Evolution of Primordial Magnetic Fields

(原始磁場の時間発展から探る初期宇宙)

A Dissertation Submitted for the Degree of Doctor of Philosophy

December 2023
令和５年１２月博士（理学）申請

Department of Physics, Graduate School of Science,
The University of Tokyo
東京大学大学院理学系研究科物理学専攻

Fumio Uchida
内田 経夫

Abstract

We study the evolution of primordial magnetic fields until the recombination epoch and apply it to probe the early universe. The evolution of primordial magnetic fields is constrained by the conservation of magnetic helicity density if they are maximally helical and the Hosking integral if they are non-helical. We combine these constraints with another condition, which is obtained by estimating time scales of energy dissipation processes, and describe the evolution of comoving magnetic field strength and comoving magnetic coherence length. We apply the description to discuss the evolution of primordial magnetic fields for representative initial conditions and its implication on magnetogenesis scenarios. If we assume magnetic field generation before the electroweak symmetry breaking, even the strongest magnetic field allowed by the baryon isocurvature constraint turns out to be weaker than the observational lower bound on the intergalactic magnetic fields in voids at the recombination epoch. In contrast, magnetic fields generated in the broken phase of the electroweak symmetry are free from the baryon isocurvature constraint and can be stronger at the recombination epoch. We find that an inflationary magnetogenesis scenario, which realizes reheating temperatures lower than the electroweak scale, can be the origin of the intergalactic magnetic fields. As this example of the application demonstrates, we emphasize that quantitative discussions that relate magnetogenesis scenarios and constraints on primordial magnetic fields at different epochs in the early universe are possible based on the description of the evolution of primordial magnetic fields.

Acknowledgments

I would like to express my greatest gratitude to the advisor, Jun'ichi Yokoyama, for his compassionate guidance and encouragement. Kohei Kamada and Ryusuke Jinno also helped me learn a lot about physics. I am grateful for their tremendous support and education during my Ph.D. course.

Also, I am grateful to the committee members, Masahiro Takada, Aya Bamba, Masahiro Kawasaki, Shigeki Matsumoto, and Yasushi Suto, for their helpful comments on this thesis. I thank all of my collaborators, including Tomohiro Fujita, Motoko Fujiwara, Koichi Miyamoto, Shinji Tsujikawa, Soichiro Yamazaki, Kazuki Yanagihara, and Naoki Yoshida, colleagues at RESCEU and UTAP, and researchers outside, including Mohamed Anber, Axel Brandenburg, Tina Kahniashvili, and Tanmay Vachaspati, for fruitful discussions. I thank the secretaries at RESCEU and the Graduate School of Science for their administrative support. Last but certainly not least, I thank my family and close friends for their moral support. This thesis would not be completed without anyone mentioned above.

The research activity in my Ph.D. course was supported by JSPS DC2 program, JSPS KAKENHI Grant No. JP23KJ0642, and the Forefront Physics and Mathematics Program to Drive Transformation (FoPM).

Contents

Chapter 1

Introduction

The early universe, where the energy scale that governs the physics gets high beyond the accessible range for human beings, has been a crucial field for us to obtain insights into fundamental physics. Today, we have the concordance model of cosmology together with the Standard Model of particle physics, but still have many mysteries left to be explored [1–3]. It is not easy to figure out new physics that solves the mysteries, because the way to observe physical quantities in the early universe is limited. In this regard, thinking about how we can probe the early universe is an issue of generic importance to be addressed.

Indeed, we already have messengers to probe the early universe. Among the most powerful ones are the cosmic microwave background (CMB) [4]. The observation of it enables us to determine the precise values of the cosmological parameters, but we need to go even beyond because the CMB does not carry the information from the early universe before the recombination epoch. Then, if we have another messenger that complements the existing messenger including the CMB photons will help us.

In this regard, cosmological magnetic fields can serve as a promising messenger from the early universe. Recently, gamma-ray observations suggested the existence of the intergalactic magnetic fields in void regions and put lower bounds on their strength [5–17]. In addition, multi-messenger observations have the potential to determine the coherence length of the intergalactic magnetic fields [18]. They can be a messenger from the early universe if we adopt that they have a cosmological origin, as is a reasonable assumption because filling the void regions with magnetic fields by astrophysical mechanisms is not easy [19]. On the theoretical side, various generation mechanisms of those primordial magnetic fields, which involve *e.g.*, the inflation and the phase transitions, have been discussed [20–26]. Therefore, we can potentially get insights into these physics that could have played a role in magnetogenesis in the early universe, by analyzing the properties of the cosmological magnetic fields.

Though we may relate and discuss the observational constraints on the cosmological magnetic fields and their generation mechanisms in the early universe [27,28], quantitative discussions are impossible without understanding the evolution of the cosmological magnetic field. Then, it is necessary to bridge the gap between the primordial magnetic fields and the cosmological magnetic fields in the present universe.

Banerjee and Jedamzik [29] addressed this issue and provided an analytic understanding of the evolution of the cosmological magnetic fields. Their methodology makes the analysis of the complicated magneto-hydrodynamic system surprisingly easy. However, numerical studies [30–36] after Banerjee and Jedamzik have found the so-called inverse transfer of the magnetic energy that is inconsistent with their analysis. Since the inverse transfer makes the decay of the cosmological magnetic fields slower than is previously expected, primordial magnetic fields may remain unexpectedly strong until today. Then, we may wonder whether they contradict the standard cosmology or not. We aim to discuss it quantitatively in this thesis.

A theoretical understanding of the inverse transfer was provided very recently by Hosking and Schekochihin [37], based on the conservation of magnetic helicity. Magnetic helicity is a quantity that measures the parity violation of a magnetic field configuration within a closed volume and is conserved in the limit of large electric conductivity [38]. For maximally helical magnetic fields, *i.e.*, when the magnetic power spectrum maximally violates parity, it has long been known that the conservation of magnetic helicity is directly rephrased as a constraint on the evolution of the magnetic field strength and the coherence length [39]. The constraint, therefore, makes the decay slower, which is nothing but the inverse transfer. For non-helical magnetic fields, *i.e.*, when the magnetic power spectrum is parity even, no direct implication was thought to be obtained because the magnetic helicity is zero independently of the magnetic field strength and the coherence length. However, according to Hosking and Schekochihin [37], the conservation of the Hosking integral, which quantifies the fluctuations of local magnetic helicity, rather than the net magnetic helicity constrains the evolution of the magnetic field strength and the coherence length. The idea well explains the numerical evidence of the inverse transfer of the non-helical magnetic fields and is supported by the dedicated numerical studies [40–42]. Then, one can reformulate the analytic understanding of the evolution of the cosmological magnetic fields based on the conservation of the Hosking integral and a recent idea in plasma physics, namely the role of magnetic reconnection in the decaying magnetic turbulence [43, 44].

The main contribution of this thesis is to provide a new comprehensive description of the evolution of the cosmological magnetic fields, from the epoch of electroweak scale down to the recombination epoch, based on the recent theoretical progress. We first classify the magneto-hydrodynamic system consisting of the primordial magnetic fields and the plasma fluid in the early universe into multiple regimes, according to whether magnetic energy is dominant or not, which conserved quantity plays a crucial role, whether the system is turbulent or not, and more detailed physical pictures of how the energy of the system is dissipated, *i.e.*, what kind of magnetic reconnection transfers the energy and/or whether the shear viscosity is the dominant dissipation term or not. In each regime, we obtain analytic formulas that determine the evolution of the system. We then check the consistency of the results at the boundaries of different regimes. Although the overall picture is quite complicated since we have much more different regimes compared to the previous analysis in Ref. [29], our classification of regimes is still systematic.

By applying the new description of the evolution of the cosmological magnetic fields, we obtain implications on the generation mechanisms of the primordial magnetic fields. In fact, most of the scenarios are inconsistent with the standard cosmology, according to the baryon isocurvature problem [27]. Nevertheless, we have several options to evade the inconsistency, *e.g.*, an inflationary magnetogenesis at very low energy scales even below the electroweak scale $\sim 100\,\mathrm{GeV}$ [28]. Such discussions demonstrate that primordial magnetic fields are useful as a probe in the early universe.

The thesis is organized as follows, mostly based on works accomplished by the author of this thesis in his Ph.D. course [44,45]. His previous work [27] and the work with his collaboration [28] are mentioned as well.

In Chap. 2, we review representative constraints on primordial magnetic fields after overviewing the standard cosmology. In particular, the constraint from the baryon isocurvature problem is introduced, based on our work [27]. The constraints introduced in this chapter are imposed at different epochs in the early universe. To discuss them simultaneously, one should understand the evolution of primordial magnetic fields.

In Chap. 3, we review the basic equations and approaches to solve them to understand the dynamics of the coupled system of magnetic fields and plasma fluids in the early universe. Based on the approximate scaling properties that the equations have and the approximately self-similar decay, we reduce the problem of understanding the evolution of primordial magnetic fields into a following a simpler task. Namely, we just need to understand the evolution of the typical strength and length scale of the magnetic field.

In Chap. 4, we give a description of the scaling evolution of primordial magnetic fields based on our work [44,45]. Several key concepts, *e.g.,* magnetic helicity, Hosking integral, turbulence, and magnetic reconnection, are reviewed as well. We classify the system into sixteen regimes, discuss them piecewise, and check the consistency among them. For the practical purpose, readers who are interested in cosmological implication may skip this chapter and use it as a reference for the next chapter.

Finally before the conclusion (Chap. 6), in Chap. 5, we combine the piecewise analyses and discuss implications on primordial magnetic fields as an application. The content of this chapter is mostly based on our work [44, 45] and includes the discussion on another work [28]. The summary plot of this thesis is Fig. 5.4.

Chapter 2

Standard cosmology and cosmological magnetic fields

In this chapter, we overview the standard cosmology. Although the standard cosmology does not include the cosmological magnetic fields, we have enough reasons to discuss them as they are sometimes called "*the elephant in the room*" [46]. We review the constraints on primordial magnetic fields, including our work [27], to convince readers of the necessity to understand the evolution of primordial magnetic fields.

2.1 Standard Cosmology

In this section, we overview the thermal history of the universe that is established as the standard theory of cosmology, based on Refs. [1–3]. The flat FLRW metric

$$g_{\mu\nu}dx^\mu dx^\nu = dt^2 - a(t)^2 d\boldsymbol{x}^2, \tag{2.1}$$

where t is the cosmic time and $\boldsymbol{x}$ is the comoving spatial coordinate, determines the geometry of the spacetime. The growth of the scale factor $a(t)$ represents the Hubble expansion of the universe. For the later purpose, conformal time τ is introduced so that $dt = ad\tau$. Let us overview what is believed to take place in the history of the universe along the time direction.

Inflation and reheating. Inflationary epoch is the earliest stage that is usually believed to have taken place in the cosmic history. Some mechanism accelerates the expansion of the universe at least for ~ 60 e-folds. Thanks to the sufficiently long period of the accelerated expansion, several problems that would arise in non-inflationary scenarios are avoided. Namely, the accelerated expansion explains the causal connection in the past over the whole observable universe and makes the spacetime extremely close to flat. Also, quantum fluctuations in this epoch can be identified as the seed of the large-scale structure of the universe. Although many models, in which potential energy of a scalar field drives the accelerated expansion, have been proposed and examined under the precise measurements of the cosmic microwave background (CMB) [4], direct clues of the existence of this epoch have not been obtained. One of the unestablished issues in this epoch is the reheating mechanism, which explains the transition to the subsequent radiation-dominated era. Although determination of the reheating temperature $T_{\rm reh}$ is crucial because it sets the initial condition of the radiation-dominated era, the range of allowed reheating temperatures remains wide [47, 48].

Radiation-dominated era. Since the energy density of radiation scales as a^{-4} while that of matter component scales as a^{-3} (both in the physical unit rather than the comoving unit), radiation energy dominates the universe in this early stage of the universe. Radiation temperature T sets the energy scales of the relevant physics. The standard thermal history that includes phase transitions and big-bang nucleosynthesis is established based on the Standard Model of particle physics.

Phase transitions. Assuming the radiation-dominated universe, the electroweak symetry is spontaneously broken at around $T_{\rm EW} \sim 100\,{\rm GeV}$. The notion of primordial magnetic fields has a different meaning above and below $T_{\rm EW}$, because the ordinary electromagnetic ${\rm U}(1)_{\rm EM}$ symmetry is a mixture of the hyper ${\rm U}(1)_Y$ symmetry and the ${\rm SU}(2)_L$ symmetry with the weak mixing angle $\theta_{\rm w0}$. Hereafter, primordial magnetic fields denote both the ${\rm U}(1)_{\rm EM}$ magnetic fields in the symmetry broken phase and the ${\rm U}(1)_Y$ magnetic fields in the symmetry restored phase. At around $T_{\rm QCD} \sim 100\,{\rm MeV}$, the color confinement takes place, which is referred to as the quark-hadron transition.

Big-bang nucleosynthesis. At around $T_{\rm BBN} \sim 0.1\,{\rm MeV}$, the process of synthesizing deuterium from protons and neutrons goes out of equilibrium, and the subsequent network of synthesizing light elements proceeds. The prediction of primordial abundances of light elements is compared with astrophysical observations, and their consistency has been a strong support of the standard cosmology.

Recombination. At around $T_{\rm rec} \sim 0.1\,\mathrm{eV}$, protons and electrons form neutral hydrogen atoms and the universe is neutralized. Photons decouple from the plasma and bring the information at the last scattering surface toward us. This is what we observe as the CMB, and its feature, which turned out to be consistent with the standard cosmology, has been another strong support.

Just before the recombination epoch, the matter components begin to dominate the energy density of the universe. In the matter-dominated universe, density fluctuations of matter components grow, and the large-scale structure of the universe develops. In this thesis, we refer to the universe before the recombination epoch as the early universe and limit ourselves to discussing the early universe only.

2.2 Primordial magnetic fields

In this section, we review the possible roles of primordial magnetic fields, based on Ref. [49], in connection with different epochs mentioned in the previous section 2.1 and introduce a severe theoretical constraint on the primordial magnetic fields, based on our work [27]. We first introduce the concept of a stochastic magnetic field (Sec. 2.2.1), review the observational constraints on primordial magnetic fields (Sec. 2.2.2), and explain the theoretical constraint (Sec. 2.2.3).

2.2.1 Stochastic magnetic fields

Since magnetic fields are fields of a three-vector, it locally breaks the isotropy. On the other hand, the cosmological principle suggests that the universe is homogeneous and isotropic on large scales. In this section, we explain how the anisotropy on small scales and isotropy on large scales hold at the same time. The discussion is general for any epoch in the history of the universe.

We introduce a length scale, $\xi_{\rm M}$, that is characteristic to the magnetic field configuration in the universe. It separates length scales into anisotropic and isotropic regimes in the following sense. Within the scale $\xi_{\rm M}$, magnetic fields are almost coherent with the same amplitudes $\sim B$ and the same direction. Therefore, on smaller scales, it looks anisotropic. On the other hand, on larger scales, many coherent patches are contained. If the direction of magnetic fields is assigned randomly to each patch, they look isotropic as a whole. Panel (a) of Fig. 3.1 in the next chapter may be helpful to understand this stochastic nature of magnetic fields.

The randomness of possible magnetic field configurations is supposed to follow some probability distribution. The homogeneity of the universe implies that the probability distribution is identical for every coherent patch. Then, the isotropy at large scales is rephrased as

$$\langle \boldsymbol{B}(\boldsymbol{x}) \rangle = 0, \tag{2.2}$$

where the angle bracket implies taking an ensemble average. According to this line of thinking, we are rather interested in the probability distribution of possible magnetic field configurations than just one realization, $\boldsymbol{B}(\boldsymbol{x})$. The probabilistic property is described by moments of magnetic fields. The first moment vanishes as Eq. (2.2) implies. Then, the second moments or, equivalently, the power spectra are of our interest, which will be introduced in Sec. 3.2.1. The coherence length ξ_{M} and the typical strength B of magnetic fields, which we introduced only conceptually in this section, are defined there in terms of the power spectra.

2.2.2 Observational constraints

In this section, we review the observational bounds on primordial magnetic fields, based on Ref. [49]. Both upper and lower bounds have been established. On one hand, CMB observations are consistent with zero magnetic fields and put upper bounds on their strength. On the other hand, observations of the intergalactic magnetic fields in voids can be interpreted as lower bounds on their strength, assuming that the primordial magnetic fields survive until today without being affected by astrophysical mechanisms in the late universe.

CMB upper bounds. The contribution of primordial magnetic fields as corrections of the CMB spectrum is estimated by comparing their energy density with that of the thermal radiation energy density. Then, primordial magnetic fields with the comoving strength $B \sim 10^{-8}\,\mathrm{G}$ above the CMB scale $\sim 10^{-3} H_0^{-1}$, where $H_0^{-1} \sim 4\,\mathrm{Gpc}$ is the present Hubble horizon, are expected to introduce significant corrections to the 10^{-5} order CMB temperature anisotropy. In addition, primordial magnetic fields at the characteristic scale $\sim 100\,\mathrm{pc}$ for the freezeout of the double-Compton scattering are expected to distort the background thermal spectrum [50]. In Fig. 2.3, we show the upper limits from the non-detection of these imprints on the CMB spectrum (gray-shaded regions).

Blazar lower bound. Gamma-ray observations have found energy spectra of TeV blazars that are consistent with the intergalactic magnetic fields in void regions [5–18]. TeV photons from distant blazars (second left panel of Fig. 2.1) are believed to experience a cascade process (leftmost panel of Fig. 2.1), in which some portion of their energy is transferred to secondary GeV photons (second right panel of Fig. 2.1). However, observations suggest that GeV flux is smaller than expected (rightmost panel of Fig. 2.1). This lack of secondary GeV photons is attributed to the intergalactic magnetic fields in void regions that bend paths of electron-positron pairs in the intermediate stage of the cascade process [5, 6, 8–13, 15–17]. The lower bounds in the literature differ by a few magnitudes because it is sensitive to the activity duration of the blazars. Closely related effects of the intergalactic magnetic fields are discussed in Refs. [7, 14, 18]. For more explanation, see Appendix B. To be conservative, the latest lower bound is [17]

$$B \gtrsim \begin{cases} 1.8 \times 10^{-17}\,\mathrm{G}, & \xi_\mathrm{M} > 0.2\,\mathrm{Mpc} \\ 1.8 \times 10^{-17}\,\mathrm{G} \left(\dfrac{\xi_\mathrm{M}}{0.2\,\mathrm{Mpc}} \right)^{-\frac{1}{2}}, & \xi_\mathrm{M} < 0.2\,\mathrm{Mpc}, \end{cases} \tag{2.3}$$

which is shown as the pink-hatched exclusion in Fig. 2.3. The constraint could become severer, if we better understand the intrinsic nature of blazars and the extragalactic background light [16, 18].

The former bounds are imposed on the magnetic field evaluated at the recombination epoch, and the latter ones are at the present universe. However, since the charged plasma disappears at recombination, we assume that the magneto-hydrodynamic evo-

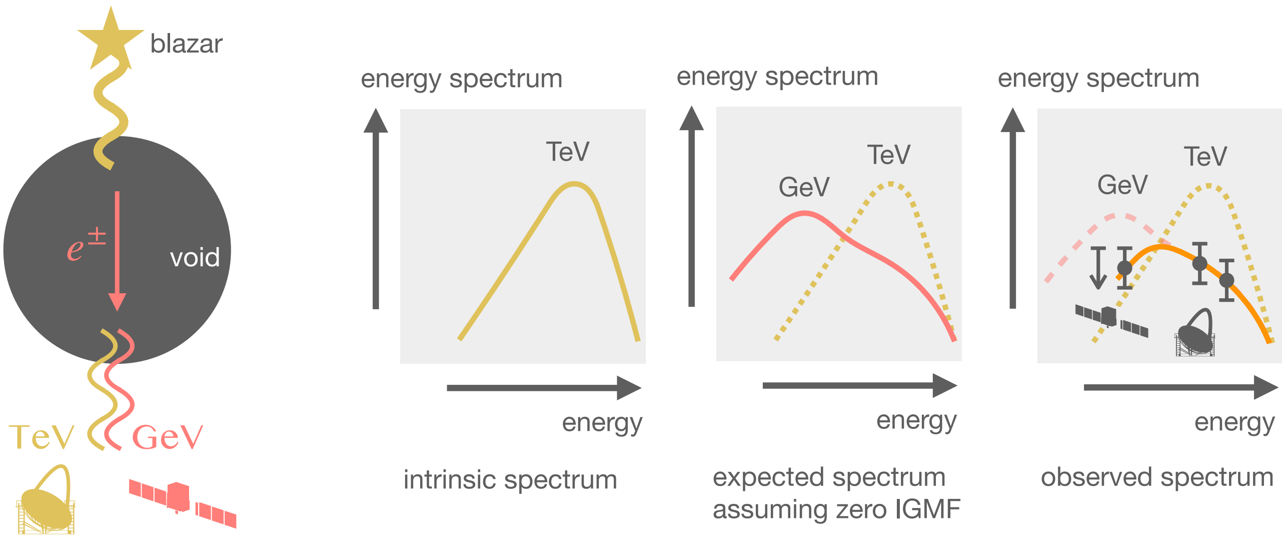

Figure 2.1: The observational evidence of the intergalactic magnetic fields in voids. Leftmost: The cascade process transfers the energy of TeV photons emitted by blazars into electron-positron pairs and finally into GeV photons before they are observed by gamma-ray telescopes. Second left: The intrinsic spectrum is assumed to have a peak at TeV range. Second right: The spectrum after the cascade process is expected to have a peak at GeV range. Right: Suppression of the observed GeV photons is interpreted as the evidence of the intergalactic magnetic fields in voids, which bend the paths of electron-positron pairs [5, 6, 8–13, 15–17].

lution of the magnetic field is negligible in the late universe [49]. Therefore, both of these CMB and blazar bounds can be compared directly as in Fig. 2.3.

2.2.3 Baryon isocurvature problem

If we interpret the blazar lower bound as the bound on primordial magnetic fields and accept that they are generated in the early universe, we can use the bound to discuss their possible generation mechanisms. Mechanisms at the inflation and reheating [20–22] are popular options, but they typically suffer from a serious problem. In this section, we introduce two closely related constraints, based on Refs. [51, 52] and our work [27].

Let us assume the magnetic field generation above the electroweak scale, as is a standard idea for the inflationary magnetogensis scenarios. Then, primordial magnetic fields are originally of the $\mathrm{U}(1)_Y$-type. The electroweak symmetry breaking changes the original field configuration to the resultant $\mathrm{U}(1)_{\mathrm{em}}$ magnetic field.

Baryon overproduction problem. For now, suppose that the magnetic field configuration maximally violates parity. Such a magnetic field is called maximally-helical. Then, a possibility of generating baryon asymmetry of the universe arises because Sakharov's conditions [53] are satisfied. Baryon number is not a conserved quantity due to the chiral anomaly, the parity-violating magnetic field violates CP symmetry, and the existence of the magnetic field implies a deviation from a thermal equilibrium. Indeed, the transition from the $\mathrm{U}(1)_Y$ magnetic field to the $\mathrm{U}(1)_{\mathrm{em}}$ magnetic field during the electroweak symmetry breaking generates the resultant baryon asymmetry of the universe [27, 52]

$$\langle \eta_B \rangle \sim 10^{-10} \left(\frac{B(T_{\mathrm{EW}})}{10^{-13}\,\mathrm{G}} \right)^2 \left(\frac{\xi_{\mathrm{M}}(T_{\mathrm{EW}})}{10^{-16}\,\mathrm{Mpc}} \right), \tag{2.4}$$

where the baryon-to-entropy ratio, $\eta_B := n_B/s$, is the baryon number density divided by the entropy density, and 10^{-10} is its observed value [4]. Note that the rate of baryon number generation is sensitive to the details of the electroweak symmetry breaking, and the coefficient of Eq. (2.4) is as well. The reference values of B and ξ_{M} in the equation have no physical meanings beyond just references. Therefore, primordial magnetic fields stronger than values determined by Eq. (2.4) $\sim 10^{-10}$ results in baryon overproduction [52].

Baryon isocurvature problem. While the baryon overproduction problem applies only to parity-violating primordial magnetic fields, primordial magnetic fields generally suffer from another problem. In analogy with the discussion about isotropy in Sec. 2.2.1, magnetic fields configuration always violates parity within local patches of the universe because of the stochastic property of primordial magnetic fields. Then, local production of baryons or antibaryons is expected at the electroweak symmetry breaking. The spatial distribution of baryons becomes $\eta_B = 10^{-10} + \delta\eta_B$, where the baryon isocurvature perturbations evaluated at the big-bang nucleosynthesis is estimated as [27]

$$\sqrt{\left\langle \left(\frac{\delta\eta_B}{10^{-10}}\right)^2 \right\rangle}(T_{\rm BBN}) \sim \left(\frac{B(T_{\rm EW})}{10^{-13}\,{\rm G}}\right)^2 \left(\frac{\xi_{\rm M}(T_{\rm EW})}{10^{-16}\,{\rm Mpc}}\right)$$
$$\times\,(\text{relative amplitude of undamped modes}), \qquad (2.5)$$

where the last factor accounts for the suppression due to the neutron diffusion. As Fig. 2.2 explains, when the magnetic coherence length $\xi_{\rm M}$ is smaller than the neutron diffusion scale, the dominant component of the baryon isocurvature perturbations at the scale $\xi_{\rm M}$ is exponentially damped at the epoch of big-bang nucleosynthesis. However, mode-couplings of the magnetic field fluctuations generate large-scale baryon isocurvature perturbations, which are subdominant but remain undamped. The suppression factor picks out the contribution from such undamped modes. For a monochromatic magnetic energy spectrum, the suppression factor is estimated as [27]

$$(\text{relative amplitude of undamped modes}) \sim \frac{\xi_{\rm M}}{10^{-9}\,{\rm Mpc}}, \qquad (2.6)$$

where the scale 10^{-9} Mpc is the characteristic neutron diffusion length at the big-bang nucleosynthesis [54]. From these estimates, strong primordial magnetic fields above the blue-hatched region in Fig. 2.3 turn out to result in large baryon isocurvature perturbations that affect big-bang nucleosynthesis, which is constrained as Eq. (2.5) $\lesssim$ 0.016 [55] by the second order effect of the baryon isocurvature perturbation on the observed abundance of primordial deuterium. Then, we obtain a general constraint [27]

$$\left(\frac{B(T_{\rm EW})}{10^{-13}\,{\rm G}}\right)\left(\frac{\xi_{\rm M}(T_{\rm EW})}{10^{-13}\,{\rm Mpc}}\right) \lesssim 1 \qquad (2.7)$$

at small scales. In Fig. 2.3, we show the baryon isocurvature constraint on primordial magnetic fields evaluated at the electroweak scale (blue-hatched region). For more explanation, see Appendix C.

These constraints, together with the observational ones, on primordial magnetic fields motivate us to discuss their evolution because constraints at different epochs in the history of the universe cannot be compared altogether unless we understand their evolution.

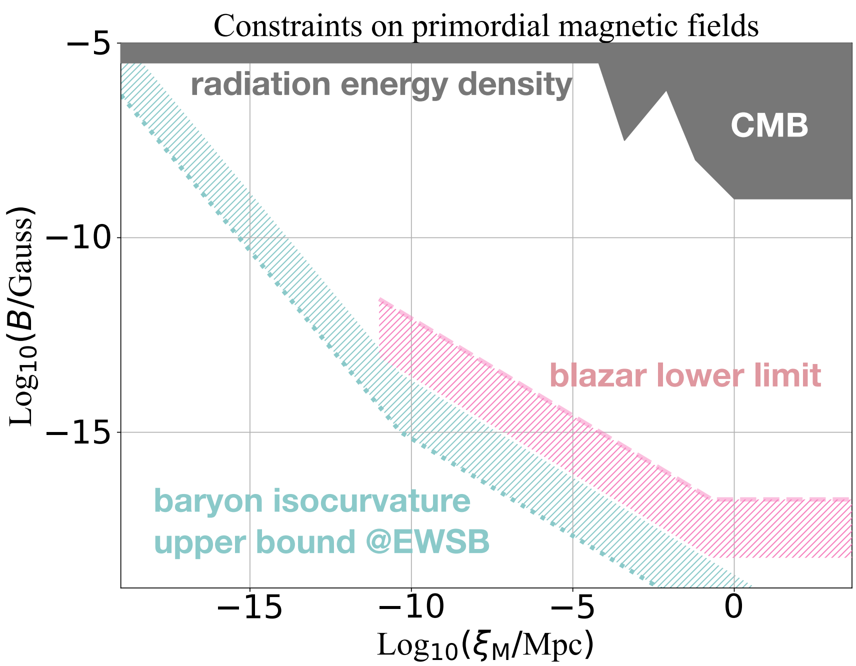

Figure 2.3: Constraints on the comoving strength and the coherence length of primordial magnetic fields. CMB upper bounds imposed in the recombination epoch (gray-shaded) [56], the blazar lower bound imposed in the present universe (pink-hatched) [17], and the baryon isocurvature constraint imposed at the electroweak symmetry breaking (blue-hatched) [27].

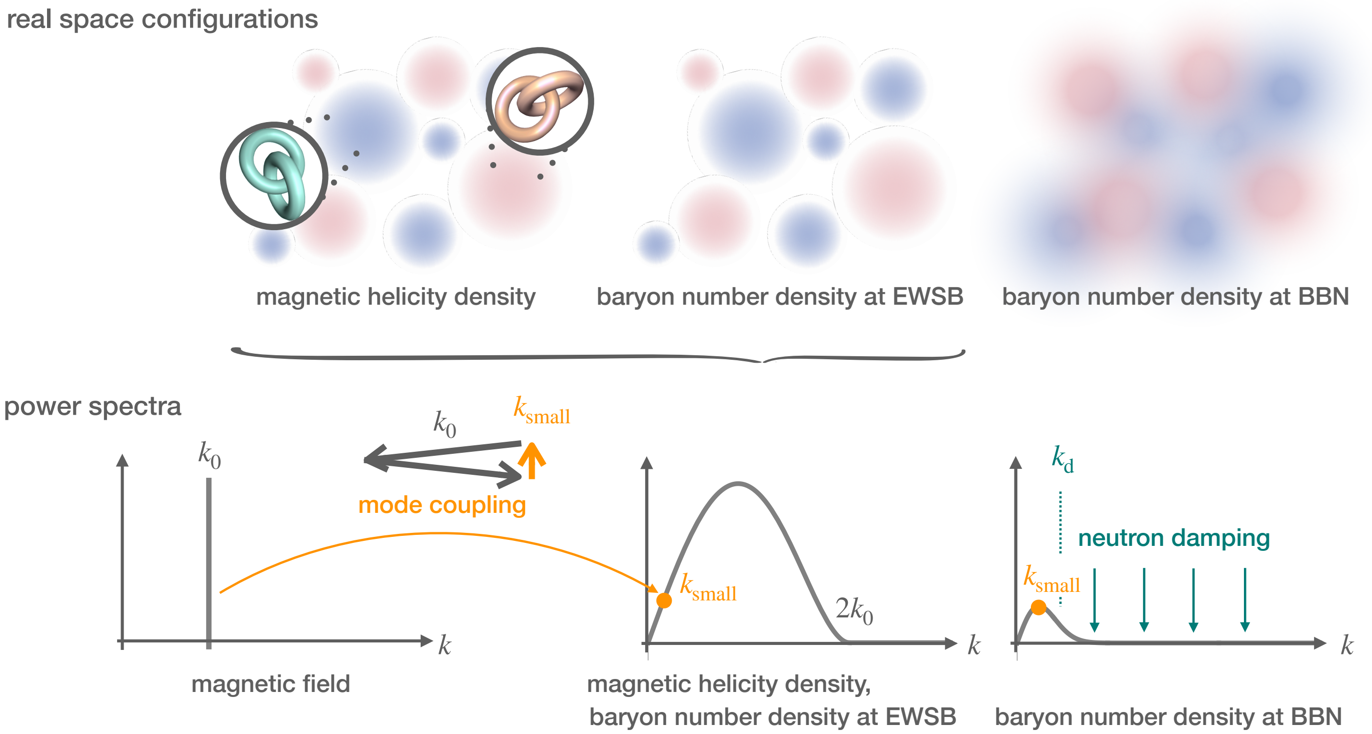

Figure 2.2: The mechanism of baryon isocurvature constraint for small magnetic coherence length. Top left: Magnetic helicity density has spatial fluctuation. Top middle: Magnetic helicity density generates baryons during the electroweak symmetry breaking (EWSB), and baryon isocurvature perturbations are generated. Top right: By the big-bang nucleosynthesis, neutrons diffuse and the baryon isocurvature perturbations are suppressed at small scales. Bottom Left: Suppose that the magnetic field is localized at a scale k_0. Bottom middle: Although the spectra of magnetic helicity density and the baryon number density just after the EWSB has a peak around $\sim k_0$, they have a large-scale component at $k_{\rm small} \ll k_{\rm d}$, where $k_{\rm d} \sim (10^{-9}\,{\rm Mpc})^{-1}$ is the neutron diffusion scale, because of the mode-coupling. Bottom right: Baryon number density at small scale $k \gg k_{\rm d}$ is exponentially damped at the big-bang nucleosynthesis, but the mode at $k_{\rm small}$ still survives and affects big-bang nucleosynthesis [27].

Chapter 3

Scaling solutions of magneto-hydrodynamics

In this chapter, we review the formulation of the magneto-hydrodynamics in the expanding universe, mostly based on Ref. [57]. It has long been known that the set of equations has the invariance under rescalings of the relevant quantities in the ideal MHD limit. Based on that, the evolution of the system is commonly projected onto only a few parameters, even when the scaling property is broken by the non-ideal terms.

3.1 Basic equations

We describe the coupled system of primordial magnetic fields and the fluid consisting of the Standard Model particles in the expanding universe. Schematically, the dynamics of the system is governed by the following three factors.

One is the expansion of the universe, which is accounted for by the following rescaling of the physical quantities into the comoving quantities [57]:

$$\begin{aligned} \boldsymbol{B} = a^2 \boldsymbol{B}_{\mathrm{p}}, \quad \boldsymbol{v} = \boldsymbol{v}_{\mathrm{p}}, \quad \rho = a^4 \rho_{\mathrm{p}}, \quad p = a^4 p_{\mathrm{p}}, \\ \sigma = a\sigma_{\mathrm{p}}, \quad \eta = a^{-1}\eta_{\mathrm{p}}, \quad \alpha = a\alpha_{\mathrm{p}}, \end{aligned} \tag{3.1}$$

where the subscript $_{\mathrm{p}}$ denotes physical quantities. Hereafter, $\boldsymbol{B}$ denotes the comoving magnetic field, $\boldsymbol{v}$ the comoving velocity of the fluid motion[1], ρ and p the comoving energy density and the pressure of the fluid, respectively, and σ, η, and α the comoving transport coefficients.

[1] Note that $v := dx/d\tau$ and $v_{\mathrm{p}} := (adx)/dt = (adx)/(ad\tau) = dx/d\tau = v$.

The other two factors are the equations of motion for the comoving magnetic field $\boldsymbol{B}$ and the comoving velocity field $\boldsymbol{v}$. The equation of motion for the comoving magnetic field is the induction equation,

$$\partial_\tau \boldsymbol{B} - \boldsymbol{\nabla} \times (\boldsymbol{v} \times \boldsymbol{B}) = \frac{1}{\sigma}\nabla^2 \boldsymbol{B}, \tag{3.2}$$

and the one for the comoving velocity field is the Navier–Stokes equation,

$$\partial_\tau \boldsymbol{v} + (\boldsymbol{v} \cdot \boldsymbol{\nabla})\boldsymbol{v} - \frac{1}{\rho + p}(\nabla \times \boldsymbol{B}) \times \boldsymbol{B} + \frac{\boldsymbol{\nabla}\delta p}{\rho + p} = \eta \left[\nabla^2 \boldsymbol{v} + \frac{1}{3}\boldsymbol{\nabla}(\boldsymbol{\nabla} \cdot \boldsymbol{v})\right] - \alpha \boldsymbol{v}, \tag{3.3}$$

from which the expansion of the universe is apparently decoupled [29, 57]. Since the energy density and the pressure have their homogeneous contribution as the background, we denote their perturbations by $\delta\rho$ and δp and distinguish them from the background component. While the terms except the ones with ∂_τ in the left hand sides of these equations transfer comoving energy density between the magnetic field and the fluid, the terms in the right hand sides dissipate the energy away from the system. The comoving electric conductivity, $\sigma \sim 10^{-15--11}\,\mathrm{GeV}$, and the comoving shear viscosity, $\eta \sim 10^{+15-+25}\,\mathrm{GeV}^{-1}$, dissipate the energy of colliding particles of the fluid into heat. The comoving coefficient of the drag force, $\alpha \sim 10^{-40--20}\,\mathrm{GeV}$, dissipates the energy of the system, also, and has contributions from the friction of the fluid with free-streaming particles as a background of the fluid motion and from the Hubble expansion in the matter-dominated era. For more precise values of these dissipation coefficients, see Appendix A. The continuity equation

$$\partial_\tau \delta\rho + \boldsymbol{\nabla} \cdot [(\rho + p)\boldsymbol{v}] = \boldsymbol{E} \cdot (\boldsymbol{\nabla} \times \boldsymbol{B}), \tag{3.4}$$

where

$$\boldsymbol{E} = \left(\frac{1}{\sigma}\boldsymbol{\nabla} - \boldsymbol{v}\right) \times \boldsymbol{B}, \tag{3.5}$$

and the equation of state, $\delta p = w\delta\rho$, close the equations of motions. We assume $w = 1/3$ in the radiation dominated universe and $w = 0$ in the matter dominated universe. Here the fluid motion is the macroscopic motion of fluid particles, including photons when they are tightly coupled with the fluid. However, we assume that density perturbations of the fluid do not have a significant impact on the dynamics governed by the magnetic and velocity fields unless their relevant length scales are as large as the Jeans scale ($\sim$ the horizon scale in the radiation-dominated era).

3.2 Self-similar decay

As is explained in Sec. 2.2.1, we are interested in the stochastic properties of magnetic and velocity fields rather than their precise configurations in the real space. To describe their stochastic properties, we define power spectra in the Fourier space and discuss how they decay in time.

3.2.1 Power spectra

Let us start by defining the magnetic and velocity energy spectra. By assuming the homogeneity and isotropy of the ensemble averages, the power spectra of the magnetic and velocity fields, $P_B(\tau, k)$ and $P_v(\tau, k)$, are defined as

$$\langle \boldsymbol{B}(\boldsymbol{k}) \cdot \boldsymbol{B}(\boldsymbol{k}') \rangle = (2\pi)^3 \delta^3(\boldsymbol{k} + \boldsymbol{k}') P_B(\tau, k), \tag{3.6}$$

$$\langle \boldsymbol{v}(\boldsymbol{k}) \cdot \boldsymbol{v}(\boldsymbol{k}') \rangle = (2\pi)^3 \delta^3(\boldsymbol{k} + \boldsymbol{k}') P_v(\tau, k), \tag{3.7}$$

where $\boldsymbol{B}(\boldsymbol{k})$ and $\boldsymbol{v}(\boldsymbol{k})$ denote Fourier modes of the fields with the convention

$$f(\boldsymbol{k}) := \int d^3x e^{-i\boldsymbol{k}\cdot\boldsymbol{x}} f(\boldsymbol{x}), \quad f(\boldsymbol{x}) = \int \frac{d^3k}{(2\pi)^3} e^{i\boldsymbol{k}\cdot\boldsymbol{x}} f(\boldsymbol{k}), \tag{3.8}$$

for a general field f. In terms of these power spectra, we define the typical magnetic field strength, B, the magnetic coherence length, ξ_{M}, the typical velocity, v, and the kinetic coherence length, ξ_{K}, as

$$B(\tau)^2 := \langle \boldsymbol{B}(\boldsymbol{x})^2 \rangle = \int \frac{d^3k}{(2\pi)^3} P_B(\tau, k), \quad \xi_{\mathrm{M}}(\tau) := \frac{1}{B^2} \int \frac{d^3k}{(2\pi)^3} \frac{2\pi}{k} P_B(\tau, k), \tag{3.9}$$

$$v(\tau)^2 := \langle \boldsymbol{v}(\boldsymbol{x})^2 \rangle = \int \frac{d^3k}{(2\pi)^3} P_v(\tau, k), \qquad \xi_{\mathrm{K}}(\tau) := \frac{1}{v^2} \int \frac{d^3k}{(2\pi)^3} \frac{2\pi}{k} P_v(\tau, k). \tag{3.10}$$

In particular, we rewrite the first equations in Eqs. (3.9) and (3.10) as

$$\frac{d\rho_{\mathrm{M}}}{d\log k} := \frac{k^3}{4\pi^2} P_B(\tau, k), \tag{3.11}$$

$$\frac{d\rho_{\rm K}}{d\log k} := (\rho + p)\frac{k^3}{4\pi^2}P_v(\tau, k), \tag{3.12}$$

where the left hand sides can be identified as the spectra of the energy densities of the magnetic and velocity fields

$$\rho_{\rm M} := \frac{1}{2}B^2, \quad \rho_{\rm K} := \frac{\rho + p}{2}v^2 \tag{3.13}$$

in the Fourier space.

Equations (3.11) and (3.12) imply that the energy spectra of the magnetic and velocity fields are roughly proportional to $k^3 P_B(k)$ and $k^3 P_v(k)$. In panel (b) of Fig. 3.1, we plot the magnetic energy spectrum (red solid line). The shape of the spectra is typically peaky, which may be approximated by a broken power law at around the peak (red dot). Then, up to numerical factors, one can read off the typical strength squared B^2 and the coherence length $\xi_{\rm M}$ of the magnetic field from the location of the peak. The numerical factors depend on the power-law indices on both sides of the peak, and they are typically of the order of unity. In a parallel way, as for the velocity field, the peak of the energy spectrum $k^3 P_v(k)$ is located at around the wavenumber corresponding to the coherence length $\xi_{\rm K}$ and the height $(\rho + p)v^2$.

For the later purpose, we would like to generalize the definition (3.6) by introducing the parity odd part of the power spectrum, $A_B(\tau, k)$, as

$$\langle B_i(\boldsymbol{k})B_j(\boldsymbol{k}')\rangle = (2\pi)^3\delta^3(\boldsymbol{k} + \boldsymbol{k}')\left(\frac{\delta_{ij} - \hat{k}_i\hat{k}_j}{2}P_B(\tau, k) - \frac{i\epsilon_{ijl}\hat{k}_l}{2}A_B(\tau, k)\right), \tag{3.14}$$

where $\hat{\boldsymbol{k}} := \boldsymbol{k}/k$ is the unit vector in the direction of $\boldsymbol{k}$. This form is general for homogeneous, isotropic, and solenoidal magnetic fields [49]. One may further introduce the power spectrum of the vector potential $\boldsymbol{A}$ as well. Let us impose the Coulomb gauge condition, $\boldsymbol{\nabla}\cdot\boldsymbol{A} = 0$, and then $\boldsymbol{A}(\boldsymbol{k}) = i\boldsymbol{k}\times\boldsymbol{B}(\boldsymbol{k})/k^2$ holds. By assuming the expression in Eq. (3.14) for the magnetic power spectrum, we obtain

$$\langle \boldsymbol{A}(\boldsymbol{k})\rangle = 0, \tag{3.15}$$

$$\langle A_i(\boldsymbol{k})B_j(\boldsymbol{k}')\rangle = i\epsilon_{ipq}k_p k^{-2}\langle B_q(\boldsymbol{k})B_j(\boldsymbol{k}')\rangle, \tag{3.16}$$

$$\langle A_i(\boldsymbol{k}) A_j(\boldsymbol{k}')\rangle = k^{-2}\langle B_i(\boldsymbol{k}) B_j(\boldsymbol{k}')\rangle. \tag{3.17}$$

In particular, Eqs. (3.15) and (3.17) imply that the vector potential is also homogeneous and isotropic in the Coulomb gauge. This feature makes the computation in Sec. 4.2.2 easier [27, 40], although all the results are independent of the gauge choice. Finally, we need to mention one more thing. If we regard $\langle \boldsymbol{A}\cdot\boldsymbol{B}\rangle$ as the inner product of $\boldsymbol{A}$ and $\boldsymbol{B}$, then Schwarz inequality implies [39, 58]

$$|A_B(\tau,k)| \leq P_B(\tau,k), \tag{3.18}$$

which is often called the realizability condition. This condition implies the notion of maximally parity-violating configuration, corresponding to the saturation of the inequality. We will encounter essentially the same inequality again in Sec. 4.2.1.

3.2.2 Scaling property

Since the magnetic field energy is dissipated in time, the magnetic energy spectrum decays downward in the ξ_{M}-B plain. (panel (c) in Fig. 3.1), basically. One of the key concepts to understand the decay laws is the scaling property of the set of equations (3.2), (3.3), and (3.4). If we rescale the variables by an arbitrary constant parameter λ as [59]

$$\begin{aligned}
\boldsymbol{x} \to \boldsymbol{x}' &:= \lambda \boldsymbol{x}, \quad \tau \to \tau' := \lambda^{1-r}\tau,\\
\boldsymbol{v} \to \boldsymbol{v}'(\tau',\boldsymbol{x}') &:= \lambda^{r}\boldsymbol{v}(\tau,\boldsymbol{x}), \quad \boldsymbol{B} \to \boldsymbol{B}'(\tau',\boldsymbol{x}') := \lambda^{r}\boldsymbol{B}(\tau,\boldsymbol{x}),\\
\delta p \to \delta p'(\tau',\boldsymbol{x}') &:= \lambda^{2r}\delta p(\tau,\boldsymbol{x}), \quad \delta\rho \to \delta\rho'(\tau',\boldsymbol{x}') := \lambda^{2r}\delta\rho(\tau,\boldsymbol{x}),
\end{aligned} \tag{3.19}$$

equations for the new variables take the same form as the original ones, up to the dissipation terms. For a while, let us ignore the dissipation terms and suppose that the invariance under the rescaling is exact.

We may expect that the stochastic properties of the solutions of those equations respect the same symmetry. Let us focus on the magnetic power spectrum, Eq. (3.14). With the rescaling, Eq. (3.19), the magnetic power spectrum is rescaled as

$$P_B \to P'_B(\tau',k') := \lambda^{3+2r} P_B(\tau,k), \quad k' := \lambda^{-1}k. \tag{3.20}$$

Correspondingly, the variables defined in Eq. (3.9), which determine the location of the peak of the spectrum, are rescaled as

$$B \to B'(\tau') := \lambda^r B(\tau), \quad \xi_{\mathrm{M}} \to \xi'_{\mathrm{M}}(\tau') := \lambda \xi_{\mathrm{M}}(\tau). \tag{3.21}$$

The symmetry implies that these functions in Eqs. (3.20) and (3.21) are invariant under the rescaling:

$$P'_B(\tau', k') = P_B(\tau', k'), \quad B'(\tau') = B(\tau'), \quad \xi'_{\mathrm{M}}(\tau') = \xi_{\mathrm{M}}(\tau'), \tag{3.22}$$

from which we find the scaling property of the magnetic energy spectrum

$$\frac{k'^3 P_B(\tau', k')}{B(\tau')^2} = \frac{k^3 P_B(\tau, k)}{B(\tau)^2}, \quad \xi_{\mathrm{M}}(\tau')k' = \xi_{\mathrm{M}}(\tau)k. \tag{3.23}$$

Let us interpret these relations by regarding τ' as an arbitrary time independent of τ. Once we know the time dependence of the magnetic coherence length, $\xi_{\mathrm{M}}(\tau')$, the second equation in Eq. (3.23) specifies the corresponding k' to an arbitrary wavenumber k. Then, the first equation in Eq. (3.23) implies that the magnetic energy spectrum, given in Eq. (3.11), is time-independent up to normalization by the typical strength B^2 and wavenumber shift by the coherence length ξ_{M} (panel (d) in Fig. 3.1). One may rephrase this argument, or Eq. (3.23), by expressing the magnetic energy spectrum as [33, 59]

$$\frac{d\rho_{\mathrm{M}}}{d\log k}(\tau, k) = B(\tau)^2 \phi(\xi_{\mathrm{M}}(\tau)k), \tag{3.24}$$

where ϕ is an unknown function that determines the shape of the energy spectrum. Decay laws that satisfy Eq. (3.24) are often referred to as self-similar decay. The self-similarity approximately holds for numerical simulations of homogeneous and isotropic turbulences in the literature [31–34]. In the following sections, we assume approximately self-similar decay laws.

One of the biggest questions about self-similar decay has long been how to determine r or, equivalently, the self-similarity parameter [33]

$$\beta := -2r - 1. \tag{3.25}$$

Determination of β is nothing but finding a relationship between the magnetic strength and the coherence length:

$$B(\tau)^2 \xi_{\mathrm{M}}(\tau)^{\beta+1} = \text{const.}, \tag{3.26}$$

which greatly simplifies the further analysis, as we will see in Sec. 4.1. Actually, $\beta = 0$ is established by both theoretical [39, 60] and numerical [61] reasonings for the so-called maximally helical magnetic fields. We will address this case thoroughly in Sec. 4.2.1. Otherwise, however, we do not have any reason to expect $\beta = 0$, and determination of β for the so-called non-helical magnetic fields has long been controversial. A wide-spreading idea was that the infrared (IR) range of the energy spectrum, which corresponds to the scales larger than the coherence length ξ_{M}, is kept intact until the coherence length reaches a given scale (panel (e) in Fig. 3.1). If this is correct, β is determined by the slope of the spectrum in the IR region [29, 59]. Although the same idea for velocity fields in pure hydrodynamics without magnetic field has been consistent with numerical studies [62], it turned out not to be the case for magnetic fields in magneto-hydrodynamics. In contrast to panel (e), which people once expected, panel (f) in Fig. 3.1 is how the decay of magnetic fields looks like in numerical simulations [30–36]. The IR range of the spectrum is enhanced as time passes, which is called the inverse transfer phenomena, implying that β is less than previously expected $\beta = n_{\mathrm{M}} + 2$, where the n_{M} is the magnetic spectral index, based on the wide-spreading idea (panel (e) in Fig. 3.1. A parallel discussion to derive this β can be found around Eq. (4.42)). In Sec. 4.2.2, we will address this issue and identify β to be 3/2, based on the recent progress in this field [37, 40].

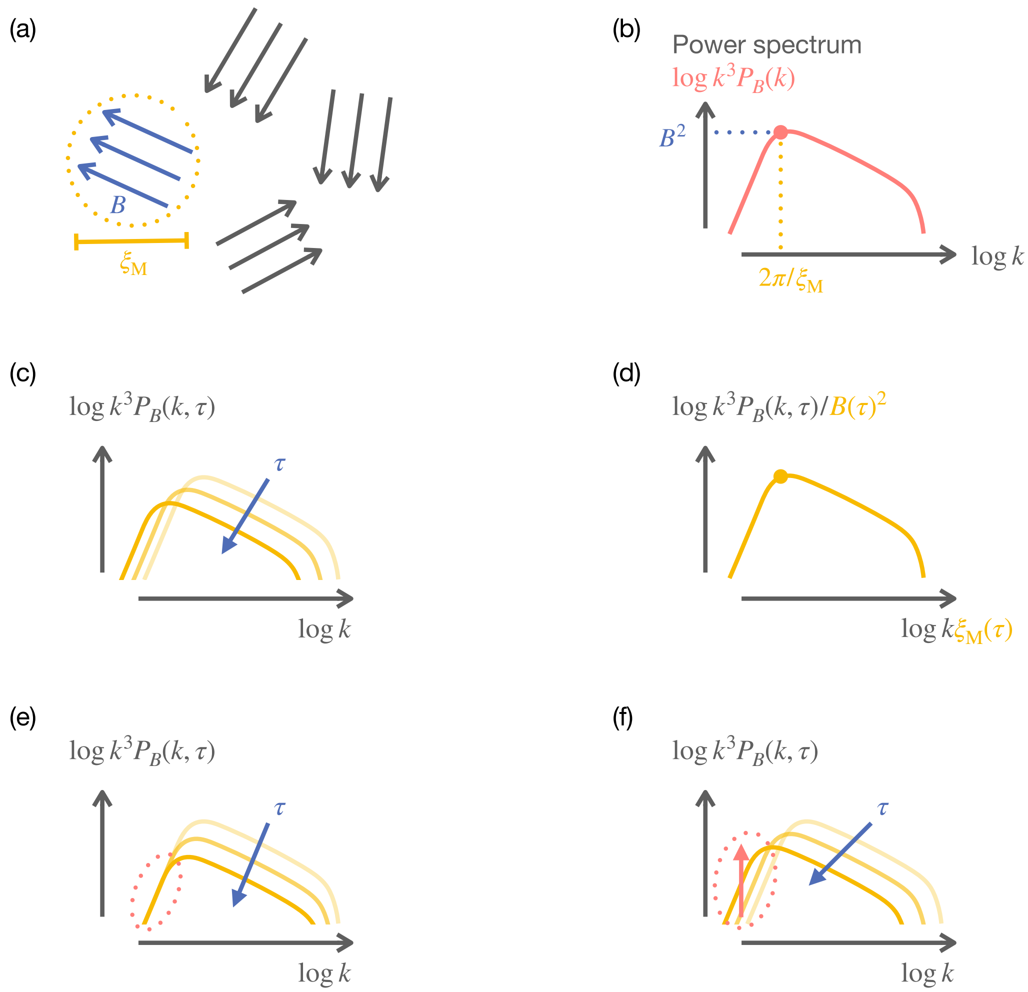

Figure 3.1: Parametrization and decay laws of a stochastic magnetic field. (a) Parametrization of a magnetic field configuration in the real space. B denotes the typical strength and $\xi_{\rm M}$ denotes the coherence length. (b) A typical shape of the magnetic energy spectrum (red solid line). The location of the peak (red dot) determines the typical strength and the coherence length of the magnetic field. (c) How the decay of the magnetic energy spectrum looks like. Each yellow solid line represents the magnetic energy spectrum at a time. As time passes, the spectrum goes downward. Panels (d–f) are special cases of panel (c). (d) Self-similar decay implies that the spectrum is time-independent, if it is rescaled for the peak location (yellow dot) to be fixed. (e) The previously expected decay law, which conserves the magnetic energy spectrum in the IR range (inside the red dotted circle). (f) The numerically found inverse transfer enhances the magnetic energy spectrum in the IR range (inside the red dotted circle).

Chapter 4

Description of the scaling evolution with regime classification

In this chapter, we provide a practically comprehensive description of the scaling evolution of statistically homogeneous magnetic fields, in a general context including but not specific to primordial magnetic fields in the early universe. We first provide readers with a rough sketch of our methodology, which mostly follows the spirit of Ref. [29]. We then introduce conserved quantities and decay time scales, which are the two concepts of the highest importance in the methodology. We incorporate recent progress in the field of research that owes mostly to Ref. [37]. According to which conserved quantity and decay time scale are relevant, we classify the system into sixteen regimes. We analyze magneto-hydrodynamics in each regime, and then discuss the consistency among independent analyses in different regimes, based on our work [44,45]. This lengthy chapter is an indispensable process toward the application in the early universe, which will be summarized in Fig. 5.4.

4.1 Sketch of the strategy

As explained in Sec. 2.1, we know several constraints on primordial magnetic fields. However, they are imposed at different epochs in the history of the universe. To discuss them at the same time, we have to understand the evolution of primordial magnetic fields (orange arrow in Fig. 4.1). For that purpose, we are going to investigate the time dependence of the quantities of our interest in the following sections. Because the whole analysis is done under a lengthy process, it would be better to describe a rough sketch of the strategy of our analysis.

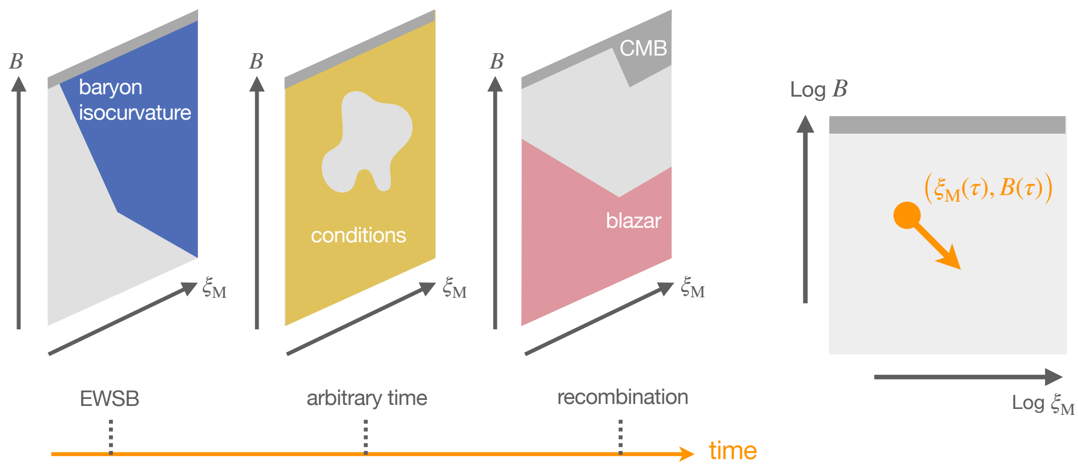

Figure 4.1: The reason we have to understand the evolution of primordial magnetic fields. Left: We have baryon isocurvature constraint at the electroweak epoch, CMB and blazar constraints after the recombination epoch, and possibly any conditions at an arbitrary time. Right: Since they are imposed on the $\xi_{\rm M}$-B plain at different epochs, we have to understand the evolution path of primordial magnetic fields on the plain (orange arrow) to discuss them in connection with each other.

We have magnetic field, $\boldsymbol{B}(\tau, \boldsymbol{x})$, and velocity field, $\boldsymbol{v}(\tau, \boldsymbol{x})$, in the system. If we suppose peaky energy spectra of these fields, as is explained for the magnetic field in panel (b) of Fig. 3.1, we only need to know the time dependence of the typical strength of the magnetic field, $B(\tau)$, the magnetic coherence length, $\xi_{\rm M}(\tau)$, the typical velocity, $v(\tau)$, and the kinetic coherence length, $\xi_{\rm K}(\tau)$. The quasi-self-similar evolution of the power spectra described in Sec. 3.2.2 implies that they provide us with almost all the information about the magnetic and kinetic power spectra.

Typically, we have an approximate conserved quantity in each regime. Let us denote it by $C(B, \xi_{\rm M})$, since it is typically a function of B and $\xi_{\rm M}$. As we will see in Sec. 4.2, C can be magnetic helicity density, the Hosking integral, and so on. Then we have a constraint

$$C\left(B(\tau), \xi_{\rm M}(\tau)\right) = C(B_{\rm ini}, \xi_{\rm M,ini}), \tag{4.1}$$

where the subscript $_{\rm ini}$ implies variables evaluated at the beginning. Suppose that C is a product of some powers of B and $\xi_{\rm M}$, as is turned out in Sec. 4.2 to be the case, then Eq. (4.1) constrains the evolution path of a point $P(\tau)$, which describes the values of B and $\xi_{\rm M}$ at each time τ, along a fixed line in the $\xi_{\rm M}$-B plain (the blue-dotted line in Fig. 4.2).

In addition to this, we typically have an estimate of the decay time scale, which is taken to process the magnetic field by some regime-dependent mechanism of magneto-hydrodynamics. Let us denote it by $\tau_{\rm decay}(\tau, B, \xi_{\rm M})$, where we included an explicit time-dependence to highlight one of the complexity in the analysis, although it is absent in some situations. As we will see in Sec. 4.3, $\tau_{\rm decay}$ can be the magnetic reconnection time scales or the Alfvén time scale. Since the time scale of the expansion of the universe is nothing but τ in the conformal unit, magnetic fields such that the decay time scale $\tau_{\rm decay}$ is smaller than the conformal time τ should have already decayed at some point in the earlier stages of the history of the universe. Then, we expect that either of

$$\tau_{\rm decay}(\tau, B, \xi_{\rm M}) \gg \tau, \quad \text{when the system is frozen,} \tag{4.2}$$

for the cases where the relevant magneto-hydrodynamic mechanism is too slow to process the magnetic field away, or

$$\tau_{\rm decay}(\tau, B, \xi_{\rm M}) \sim \tau, \quad \text{when the system is processed,} \tag{4.3}$$

for the cases where the magnetic field is not frozen but under the process of decay, always holds. These conditions (4.2) and (4.3) exclude the region with stronger magnetic fields in the $\xi_{\rm M}$-B plain (the yellow-shaded regions in Fig. 4.2).

Now let us look at panels (a), (b), and (c) in Fig. 4.2. We are going to track the motion of the point $P(\tau)$ (red circle) in the $\xi_{\rm M}$-B plain. Suppose that the point $P(\tau_{\rm ini})$ initially satisfies Eq. (4.2) and that the excluded region (yellow-shaded) is moving downward as time goes by. (a) The point $P(\tau)$ stays there because Eq. (4.2) implies that the magnetic field is frozen until (b) the edge of the region catches up the point. After that, (c) the system begins to be processed to decay, and then the point $P(\tau)$ moves downward along the line (blue-dotted) determined by Eq. (4.1), satisfying Eq. (4.3) at the same time.

As is shown in panel (d) in Fig. 4.2, sometimes Eq. (4.2) starts to hold and the system becomes frozen again, when the edge of the yellow-shaded region goes upward

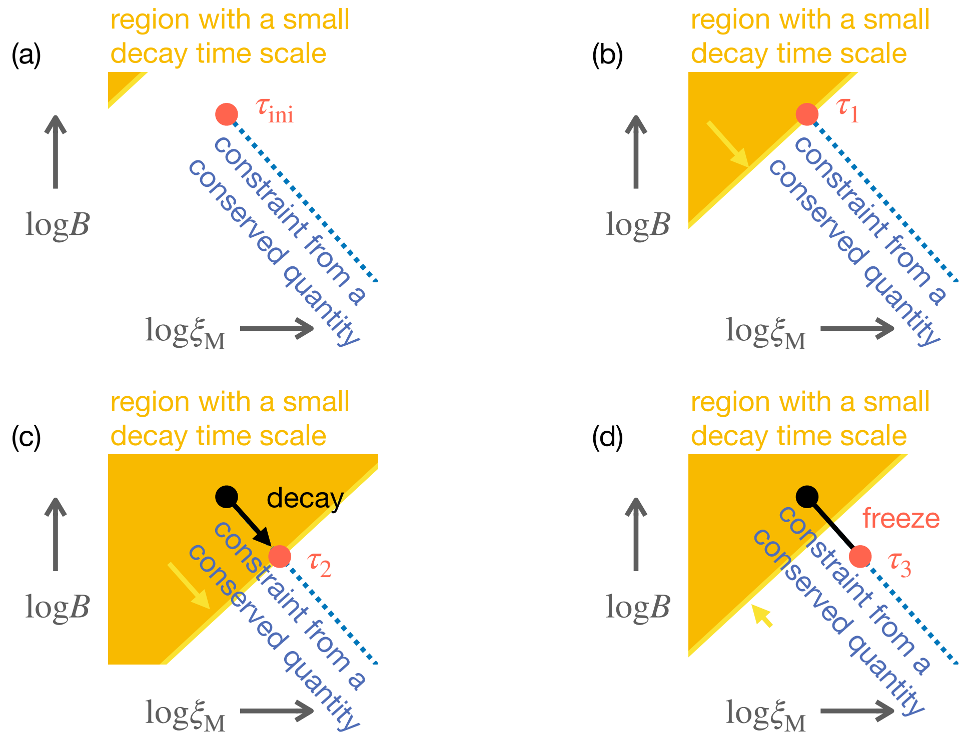

Figure 4.2: Typical evolution of the magnetic field in the $\xi_{\rm M}$-B plain. In each panel, the blue-dotted line is the constraint from a conserved quantity, given by Eq. (4.1), and the edge of the yellow-shaded region, where the decay time scale is so small that magnetic fields quickly decay, is given by Eq. (4.3). (a) The magnetic field stays there when Eq. (4.2) holds, (b) starts to go downward when Eq. (4.3) gets satisfied, (c) then goes downward with Eqs. (4.1) and (4.3) both satisfied, and (d) stays there and Eq. (4.2) holds again when the edge of the yellow-shaded region goes upward.

because of the explicit time dependence of the decay time scale $\tau_{\rm decay}(\tau, B, \xi_{\rm M})$. Such re-entrance into frozen regimes complicates the analysis, and then what we impose in addition to Eq. (4.1) should be

$$\min_{\tau_{\rm ini}\leq\tau'\leq\tau} \frac{\tau_{\rm decay}(\tau', B, \xi_{\rm M})}{\tau'} \sim 1 \tag{4.4}$$

rather than Eq. (4.3). If the solution gives a weaker magnetic field, $B < B_{\rm ini}$, then we interpret the solution as the wanted $B(\tau)$ and $\xi_{\rm M}(\tau)$. Otherwise, the system is frozen all the time until τ, and therefore $B(\tau) = B_{\rm ini}$ and $\xi_{\rm M}(\tau) = \xi_{\rm M,ini}$.

Another complication comes from different analyses in different regimes. We have multiple conserved quantities and decay time scales according to which regime the system belongs to. Also, not only B and ξ_{M} but also other quantities like v and ξ_{K} come into the expression of conserved quantities and decay time scales, which might make the strategy of our analysis unclear to some extent. However, the analysis goes essentially in a similar way to what is explained in this section.

4.2 Conserved quantities

First, let us introduce several approximate conserved quantities in the early universe. The most important one is magnetic helicity density. The recently discovered Hosking integral [37] is even believed to be conserved as a consequence of the conservation of magnetic helicity. And we have several other conserved quantities as well. We review the reason why these quantities are conserved in the ideal limits and discuss when they are conserved well in the non-ideal situation in the early universe.

4.2.1 Magnetic helicity

To avoid confusion, let us start with defining several quantities that are almost the same except essential differences in their properties. They are not always defined separately in the literature, but we have to introduce them for clarity and the later purpose. Magnetic helicity density h is a local quantity defined as

$$h(\boldsymbol{x}) := \boldsymbol{A}(\boldsymbol{x}) \cdot \boldsymbol{B}(\boldsymbol{x}), \tag{4.5}$$

where $\boldsymbol{A}$ is the vector potential. However, this quantity is gauge-dependent, and its local value at a given spatial point has no physical meaning by itself. Instead, one can define U(1)-gauge-invariant magnetic helicity H_V for a volume V such that the normal component of $\boldsymbol{B}$ is zero on its boundary as

$$H_V := \int_V d^3 r h(\boldsymbol{r}), \tag{4.6}$$

and furthermore one may define gauge-invariant magnetic helicity density h_V,

$$h_V := \frac{H_V}{V}. \tag{4.7}$$

If we take small V compared to the whole system size, h_V is a semi-local quantity and quantifies the magnetic helicity density within the volume V. On the contrary, if we take the large-volume limit,

$$\langle h \rangle := \lim_{V\to\infty} h_V \tag{4.8}$$

quantifies a global parity violation of the magnetic field configuration. When the system size, *e.g.,* the Hubble horizon of the present universe, is much larger than the coherence length of the magnetic field, the infinite-volume average can practically be the volume average over the system size. One may identify the infinite-volume average with the ensemble average, as is sometimes referred to as the ergodic hypothesis in this context [49], although the original hypothesis is on the relation between temporal (rather than spatial) averages and ensemble averages. The identification is justified by the homogeneity of the probability distribution over the space and the suppressed correlation beyond the coherence length.

Let us check the gauge-invariance of H_V. Under a gauge transformation by an arbitrary function Γ, which transforms the vector potential as $\boldsymbol{A} \to \boldsymbol{A} + \boldsymbol{\nabla}\Gamma$, magnetic helicity in a closed volume V transforms as

$$\begin{aligned} H_V \to & \int_V d^3r\, (\boldsymbol{A} + \boldsymbol{\nabla}\Gamma)\cdot \boldsymbol{B} \\ &= H_V + \int_{\partial V} d^2\boldsymbol{s}\cdot(\Gamma \boldsymbol{B}) \\ &= H_V, \end{aligned} \tag{4.9}$$

where we have used $\boldsymbol{\nabla}\cdot\boldsymbol{B} = 0$ in the second line and a condition that V is closed, *i.e.,* $\boldsymbol{B}\cdot d^2\boldsymbol{s} = 0$ on its boundary ∂V in the last line. Equation (4.9) implies that H_V is gauge-invariant, and hence h_V and $\langle h\rangle$ are gauge-invariant as well.

Magnetic helicity is an approximate conserved quantity in the large electric conductivity limit [38]. To prove that, we begin with taking the time derivative of magnetic helicity density h.

$$\begin{aligned} \dot{h} &= \dot{\boldsymbol{A}}\cdot\boldsymbol{B} + \boldsymbol{A}\cdot\dot{\boldsymbol{B}} \\ &= 2\dot{\boldsymbol{A}}\cdot\boldsymbol{B} + \boldsymbol{\nabla}\cdot(\dot{\boldsymbol{A}}\times\boldsymbol{A}) \end{aligned}$$

$$
\begin{aligned}
&= 2(-\boldsymbol{E} - \boldsymbol{\nabla} A_0) \cdot \boldsymbol{B} + \boldsymbol{\nabla} \cdot (\dot{\boldsymbol{A}} \times \boldsymbol{A}) \\
&= -2\boldsymbol{E} \cdot \boldsymbol{B} + \boldsymbol{\nabla} \cdot (\dot{\boldsymbol{A}} \times \boldsymbol{A} - 2A_0 \boldsymbol{B}) \\
&= -2\boldsymbol{E} \cdot \boldsymbol{B} - \boldsymbol{\nabla} \cdot (\boldsymbol{E} \times \boldsymbol{A} + A_0 \boldsymbol{B}),
\end{aligned} \tag{4.10}
$$

where A_0 denotes the electric potential and we have used $\boldsymbol{B} = \boldsymbol{\nabla} \times \boldsymbol{A}$ in the second line, $\boldsymbol{E} = -\boldsymbol{\nabla} A_0 - \dot{\boldsymbol{A}}$ in the third and the last lines, and $\boldsymbol{\nabla} \cdot \boldsymbol{B} = 0$ in the fourth line. Then, for a time-dependent closed volume V that moves with velocity $\boldsymbol{v}$ according to the motion of the fluid,

$$
\begin{aligned}
\dot{H}_V &= \int_V d^3 r \dot{h} + \int_{\partial V} d^2 \boldsymbol{s} \cdot \boldsymbol{v} h \\
&= -2 \int_V d^3 r \boldsymbol{E} \cdot \boldsymbol{B} + \int_{\partial V} d^2 \boldsymbol{s} \cdot [\boldsymbol{v}(\boldsymbol{A} \cdot \boldsymbol{B}) - (\boldsymbol{E} \times \boldsymbol{A} + A_0 \boldsymbol{B})] \\
&= -2\sigma^{-1} \int_V d^3 r \boldsymbol{j} \cdot \boldsymbol{B} - \sigma^{-1} \int_{\partial V} d^2 \boldsymbol{s} \cdot (\boldsymbol{j} \times \boldsymbol{A}) + \int_{\partial V} d^2 \boldsymbol{s} \cdot \boldsymbol{B} (\boldsymbol{v} \cdot \boldsymbol{A} - A_0) \\
&= -\sigma^{-1} \left[2 \int_V d^3 r \boldsymbol{j} \cdot \boldsymbol{B} + \int_{\partial V} d^2 \boldsymbol{s} \cdot (\boldsymbol{j} \times \boldsymbol{A}) \right],
\end{aligned} \tag{4.11}
$$

where we have included the advection term in the first line, substituted Eqs. (4.6) and (4.10) in the second line, used Ohm's law in the third line, and used the condition that V is closed in the last line. From the proportionality to the electric resistivity σ^{-1}, we see that H_V is approximately conserved in the large conductivity limit, $\sigma \to \infty$. If the fluid is incompressible, $\dot{V} = 0$, and then $h_V = H_V / V$ is conserved in the large conductivity limit as well. When taking the infinite-volume limit, the random motion of fluid on the boundary of the volume ∂V would cancel so that $\dot{V} = \int_{\partial V} d^2 \boldsymbol{s} \cdot \boldsymbol{v} \to 0$ even without the assumption of local incompressibility, $\boldsymbol{\nabla} \cdot \boldsymbol{v} = 0$. Therefore, $\langle h \rangle$ is also conserved in the large conductivity limit.

To understand why H_V is conserved and also for the later purpose, it would be good to explain Alfvén's theorem [63, 64], which proofs that magnetic field lines are frozen in the fluid in the large conductivity limit. For any surface S that moves with velocity $\boldsymbol{v}$ according to the motion of the fluid,

$$
\begin{aligned}
\frac{d}{d\tau} \int_S d^2 \boldsymbol{s} \cdot \boldsymbol{B} &= \int_S d^2 \boldsymbol{s} \cdot \dot{\boldsymbol{B}} - \int_{\partial S} (d\boldsymbol{l} \times \boldsymbol{v}) \cdot \boldsymbol{B} \\
&= \int_S d^2 \boldsymbol{s} \cdot \dot{\boldsymbol{B}} - \int_{\partial S} d\boldsymbol{l} \cdot (\boldsymbol{v} \times \boldsymbol{B})
\end{aligned}
$$

$$
\begin{aligned}
&= \int_S d^2\boldsymbol{s} \cdot \left[\dot{\boldsymbol{B}} - \boldsymbol{\nabla} \times (\boldsymbol{v} \times \boldsymbol{B}) \right] \\
&= \sigma^{-1} \int_S d^2\boldsymbol{s} \cdot \nabla^2 \boldsymbol{B},
\end{aligned} \tag{4.12}
$$

where we have included the advection term in the first line and used the induction equation (3.2) in the last line. The final expression becomes zero in the large conductivity limit, $\sigma \to \infty$, implying that magnetic flux across the surface S is conserved. Since S is chosen arbitrarily, we understand that magnetic field lines are advected, keeping their flux, by the fluid motion.

Then, the topology of magnetic field lines is unchanged because any continuous transformation by the fluid motion cannot untie links and knots of the field lines. Actually, magnetic helicity H_V quantifies nothing but the topology of magnetic field lines [65,66]. To understand that, probably the most common example [60,67–69] to demonstrate is a link between two flux loops (panel (a) and (b) in Fig. 4.3). However, we are going to provide another example with a trefoil knot (panel (c) in Fig. 4.3), which seems not too common to demonstrate the explicit calculation here. Let us consider a trefoil knot of a magnetic flux Φ. The volume integral is reduced to a contour integral along the magnetic flux tube as

$$
\begin{aligned}
H_V &= \int_{\text{trefoil}} d^3r \boldsymbol{A} \cdot \boldsymbol{B} \\
&= \Phi \int_{C_1+C_2+C_3} d\boldsymbol{l} \cdot \boldsymbol{A}.
\end{aligned} \tag{4.13}
$$

We have used the definition of magnetic flux, $\Phi = \int_S d^2 sB$, where S is the cross-section normal to $\boldsymbol{B}$ of the tube. Also, we have decomposed the integration contour into three loops C_1, C_2, and C_3, which are illustrated in panel (d) in Fig. 4.3. Let us focus on the contribution from C_1.

$$
\begin{aligned}
\Phi \int_{C_1} d\boldsymbol{l} \cdot \boldsymbol{A} &= \Phi \int_{S_1} d^2\boldsymbol{s} \cdot (\boldsymbol{\nabla} \times \boldsymbol{A}) \\
&= \Phi \int_{S_1} d^2\boldsymbol{s} \cdot \boldsymbol{B} \\
&= \Phi^2,
\end{aligned} \tag{4.14}
$$

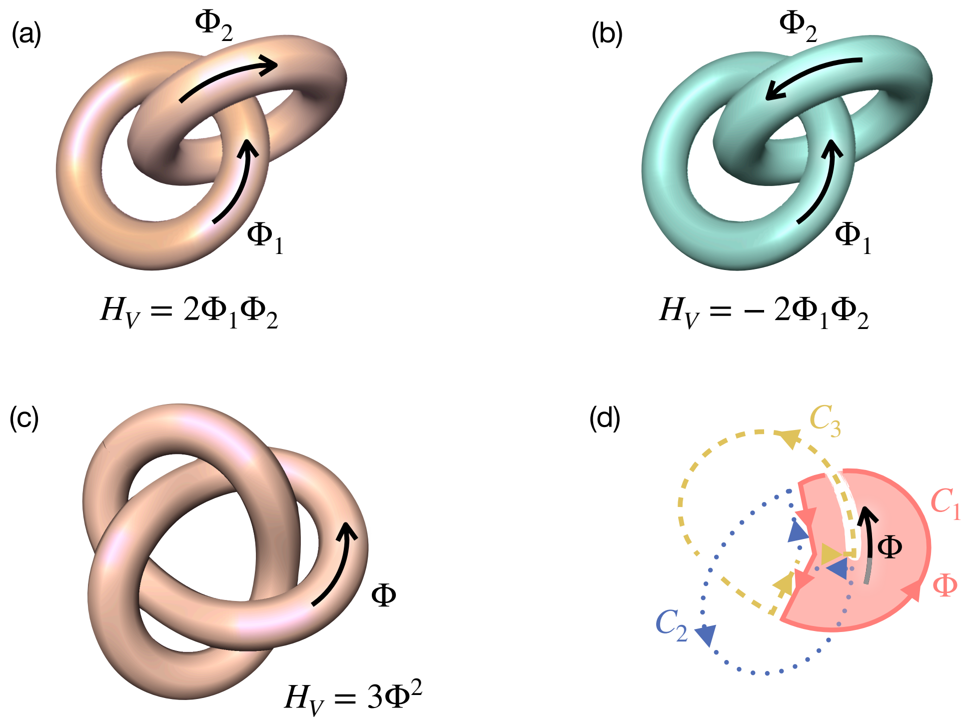

Figure 4.3: Simplest magnetic field configurations that have finite magnetic helicity. (a) A link of magnetic fluxes Φ_1 and Φ_2, whose magnetic helicity is $2\Phi_1\Phi_2$. (b) An anti-link of magnetic fluxes Φ_1 and Φ_2, whose magnetic helicity is $-2\Phi_1\Phi_2$. (c) A trefoil knot of magnetic flux Φ, whose magnetic helicity is $3\Phi^2$. (d) In the calculation of magnetic helicity of the trefoil configuration, we separate the integration contour into three loops C_1, C_2, and C_3. Each loop has a contribution Φ^2.

where S_1 is a surface surrounded by the loop C_1, so that $\partial S_1 = C_1$. Parallel calculations apply to contributions from C_2 and C_3. Then, we reproduce the same result as the one in Ref. [70],

$$\text{Eq. (4.13)} = 3\Phi^2. \tag{4.15}$$

We have learned one of the simplest examples to understand that magnetic helicity quantifies the topology of the magnetic field configuration. Then, it is quite understandable that magnetic helicity is conserved because of the conservation of the topology in the large conductivity limit.

A unique property of $\langle h \rangle$ is the realizability condition [58]. We may parametrize to what extent parity is violated by introducing the magnetic helicity fraction

$$\epsilon := \frac{2\pi\langle h \rangle}{B^2 \xi_{\mathrm{M}}}, \tag{4.16}$$

and then, by considering $\langle h \rangle = \langle \boldsymbol{A} \cdot \boldsymbol{B} \rangle$ as the inner product of two fields $\boldsymbol{A}(\boldsymbol{x})$ and $\boldsymbol{B}(\boldsymbol{x})$, Schwarz inequality implies

$$|\epsilon| \leq 1. \tag{4.17}$$

Later in Sec. 4.2.2, we will see that this is nothing but an integrated version of Eq. (3.18). Since $\langle h \rangle$ is an approximate conserved quantity, the realizability condition (4.17) imposes

$$B(\tau)^2 \xi_{\mathrm{M}}(\tau) \geq 2\pi |\langle h \rangle| = |\epsilon_{\mathrm{ini}}| B_{\mathrm{ini}}^2 \xi_{\mathrm{M,ini}} \tag{4.18}$$

on the evolution of the system. In particular, when the helicity fraction is $|\epsilon(\tau)| = 1$, we say that the magnetic field is maximally helical, and the evolution of the system is constrained by the condition [39]

$$B(\tau)^2 \xi_{\mathrm{M}}(\tau) = B_{\mathrm{ini}}^2 \xi_{\mathrm{M,ini}} \quad \text{for maximally helical magnetic field.} \tag{4.19}$$

One may ask whether the approximate conservation of magnetic helicity holds or not in the early universe. From Eq. (4.11) and by dimensional analysis, one can estimate the decay time scale of H_V as

$$\frac{H_V}{\dot{H}_V} \sim \frac{B^2 \xi_M}{\sigma^{-1} j B} \sim \frac{B^2 \xi_M^2}{\sigma^{-1} B^2} \sim \sigma \xi_M^2, \tag{4.20}$$

where we have omitted the helicity fraction ϵ because the degree of parity violation would appear both in the numerator or denominator and estimated $j \sim B/\xi_{\mathrm{M}}$. From this estimate, we obtain a condition

$$\xi_{\mathrm{M}} \gg \sigma^{-\frac{1}{2}} \tau^{\frac{1}{2}}, \tag{4.21}$$

with which we can use $\langle h \rangle$ as a conserved quantity at a given time τ and use Eqs. (4.18) and (4.19) to analyze the evolution of the system in the early universe.

4.2.2 Hosking integral

Recently, another approximate conserved quantity of magneto-hydrodynamics has been discovered in Ref. [37]. Since theoretical understanding of its gauge-invariance and conservation has not been established rigorously, we give an ambiguous definition as is often seen in the literature. The Hosking integral is defined as [37]

$$I_{\mathrm{H}} := \int d^3r \langle h(\boldsymbol{x}) h(\boldsymbol{x}+\boldsymbol{r}) \rangle, \tag{4.22}$$

where the angle bracket denotes an ensemble average. In the dedicated numerical study [40], they proposed several practical ways, which are not equivalent to each other, to incorporate the finite system size and the difficulty of taking the ensemble average into the definition (4.22).

In this thesis, to highlight the physical meaning of Hosking integral, we approximate the ensemble average by a volume average over a large volume V and define

$$I_{\mathrm{H}V,W} := \frac{1}{V} \int_V d^3x \int_W d^3r h(\boldsymbol{x}) h(\boldsymbol{x}+\boldsymbol{r}), \tag{4.23}$$

as is introduced as the correlation-integral method in Ref. [40]. We rewrite it as

$$\begin{aligned} I_{\mathrm{H}V,W} &= \frac{1}{V} \int_V d^3x h(\boldsymbol{x}) \int_W d^3r h(\boldsymbol{x}+\boldsymbol{r}) \\ &= \frac{1}{V} \int_V d^3x h(\boldsymbol{x}) \int_{W(\boldsymbol{x})} d^3y h(\boldsymbol{y}), \end{aligned} \tag{4.24}$$

where $W(\boldsymbol{x})$ is the volume W up to a shift $\boldsymbol{x}$ from the origin. The point in the final expression is that one could expect $I_{\mathrm{H}V,V} \simeq H_V^2/V$ by taking the volumes of V and W the same. Theoretical support of finiteness, gauge-invariance, and conservation of Hosking integral [37,43] in the literature is based on this expectation, parallelly to the long-standing argument on the Saffman integral [71]. However, to be rigorous, we should not overlook the $\boldsymbol{x}$ dependence of the second factor. To overcome this issue, we refine the argument in the following paragraphs.[1]

[1]This is an extension of the explanation about the conservation of the Saffman integral in Ref. [71], but has never been completely provided in the literature as far as we know.

As a lemma, we remind the readers of the property of a random walk. When we have N random variables that are independent and identically distributed, the deviation of their sum from the expectation is proportional to $\sqrt{N}$.

Let us assume $\langle h \rangle = 0$. Otherwise, we roughly evaluate Eq. (4.22) to be $W\langle h \rangle^2$, which diverges in the large W limit. In addition, suppose that V and W are spheres of radius $R \gg \xi_{\mathrm{M}}$ for simplicity. Then we expect

1. The second factor in Eq. (4.24), which we denote as $H_{W(\boldsymbol{x})}$ hereafter, is almost gauge-invariant and conserved, and scales as $H_{W(\boldsymbol{x})} \propto R^{3/2}$.

2. Eq. (4.24) is almost gauge-invariant and conserved, and scales as $\propto R^0$.

3. In the large R limit, Eq. (4.24) is finite, gauge-invariant, and conserved.

These statements are justified under the assumption that magnetic fields behave randomly beyond the coherence length ξ_M. Let us explain one by one from the first statement. If we regard $H_{W(\boldsymbol{x})}$ as a summation of $N_1 \propto W \propto R^3$ random variables, which are magnetic helicities within coherent sub-volumes filling W, then the lemma implies $H_{W(\boldsymbol{x})} \propto \sqrt{N_1} \propto R^{3/2}$. Its gauge-invariance and conservation hold, if we can neglect the surface terms in Eqs. (4.9) and (4.11). This is actually the case because we have $N_2 \propto \mathrm{Area}(\partial W(\boldsymbol{x})) \propto R^2$ random contributions on the boundary, which cancel up to fluctuations $\propto \sqrt{N_2} \propto R$. This contribution is negligible compared to $H_{W(\boldsymbol{x})} \propto R^{3/2}$ in the large R limit. Let us move on to the second statement. As to the integral $\int_V h(\boldsymbol{x}) H_{W(\boldsymbol{x})}$, if we approximate that $h(\boldsymbol{x})$ and $H_{W(\boldsymbol{x})}$ are independent random variables, the latter typicaly scales as $R^{3/2}$ and the former contributes as $\propto \sqrt{V} \propto R^{3/2}$. Then, we expect the scaling Eq. (4.24) $\propto R^0$. Its gauge-invariance and conservation are more subtle than that of $H_{W(\boldsymbol{x})}$. By parallel computations to Eqs. (4.9) and (4.11), we have to neglect not only surface terms but also contributions in the form $\int_V (\text{terms}) \cdot \boldsymbol{\nabla} H_{W(\boldsymbol{x})}$, where (terms) denotes $\Gamma \boldsymbol{B}$ for Eq. (4.9) and $\boldsymbol{E} \times \boldsymbol{A} + A_0 \boldsymbol{B}$ for Eq. (4.11). These contributions are negligible because

$$\boldsymbol{\nabla} H_{W(\boldsymbol{x})} = \int_{\partial W(\boldsymbol{x})} d^2\boldsymbol{s}\, h(\boldsymbol{y}), \tag{4.25}$$

which scales as $\propto \sqrt{N_2} \propto R$, and is negligible compared to $H_{W(\boldsymbol{x})} \propto R^{3/2}$ in the large R limit. Straightforwardly from the second statement, we expect the third one.

Now we can identify

$$I_{\rm H} = \lim_{V\to\infty} I_{{\rm H}V,V} \tag{4.26}$$

and use it as finite, gauge-invariant, and conserved quantity for the case $\langle h\rangle = 0$. Its gauge-invariance and conservation are observed numerically in Ref. [40], where they identify $I_{{\rm H}V,W}$ as Hosking integral, by taking V to be the simulation box size and W to be a sufficiently large volume. As is clear from the above discussion for the justification, Hosking integral $I_{\rm H}$ quantifies the local fluctuations of magnetic helicity from zero, as seen in Fig. 4.4.

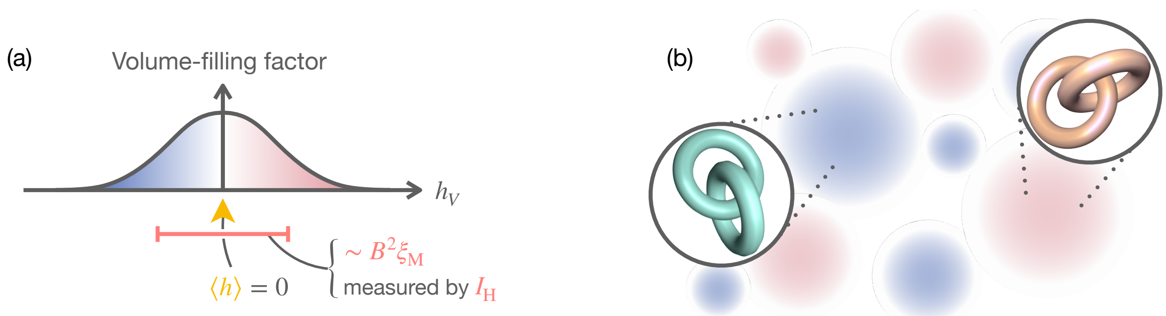

Figure 4.4: (a) The probability distribution or the volume-filling factor of magnetic helicity density. It fluctuates around the expectation value $\langle h\rangle$. The deviation from $\langle h\rangle$ is typically of the order of $B^2\xi_{\rm M}$, as shown in Eq. (4.34). When $\langle h\rangle = 0$, Hosking integral $I_{\rm H}$ has a physical meaning that it measures the fluctuation. (b) Spatial distribution of magnetic helicity density. Local structures such as links or anti-links contribute to positive or negative magnetic helicity density in the local regions.

One can estimate the value of $I_{\rm H}$ in terms of B and $\xi_{\rm M}$ [37]. Since the two-point function of magnetic helicity density in the integrand of the expression (4.22) is essentially the four-point function of the magnetic field, we can decompose it into products of two-point functions of the magnetic field that are characterized by B and $\xi_{\rm M}$ if we assume quasi-Gaussianity in the Fourier space [27]. By inserting volume averaging that does not affect ensemble averaging, which is position-independent, we find an expression in the Fourier space,

$$\begin{aligned}
I_{\mathrm{H}} &= \int d^3r \langle A_i(\boldsymbol{x})B_i(\boldsymbol{x})A_j(\boldsymbol{x}+\boldsymbol{r})B_j(\boldsymbol{x}+\boldsymbol{r})\rangle \\
&= \frac{1}{V}\int d^3x \int d^3r \langle A_i(\boldsymbol{x})B_i(\boldsymbol{x})A_j(\boldsymbol{x}+\boldsymbol{r})B_j(\boldsymbol{x}+\boldsymbol{r})\rangle \\
&= \frac{1}{V}\int d^3x \int d^3r \int \frac{d^3k}{(2\pi)^3}\int \frac{d^3l}{(2\pi)^3}\int \frac{d^3p}{(2\pi)^3}\int \frac{d^3q}{(2\pi)^3} \\
&\qquad e^{i\boldsymbol{k}\cdot\boldsymbol{x}+i\boldsymbol{l}\cdot\boldsymbol{x}+i\boldsymbol{p}\cdot(\boldsymbol{x}+\boldsymbol{r})+i\boldsymbol{q}\cdot(\boldsymbol{x}+\boldsymbol{r})}\langle A_i(\boldsymbol{k})B_i(\boldsymbol{l})A_j(\boldsymbol{p})B_j(\boldsymbol{q})\rangle \\
&= \frac{1}{V}\int \frac{d^3k}{(2\pi)^3}\int \frac{d^3p}{(2\pi)^3}\langle A_i(\boldsymbol{k})B_i(-\boldsymbol{k})A_j(\boldsymbol{p})B_j(-\boldsymbol{p})\rangle,
\end{aligned} \tag{4.27}$$

where $V = (2\pi)^2\delta^3(\boldsymbol{k}=\boldsymbol{0})$ formally denotes the volume of the whole space. By assuming quasi-Gaussianity and using isotropy, Eqs. (2.2) and (3.15), the integrand of Eq. (4.27) is decomposed as

$$\begin{aligned}
\langle A_i(\boldsymbol{k})B_i(-\boldsymbol{k})A_j(\boldsymbol{p})B_j(-\boldsymbol{p})\rangle &= \langle A_i(\boldsymbol{k})B_i(-\boldsymbol{k})\rangle\langle A_j(\boldsymbol{p})B_j(-\boldsymbol{p})\rangle \\
&\quad + \langle A_i(\boldsymbol{k})A_j(\boldsymbol{p})\rangle\langle B_i(-\boldsymbol{k})B_j(-\boldsymbol{p})\rangle \\
&\quad + \langle A_i(\boldsymbol{k})B_j(-\boldsymbol{p})\rangle\langle B_i(-\boldsymbol{k})A_j(\boldsymbol{p})\rangle \\
&= V^2k^{-2}A_B(k)A_B(p) \\
&\quad + (2\pi)^3\delta^3(\boldsymbol{k}+\boldsymbol{p})Vk^{-2}\frac{P_B^2(k)+A_B^2(k)}{2} \\
&\quad + (2\pi)^3\delta^3(\boldsymbol{k}-\boldsymbol{p})Vk^{-2}\frac{P_B^2(k)+A_B^2(k)}{2},
\end{aligned} \tag{4.28}$$

where we have used Eqs. (3.16) and (3.17) in the second equality. As for the contribution from the first term in the final expression of Eq. (4.28), a useful relationship between the parity-violating contributions is

$$\begin{aligned}
\langle h\rangle &= \frac{1}{V}\int d^3x\langle \boldsymbol{A}(\boldsymbol{x})\cdot\boldsymbol{B}(\boldsymbol{x})\rangle \\
&= \frac{1}{V}\int \frac{d^3k}{(2\pi)^3}\langle \boldsymbol{A}(\boldsymbol{k})\cdot\boldsymbol{B}(-\boldsymbol{k})\rangle \\
&= \int \frac{d^3k}{(2\pi)^3}k^{-1}A_B(k),
\end{aligned} \tag{4.29}$$

from which we understand that the realizability condition (4.17) is saturated when the mode-wise inequality (3.18) is saturated. By substituting Eq. (4.29), we have a divergent contribution to $I_{\rm H}$ for nonzero helicity fraction, namely

$$V\langle h\rangle^2 = \frac{\epsilon^2}{4\pi^2}B^4\xi_{\rm M}^2 V, \tag{4.30}$$

in the large V limit. This is consistent with the heuristic argument above in this section 4.2.2 and confirms that $\epsilon = 0$ is necessary for the Hosking integral to be well-defined. We then assume $\epsilon = 0$. As for the contribution from the second and the last terms in the final expression of Eq. (4.28), we obtain

$$I_{\rm H} = \int \frac{d^3k}{(2\pi)^3} k^{-2}(P_B^2(k) + A_B^2(k)). \tag{4.31}$$

Because of the realizability condition, Eq. (3.18), the contribution from A_B is always subdominant. In particular, if we suppose $A_B(k) \propto P_B(k)$, which is not the case in general, $\epsilon = 0$ implies $A_B(k) = 0$. The dominant contribution from $P_B(k)$ is, if we assume a peaky spectrum, approximated by the dimensional analysis, implying [37]

$$I_{\rm H} \sim B^4\xi_{\rm M}^5. \tag{4.32}$$

Of course, this approximation involves a numerical coefficient depending on the shapes of the spectrum. However, importantly, self-similar decay does not change the coefficient in time. From the evaluation, Eq. (4.32), of the Hosking integral, we expect that the evolution of non-helical magnetic fields is constrained by the condition [37]

$$B(\tau)^4\xi_{\rm M}(\tau)^5 = B_{\rm ini}^4\xi_{\rm M,ini}^5 \quad \text{for non-helical magnetic field}, \tag{4.33}$$

when the electric conductivity is sufficiently large.

Let us mention an implication of the evaluation Eq. (4.32). If we approximate that the two-point correlation of magnetic helicity density is $\langle h_V^2\rangle$ inside each coherent patch and vanishes beyond the coherence length $\xi_{\rm M}$, and then we obtain $I_{\rm H} \sim \xi_{\rm M}^3\langle h_V^2\rangle$ [40] from the expression in Eq. (4.22). By comparing this evaluation with the one in Eq. (4.32), we obtain

$$\langle h_V^2\rangle \sim B^4\xi_{\rm M}^2, \tag{4.34}$$

implying that magnetic helicity density locally fluctuates with the amplitude $\sim B^2\xi_{\rm M}$ even if the magnetic field is globally non-helical [27] (panel (a) in Fig. 4.4). This is the reason why we still have a conservation law for non-helical magnetic fields, which might appear contradictory.

4.2.3 Kinetic energy at large scales

When the system is kinetically dominated and the dynamics is governed by the velocity field, it would be a good approximation to consider the dynamics as pure hydrodynamics without magnetic field.

It is established in pure hydrodynamics that the IR region of the power spectrum of velocity field is conserved and that only the energy at small scales decays [62], which is analogous to the situation in panel (e) of Fig. 3.1. This is understandable, since the non-linear dynamics of velocity fields is a cascade process that transfers energy from a given scale to slightly smaller scales, in a way that "*Big whirls have little whirls that feed on their velocity, and little whirls have lesser whirls and so on to viscosity— in the molecular sense*" [72]. The size of the largest eddies (or whirls in the above quotation) being processed can be identified as the kinetic coherence length $\xi_{\rm K}$ (panel (d) in Fig. 4.5), since the cascade decreases the kinetic energy spectrum at smaller scales and leaves a peak of the spectrum at the largest scale of the cascading range. Then, it is reasonable to assume linearity in the IR region, while even the cascade process is semi-linear or, equivalently, semi-local in the Fourier space because the energy at a given k-mode is transferred to adjacent modes [60]. Assuming linearity, the characteristic decay time scale for the mode at a scale ξ is the eddy turnover time

$$\tau_{\rm eddy}(\xi) := \frac{\xi}{v(\xi)}, \tag{4.35}$$

where

$$v(\xi) := \sqrt{\frac{2}{\rho+p}\left.\frac{d\rho_{\rm K}}{d\log k}\right|_{k=\frac{2\pi}{\xi}}} \tag{4.36}$$

is the typical velocity at the scale ξ [29]. Note that $v = v(\xi_{\rm K})$ is what we have defined in Eq. (3.10). One may interpret this scale-wise time scale $\tau_{\rm eddy}(\xi)$ as the time for an eddy of the size ξ to break into smaller eddies. In the cascading region, the process is fast enough to take place, $\tau_{\rm eddy}(\xi) \ll \tau$. However, larger scales typically have longer time scales. At the peak of the spectrum,

$$\tau = \tau_{\rm eddy}, \quad \tau_{\rm eddy} := \tau_{\rm eddy}(\xi_{\rm K}) \tag{4.37}$$

holds, as the eddies of the size $\xi_{\rm M}$ just begin to suffer from the cascade process. In the IR region, the cascade process does not work because the process is too slow at larger scales, $\tau_{\rm eddy}(\xi) \gg \tau$, implying that the IR region of the spectrum is frozen.

Let us mention another interpretation of the frozen IR spectrum, for it is historically important. We may expand the velocity power spectrum for small k as [73]

$$k^3 P_v(\tau, k) = k^3 \left(I_{\rm S} + \frac{k^2}{6} I_{\rm L} + \mathcal{O}(k^4) \right) \tag{4.38}$$

by assuming the analyticity of $P_v(k)$ with respect to $\boldsymbol{k}$. This assumption is equivalent to a vanishing two-point correlation of the velocity field at large distances, which appears reasonable for causal generation mechanisms [56]. Actually, the discussion in Ref. [56] is rather about magnetic fields, in which the solenoidal condition implies the analyticity of $\hat{k}_i \hat{k}_j P_B(k)$ and hence leads to $d\rho_{\rm M}/d\log k \propto k^5$ at the leading order. For now, however, we include $I_{\rm S}$ in the expression (4.38) because we are not restricting ourselves to the discussion on incompressible velocity fields. One can confirm the following relations,

$$I_{\rm S} = \int d^3 r \langle \boldsymbol{v}(\boldsymbol{x}) \cdot \boldsymbol{v}(\boldsymbol{x} + \boldsymbol{r}) \rangle, \tag{4.39}$$

$$I_{\rm L} = - \int d^3 r r^2 \langle \boldsymbol{v}(\boldsymbol{x}) \cdot \boldsymbol{v}(\boldsymbol{x} + \boldsymbol{r}) \rangle, \tag{4.40}$$

by inserting volume averaging, going to the Fourier space, and substituting Eq. (4.38) in the right hand sides. Then, the conservation of the IR spectrum implies that the Saffman integral, which is defined as the right hand side of Eq. (4.39), is a conserved quantity [71, 74] and that, for Bachelor spectrum $d\rho_{\rm K}/d\log k \propto k^5$ with vanishing

Saffman integral $I_\mathrm{S} = 0$, Loitsyanskii integral, which is defined as the right hand side of Eq. (4.40), is a conserved quantity [75, 76]. Actually, the idea of Hosking integral [37] explained in Sec. 4.2.2 is proposed as an analogue of the Saffman integral.

If we parametrize the IR slope of a peaky kinetic power spectrum by n as

$$P_v(k,\tau) = 2\pi^2 A k^n \quad \text{for} \quad k \lesssim \frac{2\pi}{\xi_\mathrm{K}}, \tag{4.41}$$

then the amplitude A is approximated by $A \simeq v^2(\xi_\mathrm{K}/2\pi)^{n+3}$, by evaluating Eq. (3.12) at the peak scale. The conservation of the IR spectrum, $A = \text{const.}$, implies

$$v^2 \xi_\mathrm{K}^{n+3} = \text{const.} \quad \text{in pure hydrodynamics.} \tag{4.42}$$

This condition constrains the dynamics of the velocity field and even the magnetic field in the system, when the process of energy decay is governed by the velocity field. In particular, $n = 0$ and 2 correspond to the conservation of Saffman and Loitsyanskii integral, respectively.

4.2.4 Cross helicity

So far, we have not mentioned kinetic helicity and cross helicity. Indeed, kinetic helicity, which is defined as $\int_V d^3x h_\mathrm{K}(\boldsymbol{x})$, where $h_\mathrm{K} := \boldsymbol{v}\cdot(\boldsymbol{\nabla}\times\boldsymbol{v})$, is approximately conserved in pure hydrodynamics without magnetic field. However, it is unimportant in our discussion because it is not conserved in the presence of magnetic field. On the other hand, cross helicity is marginally conserved in the following sense. Cross helicity density h_C is locally defined as

$$h_\mathrm{C} := \boldsymbol{v}\cdot\boldsymbol{B}. \tag{4.43}$$

By using Eqs. (3.2) and (3.3), we obtain

$$\dot{h}_\mathrm{C} = (\text{total derivatives}) + \eta(\nabla^2\boldsymbol{v})\cdot\boldsymbol{B} - \alpha\boldsymbol{v}\cdot\boldsymbol{B} + \frac{1}{\sigma}\boldsymbol{v}\cdot(\nabla^2\boldsymbol{B}), \tag{4.44}$$

which implies that cross helicity within a volume $\int_V d^3x h_\mathrm{C}(\boldsymbol{x})$ is conserved up to the non-ideal dissipation effects if we assume appropriate boundary conditions. Then, if we ignore the dissipation terms, we can introduce the average cross helicity $\langle h_{\mathrm{C}} \rangle$ and Saffman cross-helicity integral [37]

$$I_{\mathrm{C}} := \int d^3 r \langle h_{\mathrm{C}}(\boldsymbol{x}) h_{\mathrm{C}}(\boldsymbol{x}+\boldsymbol{r}) \rangle, \tag{4.45}$$

parallelly to the discussion in Secs. 4.2.1 and 4.2.2, as conserved quantities left to be mentioned. However, their conservation is only marginal because the dissipation terms in Eq. (4.44) include η and α. While the resistivity σ^{-1} may be neglected because of the large magnetic Prandtl number

$$\mathrm{Pr}_{\mathrm{M}} := \sigma\eta \tag{4.46}$$

in the early universe [29], either of η or α can not be neglected because they are nothing but the origin of the energy dissipation. Therefore, in general, it is not a reliable approximation to use the ideal conservation laws to constrain the energy decay laws. We will return to this point in Secs. 4.5.3 and 4.5.4.

4.3 Decay time scales

Next, we introduce several decay time scales. Each time scale corresponds to a physical mechanism of energy dissipation. The time scale of magnetic reconnection is introduced in Sec. 4.3.1, based on the recent proposal [37]. The time scales of kinetic turbulence (Sec. 4.3.2) and the linear dissipation effects (Sec. 4.3.3) are introduced as well. Since which time scale is relevant depends on the regime, we just introduce the time scales and leave this point to Sec. 4.5.

4.3.1 Reconnection time scale

Let us ignore the energy dissipation by the finite resistivity and suppose that magnetic energy dominates over kinetic energy. Then, the process of energy dissipation will be two-fold. Magnetic energy is transferred to the velocity field, and the kinetic energy is both fed by the magnetic field and dissipated by either the shear viscosity or the drag force. An established picture of such processes is the magnetic reconnection [77–80]. It is a violent process such that anti-parallel magnetic field lines annihilate and that the initial magnetic energy is dissipated or converted into the energy of outflows from the reconnecting region. Such processes are assumed to continue stationarily in a scaling regime of the evolution [37].

Let us look at panels (a–c) of Fig. 4.5. In our homogeneous and isotropic universe, magnetic reconnection can be modeled as follows [37, 44]. The whole space consists of unit patches whose sizes are typically the coherence length of the magnetic field $\xi_{\rm M}$ (panel (a)). We suppose that each patch is a cube that is separated into half regions by a thin sheet (orange-shaded regions in panels (a–c)) at the middle of the height. The directions of the sheets in cubes are assigned randomly because correlation beyond the coherence scale $\xi_{\rm M}$ is suppressed, guaranteeing the isotropy of the whole space. Each sheet is the so-called current sheet or the neutral region, where the magnetic reconnection is taking place (panel (b)). Magnetic fields are coherently filling each half of the unit patch and are anti-parallel on both sides of the current sheet (red solid arrows in panels (b) and (c)). They are inflowing into the sheet with inflow velocity $v_{\rm in}$ (vertical blue-dotted arrows in panels (b) and (c)). Inside the sheet, magnetic field vanishes and the energy inflowing from both sides of the sheet is converted into a fluid flow $v_{\rm out}$ inside the sheet (horizontal blue-dotted arrows in panel (c)). Some portion of the flows is dissipated inside the sheet [79] and the remaining is outflowing from the sheet [77, 78].

In this picture, magnetic coherence length $\xi_{\rm M}$ characterizes the size of each unit patch and the area of each current sheet. The typical strength of the magnetic field B is the strength of magnetic fields on both sides of the current sheet because almost all the space is filled by these regions. As will be turned out in discussions in Sec. 4.5.1, the kinetic energy is dominated by the outflow rather than the inflow. Then, the characteristic length scale for the velocity field is the thickness of the current sheet, which can be identified as $\xi_{\rm K}$ [37]. Also, the root-mean-square velocity v can be approximated by the outflow energy as [37]

$$\frac{v^2}{2} = \frac{\xi_{\rm K}}{\xi_{\rm M}} \frac{v_{\rm out}^2}{2}, \tag{4.47}$$

by taking into account dilution by the volume ratio of a current sheet to a unit patch.

Now let us introduce the reconnection time scale. Since the magnetic field flux $\Phi = B\xi_{\rm M}^2$ in each patch is being processed on the current sheet with the inflow velocity $v_{\rm in}$, we obtain $\dot{\Phi} = B\xi_{\rm M} v_{\rm in} = \Phi/\tau_{\rm rec}$, where [78]

$$\tau_{\rm rec} := \frac{\xi_{\rm M}}{v_{\rm in}} \tag{4.48}$$

is the characteristic time scale (See panel (b) in Fig. 4.7). The expression of $v_{\rm in}$ in terms of $B, \xi_{\rm M}, v$ and $\xi_{\rm K}$ depends on regimes and will be discussed in each subsection in Sec. 4.5.1.

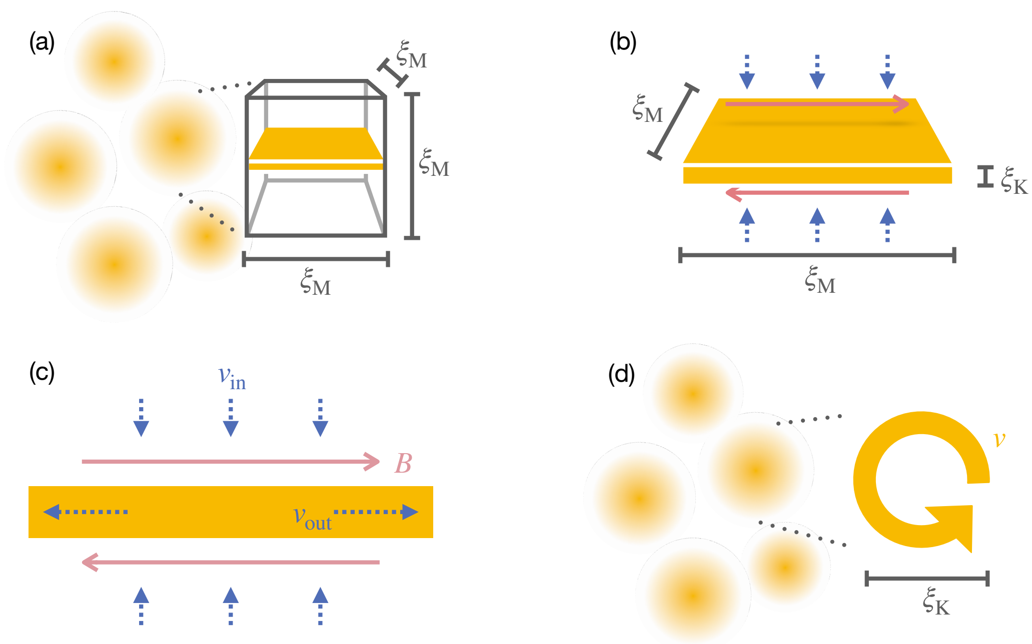

Figure 4.5: Mechanisms of the energy decay in non-linear regimes. (a–c) Magnetic reconnection is operating on a current sheet (orange-shaded) in each coherent patch (gray-outlined box). Anti-parallel magnetic fields on both sides of the sheet (red solid arrows) are inflowing into the sheet (vertical blue-dotted arrows), and a portion of the inflowing energy is converted into outflow from the sheet (horizontal blue-dotted arrows). (d) The time scale of the energy cascade of velocity field is controlled by the largest eddies (thick orange arrow) in the cascading process.

4.3.2 Eddy turnover time

Suppose that kinetic energy dominates over magnetic energy, and the process of energy decay is non-linear. Then, the relevant mechanism is the energy cascade from large eddies to small eddies, which we already explained in Sec. 4.2.3.

Let us look at panel (d) of Fig. 4.5. The velocity field consists of various sizes of eddies, each of them has its characteristic decay time scale $\tau_{\text{eddy}}(\xi)$ defined in Eq. (4.35), where ξ is the size of the eddy. Typically, smaller eddies take a shorter time to decay. Therefore, the peak of the kinetic energy spectrum is located at the size of the largest eddies in the cascading process (thick orange arrow), which we identify as the kinetic coherence length ξ_{K}. Also, the rate of dissipating energy in the whole process is controlled by the eddy turnover time of the largest eddies τ_{eddy} [29], which is defined in Eq. (4.37).

For the later purpose, we have to mention that, even when the non-linear cascading process is absent and the dynamics is linear, the characteristic time scale of a linear dynamics is given by the eddy turnover time at the kinetic coherence length τ_{eddy}, which is obtained by the dimensional consideration.

4.3.3 Dissipation time scales

For now, we ignore the non-linear terms and estimate characteristic time scales of linear dissipation processes. Since we have three dissipation terms in Eqs. (3.2) and (3.3), we introduce three time scales for each term.

As for the shear viscosity, we have contributions to $\dot{\boldsymbol{v}}$ in the form $\eta\nabla\nabla v$. At a length scale ξ, we may approximate the spatial derivatives by the inverse of the length ξ^{-1}. Then, the contribution at the scale ξ is $\dot{v}(\xi) \sim -v(\xi)/\tau_\eta(\xi)$, where

$$\tau_\eta(\xi) := \eta^{-1}\xi^2 \tag{4.49}$$

is the scale-wise dissipation time scale for the shear viscosity.

As for the drag force, we have a contribution $-\alpha\boldsymbol{v}$ to $\dot{\boldsymbol{v}}$. Then, the contribution is scale-independently $\dot{v}(\xi) \sim -v(\xi)/\tau_\alpha$, where

$$\tau_\alpha := \alpha^{-1} \tag{4.50}$$

is the dissipation time scale for the drag force.

As for the resistivity, we have contributions to $\dot{\boldsymbol{B}}$ in the form $\sigma^{-1}\nabla\nabla v$. At a length scale ξ, similarly to the discussion for the shear viscosity, the contribution can be approximated by $\dot{B}(\xi) \sim -B(\xi)/\tau_\sigma(\xi)$, where

$$\tau_\sigma(\xi) := \sigma\xi^2 \tag{4.51}$$

is the scale-wise dissipation time scale for the resistivity. If we compare $\tau_\sigma(\xi)$ to $\tau_\eta(\xi)$, their ratio is given by the magnetic Prandtl number defined in Eq. (4.46),

$$\frac{\tau_\sigma(\xi)}{\tau_\eta(\xi)} = \mathrm{Pr_M}. \tag{4.52}$$

The largeness of $\mathrm{Pr_M}$ in the early universe [29] implies that the linear dissipation process through the channel of resistivity is much slower than that of shear viscosity at every scale. This explains why we neglect finite resistivity in the early universe.

4.4 Classification of the regimes

In the previous sections, we listed several conserved quantities (Sec. 4.2) and decay time scales (Sec. 4.3) of the system. In this section, we explain which one is relevant under what conditions. We classify different regimes by several dichotomous criteria and give qualitative descriptions of what determines the dynamics of the system. Let us unifiedly summarize the classification criteria of the possible regimes before discussing the evolution laws in each regime.

4.4.1 Energy ratio

The first dichotomy, which we refer to as criterion A in Sec. 4.4.6, is whether the total energy is dominated by the magnetic field or the velocity field. Let us define the energy ratio of these fields [29]

$$\Gamma := \frac{(\rho + p)v^2}{B^2}. \tag{4.53}$$

When $\Gamma \ll 1$, it implies that the energy of the system is dominated by the magnetic field. In this case, magnetic energy cannot be directly dissipated away out of the system because dissipation by the finite resistivity is so slow compared with the dissipation by the shear viscosity, as discussed around Eq. (4.52). Instead, magnetic energy is first transferred to the velocity field by some mechanisms, and then dissipated due to the shear viscosity η or the drag force α. The mechanism of transferring magnetic energy into the velocity field depends on how large the magnetic Reynolds number, which will be introduced in Sec. 4.4.3, is. During the process of the energy decaying, a relevant conserved quantity constrains the dynamics. The relevant one is either magnetic helicity or Hosking integral, according to the helicity fraction. Kinetic energy at large scales is not necessarily conserved because energy injection from the magnetic field is significant. We discuss this class of regimes in Secs. 4.5.1 and 4.5.2.

When $\Gamma \gtrsim 1$, on the other hand, it implies that the kinetic energy dominates the total energy. Then, the energy can directly go away due to the shear viscosity η or the drag force α. Actually, according to numerical studies [34], even if we start from $\Gamma \gg 1$, quasi-equipartition $\Gamma \sim 1$ is achieved quickly because of the dynamo amplification at small scales. Therefore, in this thesis, we do not distinguish the initial Γ slightly larger than unity from this classification. The fate of this quasi-equipartition is not well-established. However, theoretical speculations [37] expect that it is completely different according to the helicity fraction. If the kinetic dominance of the energy is maintained, implying that the dynamics is primally governed by the velocity field, the conservation of kinetic energy at large scales holds. Then, Eq. (4.42) constrains the decay laws. We have room to discuss whether we should care also about the conservation of magnetic helicity and Hosking integral in this regime. We discuss this class of regimes in Secs. 4.5.3 and 4.5.4.

4.4.2 Helicity fraction

The second dichotomy, which we refer to as criterion B, is whether the magnetic field is maximally helical or non-helical. We already defined the helicity fraction of the magnetic field ϵ in Eq. (4.16).

When $|\epsilon| = 1$, the magnetic field is maximally helical, and Eq. (4.19) constrains the dynamics, regardless of the other dichotomies. The magnetic energy at large scales is enhanced because of the constraint, implying that the magnetic energy at smaller scales is transferred to the larger scales. This process is conventionally, but not always, referred to as the inverse cascade, although criticism about the terminology exists [81]. In this thesis, we call it inverse transfer regardless of the helicity fraction. The other constraint (4.33) is not relevant because Hosking integral is ill-defined for helical magnetic field, as is explained in Sec. 4.2.2. We discuss this class of regimes in Secs. 4.5.1.1–4.5.1.4, 4.5.2.1, 4.5.2.2, and 4.5.3.

Note that, if we start from tiny but nonzero helicity fraction $0 < |\epsilon| \ll 1$, the decay law will be approximated as the non-helical one at the beginning. However, the decay of non-helical magnetic field energy according to Eq. (4.33) is so fast that the inequality (4.18) is saturated at some point of the subsequent evolution. Then, the decay law switches to maximally helical one if we identify the point where Eq. (4.18) is saturated for the first time as the initial condition. We may reexpress this constraint as

$$B^2\xi_{\mathrm{M}} = |\epsilon_{\mathrm{ini}}|B^2_{\mathrm{ini}}\xi_{\mathrm{M,ini}} \quad \text{after } |\epsilon| \text{ reaches unity,} \tag{4.54}$$

for such a case.

When $\epsilon = 0$, the magnetic field is non-helical. In this case, the conservation of magnetic helicity does not constrain the dynamics of B and ξ_{M}. Rather, the conservation of the Hosking integral, Eq. (4.33), is relevant. We discuss this class of regimes in Secs. 4.5.1.5–4.5.1.8, 4.5.2.3, 4.5.2.4, and 4.5.4.

4.4.3 Reynolds numbers

The third dichotomy, criterion C in Sec. 4.4.6, is whether the dynamics is linear or not. We parametrize the non-linearity of the system, by taking the ratio of the non-linear and linear terms in Eqs. (3.2) and (3.3). As for the induction equation, we define the magnetic Reynolds number

$$\mathrm{Re}_{\mathrm{M}} := \frac{\sigma v \xi_{\mathrm{M}}^2}{\min\{\xi_{\mathrm{M}}, \xi_{\mathrm{K}}\}}, \tag{4.55}$$

where we estimate $|\boldsymbol{\nabla} \times (\boldsymbol{v} \times \boldsymbol{B})| \sim vB/\min\{\xi_{\mathrm{M}}, \xi_{\mathrm{K}}\}$ and $|\nabla^2 \boldsymbol{B}/\sigma| \sim B/\left(\sigma \xi_{\mathrm{M}}^2\right)$ [44]. As for Navier–Stokes equation, we define the kinetic Reynolds number

$$\mathrm{Re}_{\mathrm{K}} := \frac{v\xi_{\mathrm{K}}}{\max\{\eta, \alpha\xi_{\mathrm{K}}^2\}}, \tag{4.56}$$

where we estimate $|(\boldsymbol{v} \cdot \boldsymbol{\nabla})\,\boldsymbol{v}| \sim v^2/\xi_{\mathrm{K}}$ and $|\eta\,[\cdots] - \alpha\boldsymbol{v}| \sim \max\{\eta v/\xi_{\mathrm{K}}^2, \alpha v\}$ [44].

We have two Reynolds numbers, and which one plays the crucial role depends on criterion A, *i.e.*, whether the magnetic field is energetically dominant or not.

If $\Gamma \ll 1$ and magnetic energy is dominant, magnetic Reynolds number Re_{M} provides us with the following useful criterion. When $\mathrm{Re}_{\mathrm{M}} \gg 1$, it implies that the magnetic field is in a non-linear regime. We identify the process occurring in this class of regimes as the magnetic reconnection [37, 44]. We address these regimes in Sec. 4.5.1. When $\mathrm{Re}_{\mathrm{M}} \ll 1$, the magnetic field is in a linear regime. A large magnetic Prandtl number implies that magnetic field energy is not directly dissipated into heat. Rather, magnetic field first excites kinetic energy, and the kinetic energy is dissipated by the dissipation terms for the velocity field [29, 82]. We discuss this class of regimes in Sec. 4.5.2.

If $\Gamma \gtrsim 1$, then the kinetic Reynolds number primarily matters, since the velocity field governs the dynamics of the system. When $\mathrm{Re}_{\mathrm{K}} \gg 1$, the velocity field is in the non-linear kinetic turbulence. It is a cascading process of the eddies from large scales down to the smallest scales, where the scale-wise dissipation time scales are enough short to dissipate the energy within a Hubble time. This class of a regime is discussed in Sec. 4.5.4.1. If $\mathrm{Re}_{\mathrm{K}} \ll 1$, the velocity field is in a linear regime. They are directly dissipated by the dissipation terms at the coherence length scale. We discuss this class of regimes in Secs. 4.5.4.2 and 4.5.4.3.

4.4.4 Dominant dissipation term

We refer to the remaining dichotomies as criteria D in Sec. 4.4.6. One of them is which dissipation term is the dominant one. We have three dissipation coefficients in Eqs. (3.2) and (3.3), namely the resistivity σ^{-1}, shear viscosity η, and drag coefficient α. The large Prandtl number in the early universe implies that the resistivity can be basically ignored, although it plays a crucial role in the magnetic reconnection. We will explain this point in the next Sec. 4.4.5. As for the comparison between η and α, let us introduce a parameter [44]

$$r_{\text{diss}}(\xi) := \frac{\tau_\eta(\xi)}{\tau_\alpha} = \frac{\alpha\xi^2}{\eta}, \tag{4.57}$$

where we have substituted Eqs. (4.49) and (4.50) in the second equality, to judge which contribution is the dominant dissipation source for the velocity field. Basically, we evaluate this quantity at the kinetic coherence length ξ_{K}, except for the fast reconnection regimes, where the dissipation terms play crucial roles at much smaller length scales. To avoid confusion, at which scale r_{diss} is evaluated will be explicit in the discussion in each regime.

When $r_{\text{diss}} \ll 1$, dissipation by the shear viscosity is much faster at the relevant length scale. Therefore, we do not have to care about the drag term. We discuss this class of regimes in Secs. 4.5.1.1, 4.5.1.2, 4.5.1.5, 4.5.1.6, and 4.5.4.2.

When $r_{\text{diss}} \gg 1$, on the other hand, drag force dominates over the shear viscosity at the relevant length scale. In that case, we ignore the shear viscosity. We discuss this class of regimes in Secs. 4.5.1.3, 4.5.1.4, 4.5.1.7, 4.5.1.8, and 4.5.4.3.

4.4.5 Lundquist number

The other dichotomy in criteria D distinguishes different reconnection mechanisms in the regimes with $\Gamma \ll 1$ and $\text{Re}_{\text{M}} \gg 1$. A rough qualitative explanation of magnetic reconnection is already given in Sec. 4.3.1, where we explained that anti-parallel magnetic field lines annihilate on the current sheets. However, this is contradictory to the Alfvén's theorem [63, 64] explained in Sec. 4.2.1 because the theorem guarantees that magnetic flux is frozen into the fluid and prohibits reconnection in the large conductivity limit, $\sigma \to \infty$. Therefore, the finite electric conductivity or, equivalently, the non-zero resistivity is crucial in magnetic reconnection. Let us define a dimensionless parameter called the Lundquist number [43, 45, 83]

$$S := \frac{\tau_\sigma(\xi_{\text{M}})}{\xi_{\text{M}}/v_{\text{out}}} = \sigma v_{\text{out}} \xi_{\text{M}}, \tag{4.58}$$

which quantifies how significant the dissipation by the finite electric conductivity is for the outflow inside the current sheets.

We have an empirical value of the critical Lundquist number $S_\mathrm{c} \sim 10^4$ [80,84–86], above which too large Lundquist number leads to an instability of the current sheet. On one hand, when $S \ll S_\mathrm{c}$, magnetic reconnection operates on quasi-stationary current sheets, as is simply modeled by Refs. [77,78] and later extended by Ref. [79]. We call this regime as the Sweet–Parker reconnection regime and discuss it in Secs. 4.5.1.1, 4.5.1.3, 4.5.1.5, and 4.5.1.7.

If $S \gg S_\mathrm{c}$, however, the structure of the current sheet becomes unstable. Then another hierarchical structure involving plasmoids governs the dynamics [80,83]. The structure is visualized and will be explained in Fig. 4.8. We call this regime the fast reconnection regime, following the literature [43], and address it in Secs. 4.5.1.2, 4.5.1.4, 4.5.1.6, and 4.5.1.8.

4.4.6 Classification summary

We classify the system into four branches of regimes and a few regimes for each branch, according to the criteria A–D introduced in Secs. 4.4.1–4.4.5. We will explain the way to obtain analytic decay laws in each regime in Sec. 4.5.

Let us look at Fig. 4.6. We first classify the regimes according to criterion A. When $\Gamma \ll 1$, then the system is magnetically dominated. Otherwise, if $\Gamma \gtrsim 1$, then the system is kinetically dominated. For magnetically dominated regimes, we next consider criterion C. When $\mathrm{Re}_\mathrm{M} \gg 1$, then the system is non-linear. We expect that magnetic reconnection is the dominant process. This is one of the major classifications of regimes and will be investigated in Sec. 4.5.1 (MD-NL branch in Fig. 4.6). When $\mathrm{Re}_\mathrm{M} \ll 1$, then the system is linear. This is another classification of regimes, and we will study it in Sec. 4.5.2 (MD-L branch in Fig. 4.6). For kinetically dominated regimes, on the other hand, we consider criterion B. When $|\epsilon| = 1$, the system is maximally helical. This is also one of the major classifications of regimes and will be investigated in Sec. 4.5.3 (KD-MH branch in Fig. 4.6). When $|\epsilon| = 0$, the system is non-helical. This major classification of regimes will be investigated in

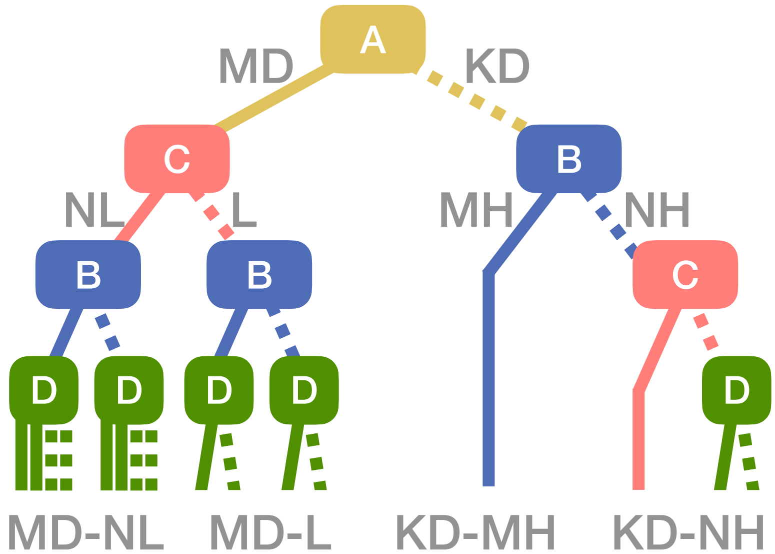

Figure 4.6: Classification of the regimes according to the criteria A–D. We have four branches of regimes, magnetically dominated and non-linear (MD-NL) branch, magnetically dominated and linear (MD-L) branch, kinetically dominated and maximally helical (KD-MH) branch, and kinetically dominated and non-helical (KD-NH) branch. Each branch has a few regimes, which adds up to sixteen in total.

Sec. 4.5.4 (KD-NH branch in Fig. 4.6).

Each of the four branches of regimes introduced above is further classified into a few regimes. The magnetically dominated and non-linear branch has maximally helical and non-helical sub-branches of regimes according to criterion B, and each of them is devided into four regimes according to criteria D. Viscous and Sweet–Parker reconnection regimes with $r_{\rm diss} \ll 1$ and $S \ll S_{\rm c}$ are discussed in Secs. 4.5.1.1 and 4.5.1.5. Viscous and fast reconnection regimes with $r_{\rm diss} \ll 1$ and $S \gg S_{\rm c}$ are discussed in Secs. 4.5.1.2 and 4.5.1.6. Dragged and Sweet–Parker reconnection regimes with $r_{\rm diss} \gg 1$ and $S \ll S_{\rm c}$ are discussed in Secs. 4.5.1.3 and 4.5.1.7. Dragged and fast reconnection regimes with $r_{\rm diss} \gg 1$ and $S \gg S_{\rm c}$ are discussed in Secs. 4.5.1.4 and 4.5.1.8. Note that the Lundquist number S matters only in this branch of regimes. The magnetically dominated and linear branch also has maximally helical and non-helical sub-branches of regimes according to criterion B, and each of them is divided into two regimes according to r_{diss}. Viscous regimes with $r_{\text{diss}} \ll 1$ are discussed in Secs. 4.5.2.1 and 4.5.2.3. Dragged regimes with $r_{\text{diss}} \gg 1$ are discussed in Secs. 4.5.2.2 and 4.5.2.4. The kinetically dominated and maximally helical branch consists of only one regime. The kinetically dominated and non-helical branch has non-linear and linear sub-branches of regimes according to criterion C. The non-linear sub-branch consists of only one regime discussed in Sec. 4.5.4.1. The linear sub-branch is divided into two regimes according to r_{diss}. The viscous regime with $r_{\text{diss}} \ll 1$ is discussed in Sec. 4.5.4.2. The dragged regime with $r_{\text{diss}} \gg 1$ is discussed in Sec. 4.5.4.3.

Then, we have sixteen regimes in total. We summarize the classification of the regimes and where to look for the results in Table 4.1.

4.5 Regime dependent analyses

According to the classification of the regimes, we analyze the evolution of the system in each regime. While the analyses for the regimes in Secs. 4.5.1.6 and 4.5.3 follow the ones in Refs. [37, 43], the analyses in the remaining regimes are studied in our works [44, 45]. In the derivation of the scaling solutions, we assume that the system is not frozen ever since τ_{ini}. Then, Eq. (4.4) is reduced to Eq. (4.3). The frozen regimes are explained later in Chap. 5. The equations we solve in each regime are summarised altogether in simple forms in Appendix F.

4.5.1 Magnetically dominated and non-linear regimes

In this branch of regimes, magnetic energy dominates over kinetic energy, and magnetic reconnection is continuously dissipating magnetic energy into both heat and outflow velocity. Conditions

$$\Gamma \ll 1, \quad \mathrm{Re}_{\mathrm{M}} \gg 1 \tag{4.59}$$

are satisfied. As depicted in panels (a), (b), and (c) of Fig. 4.5, the system is characterized by six variables, B, ξ_{M}, v, ξ_{K}, v_{in}, and v_{out}. We have several regimes

Regime		Sec.	Conserved quantity	Decay time scale	Scaling solution
$\Gamma \ll 1$, $\mathrm{Re}_{\mathrm{M}} \gg 1$ (MD-NL)	$\lvert\epsilon\rvert = 1, r_{\mathrm{diss}} \ll 1$, $S \ll S_{\mathrm{c}}$	4.5.1.1	$B^2\xi_{\mathrm{M}}$	(4.75)	(4.77) (4.78)
	$\lvert\epsilon\rvert = 1, r_{\mathrm{diss}} \ll 1$, $S \gg S_{\mathrm{c}}$	4.5.1.2		(4.96)	(4.97) (4.98)
	$\lvert\epsilon\rvert = 1, r_{\mathrm{diss}} \gg 1$, $S \ll S_{\mathrm{c}}$	4.5.1.3		(4.105)	(4.107) (4.108)
	$\lvert\epsilon\rvert = 1, r_{\mathrm{diss}} \gg 1$, $S \gg S_{\mathrm{c}}$	4.5.1.4		(4.112)	(4.113) (4.114)
	$\epsilon = 0, r_{\mathrm{diss}} \ll 1$, $S \ll S_{\mathrm{c}}$	4.5.1.5	$B^4\xi_{\mathrm{M}}^5$	(4.75)	(4.116) (4.117)
	$\epsilon = 0, r_{\mathrm{diss}} \ll 1$, $S \gg S_{\mathrm{c}}$	4.5.1.6		(4.96)	(4.119) (4.120)
	$\epsilon = 0, r_{\mathrm{diss}} \gg 1$, $S \ll S_{\mathrm{c}}$	4.5.1.7		(4.105)	(4.122) (4.123)
	$\epsilon = 0, r_{\mathrm{diss}} \gg 1$, $S \gg S_{\mathrm{c}}$	4.5.1.8		(4.112)	(4.125) (4.126)
$\Gamma \ll 1$, $\mathrm{Re}_{\mathrm{M}} \ll 1$ (MD-L)	$\lvert\epsilon\rvert = 1$, $r_{\mathrm{diss}} \ll 1$	4.5.2.1	$B^2\xi_{\mathrm{M}}$	(4.134)	(4.135) (4.136)
	$\lvert\epsilon\rvert = 1$, $r_{\mathrm{diss}} \gg 1$	4.5.2.2		(4.141)	(4.142) (4.143)
	$\epsilon = 0$, $r_{\mathrm{diss}} \ll 1$	4.5.2.3	$B^4\xi_{\mathrm{M}}^5$	(4.134)	(4.145) (4.146)
	$\epsilon = 0$, $r_{\mathrm{diss}} \gg 1$	4.5.2.4		(4.141)	(4.148) (4.149)
$\Gamma \gtrsim 1, \lvert\epsilon\rvert = 1$ (KD-MH)		4.5.3			$\to$ MD
$\Gamma \gtrsim 1$, $\epsilon = 0$ (KD-NH)	$\mathrm{Re}_{\mathrm{K}} \gg 1$	4.5.4.1	$B^2\xi_{\mathrm{M}}^{n+3}$	(4.162)	(4.160) (4.161)
	$\mathrm{Re}_{\mathrm{K}} \ll 1$, $r_{\mathrm{diss}} \ll 1$	4.5.4.2		(4.168)	(4.166) (4.167)
	$\mathrm{Re}_{\mathrm{K}} \ll 1$, $r_{\mathrm{diss}} \gg 1$	4.5.4.3		τ_α	$\to$ MD

Table 4.1: Classification and the scaling solutions in the sixteen regimes. Scaling solutions are obtained by considering the conserved quantities and the decay time scales in terms of the magnetic field.

within this branch according to the helicity fraction ϵ, the ratio of dissipation terms $r_{\rm diss}$, and the Lundquist number S. We extend the analysis in the literature [37, 43, 77–79] to find six equations for each subregime [44, 45]. By solving them, we find formulas that describe the evolution of the system in each regime.

4.5.1.1 Maximally helical and viscous Sweet–Parker regime

In this regime, magnetic field is maximally helical, shear viscosity dominates over drag force, and the Lundquist number is relatively small. In addition to Eq. (4.59),

$$|\epsilon| = 1, \quad r_{\rm diss}(\xi_{\rm K}) \ll 1, \quad S \ll S_{\rm c} \tag{4.60}$$

are satisfied. The mechanism that governs the evolution of the system is Sweet–Parker reconnection with shear viscosity.

Let us follow Refs. [77–79] to find relations between the six variables. Look at panel (c) of Fig. 4.5. The mass conservation on each current sheet implies [78]

$$v_{\rm in}\xi_{\rm M} = v_{\rm out}\xi_{\rm K}, \tag{4.61}$$

where the left and right hand sides represent the rate of incoming and outgoing mass, respectively. Another condition is the stationarity of the current sheet. If we focus only on the structure across the current sheet, by assuming a large aspect ratio $\xi_{\rm M} \gg \xi_{\rm K}$, we can replace the spatial derivative $\boldsymbol{\nabla}$ in the induction equation (3.2) by $1/\xi_{\rm K}$ (panel (a) of Fig. 4.7). As for the term $\boldsymbol{\nabla} \times (\boldsymbol{v} \times \boldsymbol{B})$, we have $|\boldsymbol{v} \times \boldsymbol{B}| \sim v_{\rm in} B$ outside the sheet, while $|\boldsymbol{v} \times \boldsymbol{B}| \sim 0$ inside the sheet. Since the outside and the inside are separated by the width of the sheet $\xi_{\rm K}$, we estimate $|\boldsymbol{\nabla} \times (\boldsymbol{v} \times \boldsymbol{B})| \sim v_{\rm in} B/\xi_{\rm K}$. As for the term $\sigma^{-1}\nabla^2\boldsymbol{B}$, we have opposite directions of magnetic field $|\boldsymbol{B}| \sim B$ on both sides of the sheet, while $|\boldsymbol{B}| \sim 0$ inside. Therefore, we estimate $|\sigma^{-1}\nabla^2\boldsymbol{B}| \sim B/\sigma\xi_{\rm K}^2$. Then, the balance between terms in the induction equation (3.2) implies [78]

$$\frac{v_{\rm in} B}{\xi_{\rm K}} = \frac{B}{\sigma\xi_{\rm K}^2}. \tag{4.62}$$

For convenience, we use Eqs. (4.61) and (4.62) to obtain an expression of the outflow velocity in terms of the coherence lengths,

$$v_{\rm out} = \frac{\xi_{\rm M}}{\sigma\xi_{\rm K}^2}. \tag{4.63}$$

Energy dissipation of the outflow along the current sheet implies

$$\frac{B^2}{2} = \frac{\rho + p}{2} v_{\mathrm{out}}^2 + \int_0^{\xi_{\mathrm{M}}/2} \frac{d\xi}{v_{\mathrm{out}}} \frac{(\rho + p)\eta v_{\mathrm{out}}^2}{\xi_{\mathrm{K}}^2}, \tag{4.64}$$

which is reduced to [79]

$$B^2 = (\rho + p)(1 + \mathrm{Pr}_{\mathrm{M}}) v_{\mathrm{out}}^2, \tag{4.65}$$

by approximating the integrand in Eq. (4.64) to be constant and using Eq. (4.63). The first term in the right hand side of Eq. (4.64) or the term 1 in Eq. (4.65) represents the energy of the outflow, while the second term in the right hand side of Eq. (4.64) or the term Pr_{M} in Eq. (4.65) represents the energy dissipation by the shear viscosity on the current sheet. Although the original idea of the Sweet–Parker model [77, 78] neglects the latter contribution, large Prandtl number $\mathrm{Pr}_{\mathrm{M}} \gg 1$ in the early universe implies that the former contribution is negligible but rather the latter one is the dominant. Then we approximate Eq. (4.65) as

$$B^2 = (\rho + p)\mathrm{Pr}_{\mathrm{M}} v_{\mathrm{out}}^2. \tag{4.66}$$

The condition about decay time scales, Eq. (4.3), implies [37]

$$\tau_{\mathrm{rec}} = \tau, \tag{4.67}$$

where the reconnection time scale τ_{rec} is given by Eq. (4.48) (panel (b) of Fig. 4.7). Finally, the kinetic energy in each coherent patch is dominated by the outflow, and the typical velocity v is obtained from Eq. (4.47). Neglecting the contribution of the inflow velocity is justified by confirming $v_{\mathrm{in}} \ll v$ in the final expression.

Let us summarize what we have to solve. We need to solve Eqs. (4.61), (4.62), (4.66), (4.67), and (4.47) together with the helicity conservation, Eq. (4.19). In addition, we have two assumptions for the solution, which guarantee that the set of equations is reasonable. One is the large aspect ratio of the current sheet,

$$\frac{\xi_{\mathrm{M}}}{\xi_{\mathrm{K}}} \gg 1, \tag{4.68}$$

and the other is the small inflow velocity,

$$\frac{v_{\rm in}}{v} \ll 1. \tag{4.69}$$

They will be justified after solving the set of equations.

To solve the set of equations, let us go stepwise and see which equations lead to which results. First, we express quantities about the velocity field in terms of B and $\xi_{\rm M}$. By using the condition about the decay time scale, Eq. (4.67), we obtain

$$v_{\rm in} = \tau^{-1}\xi_{\rm M}. \tag{4.70}$$

We substitute this expression into the stationarity condition, Eq. (4.62), to obtain an expression of the kinetic coherence length $\xi_{\rm K}$, substitute the resultant expression into Eq. (4.63) to obtain an expression of the outflow velocity $v_{\rm out}$, and finally obtain an expression of the typical velocity v by considering the energy dilution, Eq. (4.47). Then we obtain

$$\xi_{\rm K} = \sigma^{-1}\tau\xi_{\rm M}^{-1}, \quad v_{\rm out} = \sigma\tau^{-2}\xi_{\rm M}^{3}, \quad v = \sigma^{\frac{1}{2}}\tau^{-\frac{3}{2}}\xi_{\rm M}^{2}. \tag{4.71}$$

Before going to the next step, we express the order parameters in terms of B and $\xi_{\rm M}$ as well, by substituting Eqs. (4.70) and (4.71) into the definitions, Eqs. (4.53), (4.55), (4.57), and (4.58). The energy ratio and the magnetic Reynolds number are

$$\Gamma = (\rho+p)\sigma\tau^{-3}B^{-2}\xi_{\rm M}^{4}, \quad {\rm Re}_{\rm M} = \left(\frac{\xi_{\rm M}}{\sigma^{-\frac{1}{2}}\tau^{\frac{1}{2}}}\right)^{5}, \tag{4.72}$$

in terms of which the ratio of dissipation terms evaluated at the kinetic coherence length and the Lundquist number are

$$r_{\rm diss}(\xi_{\rm K}) = {\rm Pr}_{\rm M}^{-1}{\rm Re}_{\rm M}^{-\frac{2}{5}}\alpha\tau, \quad S = {\rm Re}_{\rm M}^{\frac{4}{5}}. \tag{4.73}$$

Also, the largeness of the aspect ratio, Eq. (4.68), and the smallness of the inflow velocity, Eq. (4.69), are guaranteed by the large magnetic Reynolds number because

$$\frac{\xi_{\rm M}}{\xi_{\rm K}} = {\rm Re}_{\rm M}^{\frac{2}{5}}, \quad \frac{v_{\rm in}}{v} = {\rm Re}_{\rm M}^{-\frac{1}{5}} \tag{4.74}$$

are derived from Eqs. (4.70) and (4.71).

The next step is the use of Eq. (4.66). By substituting the expression of the outflow velocity v_{out}, we obtain

$$(\rho+p)^{\frac{1}{4}}\sigma^{\frac{3}{4}}\eta^{\frac{1}{4}}B^{-\frac{1}{2}}\xi_{\text{M}}^{\frac{3}{2}}=\tau, \tag{4.75}$$

which corresponds to Eq. (4.3), although the discussion here is not as simple as the one in Sec. 4.1. We can relate Γ and Re_{M} by employing this condition and the expression in Eq. (4.72) as

$$\Gamma=\text{Pr}_{\text{M}}^{-1}\text{Re}_{\text{M}}^{-\frac{2}{5}}. \tag{4.76}$$

Finally, by solving the conservation law, Eq. (4.19), and the time-dependent condition, Eq. (4.75), we obtain

$$B=B_{\text{ini}}^{\frac{6}{7}}\xi_{\text{M,ini}}^{\frac{3}{7}}(\rho+p)^{\frac{1}{14}}\sigma^{\frac{3}{14}}\eta^{\frac{1}{14}}\tau^{-\frac{2}{7}}, \tag{4.77}$$

$$\xi_{\text{M}}=B_{\text{ini}}^{\frac{2}{7}}\xi_{\text{M,ini}}^{\frac{1}{7}}(\rho+p)^{-\frac{1}{7}}\sigma^{-\frac{3}{7}}\eta^{-\frac{1}{7}}\tau^{\frac{4}{7}}. \tag{4.78}$$

As Ref. [43] pointed out for a drag force dominant regime, we should be careful about the effect of dissipation on the inflow. We have implicitly assumed in the above discussion that Sweet–Parker reconnection is the rate-determining process, although the inflow velocity can be limited rather by the dissipation of the inflow. To justify the assumption, let us consider the region away from the current sheet and suppose that the inflow velocity v'_{in} is determined by the dissipation effect. Then we will compare the two inflow speeds, v'_{in} and v_{in}.

In the region where the flow is laminar and stationary but the dissipation is significant, the energy injection from the magnetic field should balance with the energy dissipation [29]. By approximating the relevant terms in the Navier–Stokes equation (3.3) as

$$\left|\frac{(\boldsymbol{\nabla}\times\boldsymbol{B})\times\boldsymbol{B}}{\rho+p}\right|\sim\frac{B^2}{(\rho+p)\xi_{\text{M}}},\quad |\eta[\nabla^2\boldsymbol{v}+\cdots]|\sim\frac{\eta v'_{\text{in}}}{\xi_{\text{M}}^2} \tag{4.79}$$

and balancing these terms, we obtain an estimate of the inflow velocity

$$v'_{\text{in}}=\frac{B^2\xi_{\text{M}}}{(\rho+p)\eta}=\text{Re}_{\text{M}}^{\frac{6}{5}}v_{\text{in}}\gg v_{\text{in}}, \tag{4.80}$$

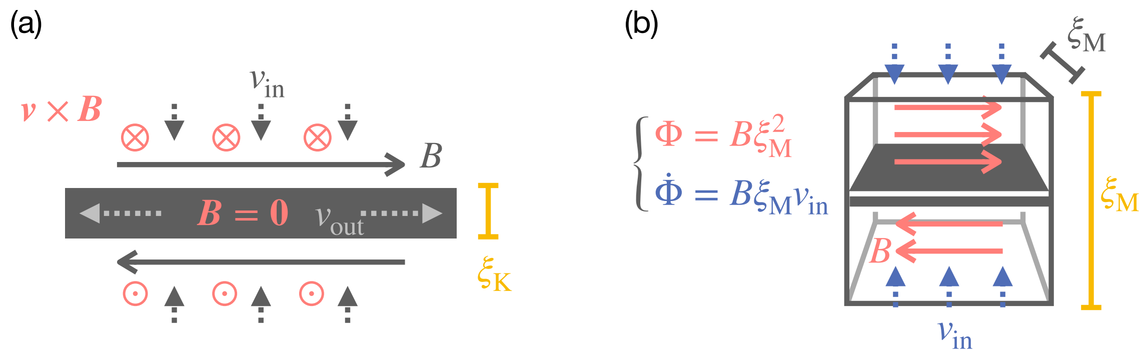

Figure 4.7: Illustrations of Sweet–Parker reconnection. (a) Magnetic field (gray solid arrows) is anti-parallel on both sides of the current sheet (gray-shaded region) and vanishes inside the sheet. Since the inflow velocity (gray-dotted arrows) is there, the Lorentz force $\boldsymbol{v} \times \boldsymbol{B}$ can be estimated to be $\sim v_{\rm in} B$ outside the sheet. (b) The time scale of the reconnection process can be identified as the rate of processing magnetic flux Φ. We have magnetic fluxes $\sim B\xi_{\rm M}^2$ (red solid arrows) in each half of the box separated by the current sheet (gray-shaded region). Because of the inflow velocity (blue-dotted arrows), each flux is processed as $\dot{\Phi} \sim B\xi_{\rm M} v_{\rm in}$, from which we can estimate the time scale to be $\Phi/\dot{\Phi} \sim \xi_{\rm M}/v_{\rm in} =: \tau_{\rm rec}$.

where we have used Eqs. (4.53), (4.69), (4.70), (4.72), and (4.76) in the second equality. The hierarchy between $v_{\rm in}$ and $v'_{\rm in}$ supports our assumption that the rate-determining process is magnetic reconnection. The inflow velocity $v_{\rm in}$ is so small that the estimated magnitudes of the two terms in Eq. (4.79) do not balance, implying that the magnetic field actually takes a force-free configuration,

$$(\boldsymbol{\nabla} \times \boldsymbol{B}) \times \boldsymbol{B} \ll \frac{B^2}{\xi_{\rm M}}, \tag{4.81}$$

of which observation in numerical studies can support our analysis.

4.5.1.2 Maximally helical and viscous fast reconnection regime

In this regime, magnetic field is maximally helical, shear viscosity dominates over drag force, and the Lundquist number is large. In addition to Eq. (4.59),

$$|\epsilon| = 1, \quad r_{\rm diss}(\xi_{\rm K}) \ll 1, \quad S \gg S_{\rm c} \tag{4.82}$$

are satisfied. The mechanism that governs the evolution of the system is no longer Sweet–Parker reconnection because the current sheet becomes unstable to form plasmoids that are connected by smaller current sheets [80, 84–86]. The ratio of dissipation terms may be evaluated at the width of the smallest current sheet involved in the mechanism, δ_c, which is explained within this section. Such a reconnection regime is referred to as the fast magnetic reconnection [43, 83].

Nevertheless, a similar analysis to the one in Sec. 4.5.1.1 is still possible by applying the same procedure to the so-called critical current sheets [43, 80, 83]. We model the system as depicted in Fig. 4.8, following Refs. [80, 87]. Macroscopically, the system looks similar to the Sweet–Parker one. We have a sheet-like structure of thickness ξ_K and area ξ_M^2 (orange-shaded region in panel (a)) in each unit patch of volume ξ_M^3. Magnetic field (red solid arrows) is anti-parallel on both sides of the structure, the fluid is inflowing onto the faces of the current sheet (vertical blue-dotted arrows), and it is outflowing from the narrow sides of the sheet (horizontal blue-dotted arrows). However, the sheet has a hierarchical structure inside it (panel (b)). The largest sheet in the hierarchy is of the size $\xi_M^2 \times \xi_K$ (the top orange-shaded region). It has plasmoids (dark blobs) inside it and is separated into smaller sheets of the second hierarchy (the middle orange-shaded region). The largest sheet is unstable and plasmoids inside it are continuously formed and ejected by the outflow. Similarly, each sheet in a hierarchy has smaller sheets in the next hierarchy because of the instability. If we assign Lundquist numbers for sheets in the i-th hierarchy as

$$S_i := \sigma v_{\text{out}} L_i, \tag{4.83}$$

where L_i is the typical length of the sheets, the hierarchical structure continues to the $(i+1)$-th hierarchy if $S_i \gg S_c$. However, for a given outflow velocity v_{out}, the hierarchy terminates at a length scale L_c because the condition

$$S_c = \sigma v_{\text{out}} L_c, \tag{4.84}$$

determines the size of the smallest sheets, which we refer to as the critical current sheet (the bottom orange-shaded region). If we parametrize the thickness of the critical current sheets as $\delta_{\rm c}$ and the inflow velocity onto them as $v_{\rm in}$, a parallel discussion to the Sweet–Parker one holds (panel (c)).

We assume that the reconnecting magnetic field B and the outflow velocity $v_{\rm out}$ are common in the hierarchy of the current sheets. From Eqs. (4.58) and (4.84), we obtain the critical size of the current sheets

$$L_{\rm c} = \frac{S_{\rm c}}{S}\xi_{\rm M}. \tag{4.85}$$

The consideration about mass conservation and (quasi-)stationarity in Sec. 4.5.1.1 for the Sweet–Parker current sheet applies to the critical sheets, and Eqs. (4.61), (4.62), and (4.63) analogously hold by replacing $\xi_{\rm M}$ with $L_{\rm c}$ and $\xi_{\rm K}$ with $\delta_{\rm c}$. Conditions about mass conservation and (quasi-)stationarity of the critical sheets imply

$$v_{\rm in}L_{\rm c} = v_{\rm out}\delta_{\rm c}, \quad \frac{v_{\rm in}B}{\delta_{\rm c}} = \frac{B}{\sigma\delta_{\rm c}^2}, \tag{4.86}$$

from which we obtain an expression of the outflow velocity

$$v_{\rm out} = \frac{L_{\rm c}}{\sigma\delta_{\rm c}^2}, \tag{4.87}$$

where we have substituted Eq. (4.85) in the second equality. We relate this with the magnetic field strength by considering macroscopic energy budget, Eq. (4.66). In addition, we have conditions about the decay time scale, Eq. (4.67), and the dilution of kinetic energy, Eq. (4.47).

Before solving them together with the helicity conservation, Eq. (4.19), let us estimate the kinetic coherence length $\xi_{\rm K}$. We assume that the aspect ratio of the unstable sheets is determined as if they are stable Sweet–Parker ones. In particular for the lowest hierarchy, we employ analogues of Eqs. (4.61) and (4.62) with an unknown inflow velocity that can be different from the inflow velocity onto the critical sheets, and hence we obtain Eq. (4.63). Then the kinetic coherence length can be expressed as [80]

$$\xi_{\rm K} = S^{-\frac{1}{2}}\xi_{\rm M}. \tag{4.88}$$

If we express $\delta_{\rm c}$ in terms of $\xi_{\rm K}$,

$$\delta_{\rm c} = S_{\rm c}^{-\frac{1}{2}}L_{\rm c} = \sqrt{\frac{S_{\rm c}}{S}}\xi_{\rm K}. \tag{4.89}$$

From Eqs. (4.85) and (4.89), it is clear that, when $S = S_\mathrm{c}$, $L_\mathrm{c} = \xi_\mathrm{M}$ and $\delta_\mathrm{c} = \xi_\mathrm{K}$ hold. Then, the solution reduces to the one in Sec. 4.5.1.1 because the difference of the analyses is just the replacement of ξ_M with L_c and ξ_K with δ_c.

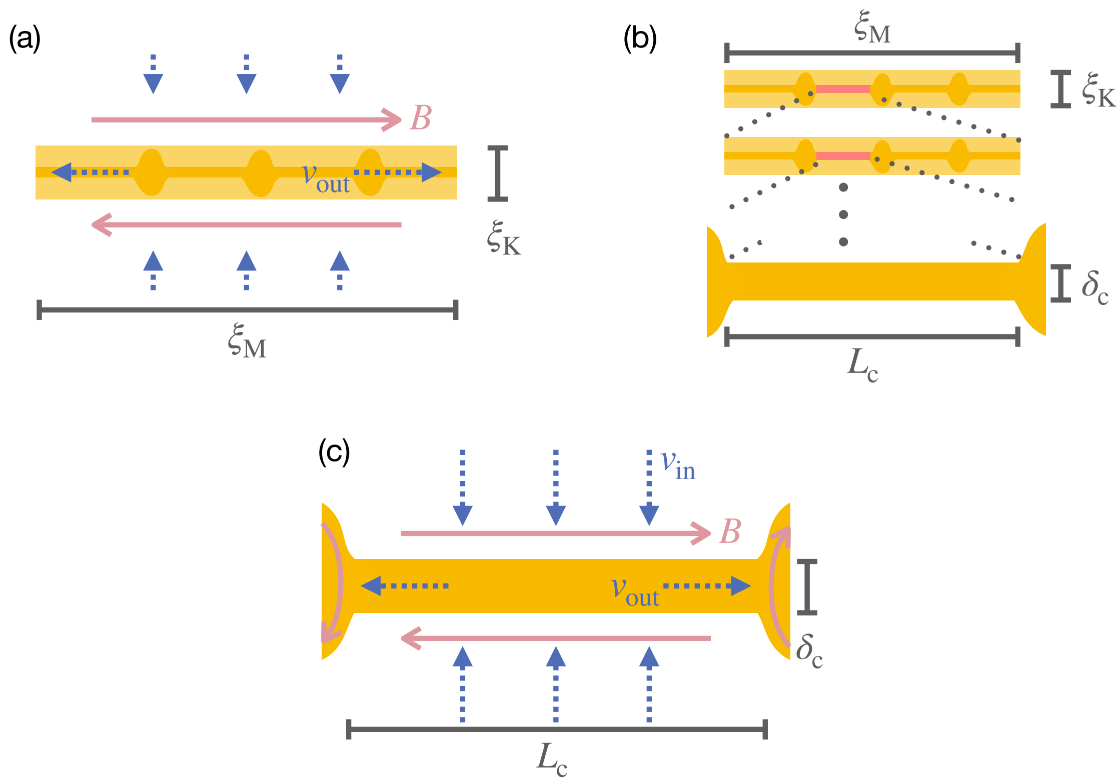

Figure 4.8: The structure of current sheets of the fast reconnection. (a) Sheets in the lowest hierarchy (orange-shaded region) determine the magnetic and kinetic coherence lengths. (b) The sheets have a hierarchical structure, in which each sheet has plasmoids (dark blobs) and smaller sheets in the next hierarchy, until the size reaches down to the critical length, L_c. (c) The critical sheets are similar to the Sweet–Parker current sheet because they do not suffer from the plasmoid instability.

Now let us solve the set of equations, (4.86), (4.66), (4.67), (4.47), and (4.19). Since we are interested in finding an expression of ξ_K rather than δ_c, we replace Eq. (4.86) with Eq. (4.88) and

$$v_\mathrm{in} = S_\mathrm{c}^{-\frac{1}{2}} v_\mathrm{out}, \tag{4.90}$$

which is derived from Eqs. (4.86) and (4.84).

We solve the set of equations step by step as we did in Sec. 4.5.1.1. First, we use the condition about the decay time scale, Eq. (4.67), to obtain Eq. (4.70). We substitute this expression into Eq. (4.90) to obtain

$$v_{\mathrm{out}} = S_{\mathrm{c}}^{\frac{1}{2}} \tau^{-1} \xi_{\mathrm{M}}. \tag{4.91}$$

Then the Lundquist number becomes $S = S_{\mathrm{c}}^{\frac{1}{2}} \sigma \tau^{-1} \xi_{\mathrm{M}}^{2}$, and we obtain expressions of the kinetic coherence length ξ_{K}, by using Eq. (4.88), and of the typical velocity v, by considering the energy dilution, Eq. (4.47). We obtain

$$\xi_{\mathrm{K}} = S_{\mathrm{c}}^{-\frac{1}{4}} \sigma^{-\frac{1}{2}} \tau^{\frac{1}{2}}, \quad v = S_{\mathrm{c}}^{\frac{3}{8}} \sigma^{-\frac{1}{4}} \tau^{-\frac{3}{4}} \xi_{\mathrm{M}}^{\frac{1}{2}}. \tag{4.92}$$

We express the order parameters in terms of B and ξ_{M} as well, by substituting Eqs. (4.70), (4.91), and (4.92) into the definitions, Eqs. (4.53), (4.55), (4.57), and (4.58). The energy ratio, the magnetic Reynolds number, and the ratio of dissipation terms become

$$\begin{gathered}
\Gamma = (\rho + p) S_{\mathrm{c}}^{\frac{3}{4}} \sigma^{-\frac{1}{2}} \tau^{-\frac{3}{2}} B^{-2} \xi_{\mathrm{M}}, \quad \mathrm{Re}_{\mathrm{M}} = \left(\frac{\xi_{\mathrm{M}}}{S_{\mathrm{c}}^{-\frac{1}{4}} \sigma^{-\frac{1}{2}} \tau^{\frac{1}{2}}} \right)^{\frac{5}{2}}, \\
r_{\mathrm{diss}}(\delta_{\mathrm{c}}) = \left(\frac{\xi_{\mathrm{M}}}{\sigma^{-1} \eta^{-\frac{1}{2}} \alpha^{\frac{1}{2}} \tau} \right)^{-2}, \quad r_{\mathrm{diss}}(\xi_{\mathrm{K}}) = S_{\mathrm{c}}^{-\frac{1}{2}} \mathrm{Pr}_{\mathrm{M}}^{-1} \alpha \tau,
\end{gathered} \tag{4.93}$$

in terms of which the Lundquist number has the same expression as in Sec. 4.5.1.1,

$$S = \mathrm{Re}_{\mathrm{M}}^{\frac{4}{5}}. \tag{4.94}$$

The largeness of the aspect ratio of the sheets and the smallness of the macroscopic inflow velocity are guaranteed because

$$\frac{\xi_{\mathrm{M}}}{\xi_{\mathrm{K}}} \left(= S^{\frac{1}{2}} \right) \gg \frac{L_{\mathrm{c}}}{\delta_{\mathrm{c}}} = S_{\mathrm{c}}^{\frac{1}{2}} \gg 1, \quad \frac{(S_{\mathrm{c}}/S)^{\frac{1}{2}} v_{\mathrm{in}}}{v} = S^{-\frac{1}{4}} \ll 1 \tag{4.95}$$

in this regime. Next, we substitute the expression of the outflow velocity, Eq. (4.91), into Eq. (4.66), to obtain [43, 83]

$$S_{\mathrm{c}}^{\frac{1}{2}} (\rho + p)^{\frac{1}{2}} \mathrm{Pr}_{\mathrm{M}}^{\frac{1}{2}} B^{-1} \xi_{\mathrm{M}} = \tau. \tag{4.96}$$

By using this, we can relate Γ with the magnetic Reynolds number in the same way as Eq. (4.76) in Sec. 4.5.1.1. Finally, we solve Eqs. (4.96) and (4.19) to obtain

$$B = B_{\mathrm{ini}}^{\frac{2}{3}} \xi_{\mathrm{ini}}^{\frac{1}{3}} S_{\mathrm{c}}^{\frac{1}{6}} (\rho + p)^{\frac{1}{6}} \sigma^{\frac{1}{6}} \eta^{\frac{1}{6}} \tau^{-\frac{1}{3}}, \tag{4.97}$$

$$\xi_{\mathrm{M}} = B_{\mathrm{ini}}^{\frac{2}{3}} \xi_{\mathrm{ini}}^{\frac{1}{3}} S_{\mathrm{c}}^{-\frac{1}{3}} (\rho + p)^{-\frac{1}{3}} \sigma^{-\frac{1}{3}} \eta^{-\frac{1}{3}} \tau^{\frac{2}{3}}. \tag{4.98}$$

We should be careful about the dissipation of the inflow [43]. The discussion here is parallel to the one in Sec. 4.5.1.1. Let us consider the region away from the current sheet and suppose that the inflow velocity v'_{in} is determined by the energy dissipation. In such a region, the energy injection from the magnetic field should balance with the energy dissipation [29]. By approximating the relevant terms in Navier–Stokes equation (3.3) as we do in Eq. (4.79) and balancing these terms, we obtain the same estimate of the inflow velocity as Eq. (4.80), which implies $v'_{\mathrm{in}} \gg v_{\mathrm{in}}$ and supports our assumption that the rate-determining process is magnetic reconnection.

4.5.1.3 Maximally helical and dragged Sweet–Parker regime

In this regime, magnetic field is maximally helical, drag force dominates over shear viscosity, and the Lundquist number is relatively small. In addition to Eq. (4.59),

$$|\epsilon| = 1, \quad r_{\mathrm{diss}}(\xi_{\mathrm{K}}) \gg 1, \quad S \ll S_{\mathrm{c}} \tag{4.99}$$

are satisfied. The mechanism that governs the evolution of the system is basically the Sweet–Parker reconnection, but the dissipation is due to the drag force rather than the shear viscosity [44]. Note that we are considering a different regime from the so-called collisionless regime [43, 80]. We assume that the fluid approximation of the plasma still holds.

We do the same discussion as in Sec. 4.5.1.1, except for the estimate of energy dissipation in Eq. (4.64). When the drag force dominates over shear viscosity, energy dissipation of the outflow along the current sheet implies

$$\frac{B^2}{2} = \frac{\rho + p}{2} v_{\mathrm{out}}^2 + \int_0^{\xi_{\mathrm{M}}/2} \frac{d\xi}{v_{\mathrm{out}}} (\rho + p) \alpha v_{\mathrm{out}}^2, \tag{4.100}$$

which is reduced to

$$B^2 = (\rho + p)(v_{\rm out}^2 + \alpha \xi_{\rm M} v_{\rm out}), \tag{4.101}$$

by approximating the integrand in Eq. (4.100) to be constant. The first term in the right hand side of Eq. (4.100) or the term $v_{\rm out}^2$ in Eq. (4.65) represents the energy of the outflow, while the second term in the right hand side of Eq. (4.100) or the term $\alpha \xi_{\rm M} v_{\rm out}$ in Eq. (4.101) represents the energy dissipation by the shear viscosity on the current sheet. As is the case in Sec. 4.5.1.1, the former contribution can be assumed to be negligible. This assumption is justified later by confirming

$$\alpha \xi_{\rm M} \gg v_{\rm out}. \tag{4.102}$$

With this assumption, we approximate Eq. (4.103) as

$$B^2 = (\rho + p)\alpha \xi_{\rm M} v_{\rm out}. \tag{4.103}$$

We replace Eq. (4.66) in Sec. 4.5.1.1 with Eq. (4.103). Then, we need to solve Eqs. (4.61), (4.62), (4.103), (4.67), (4.47), and (4.19). If we solve the set of equations step by step, the expressions we find in Sec. 4.5.1.1, namely Eqs. (4.70), (4.71), (4.72), (4.73), and (4.74), hold. We can justify the assumption, Eq. (4.102), by confirming

$$\frac{\alpha \xi_{\rm M}}{v_{\rm out}} = {\rm Pr}_{\rm M} r_{\rm diss} \gg 1. \tag{4.104}$$

By substituting the expression of the outflow into Eq. (4.103), we obtain

$$(\rho + p)^{\frac{1}{2}} \sigma^{\frac{1}{2}} \alpha^{\frac{1}{2}} B^{-1} \xi_{\rm M}^2 = \tau, \tag{4.105}$$

which leads to expressions of the energy ratio

$$\Gamma = {\rm Pr}_{\rm M}^{-1} {\rm Re}_{\rm M}^{-\frac{2}{5}} r_{\rm diss} (\xi_{\rm K})^{-1}. \tag{4.106}$$

We solve Eq. (4.105) with the helicity conservation constraint, Eq. (4.19), to obtain

$$B = B_{\rm ini}^{\frac{4}{5}} \xi_{\rm M,ini}^{\frac{2}{5}} (\rho + p)^{\frac{1}{10}} \sigma^{\frac{1}{10}} \alpha^{\frac{1}{10}} \tau^{-\frac{1}{5}}, \tag{4.107}$$

$$\xi_{\rm M} = B_{\rm ini}^{\frac{2}{5}} \xi_{\rm M,ini}^{\frac{1}{5}} (\rho + p)^{-\frac{1}{5}} \sigma^{-\frac{1}{5}} \alpha^{-\frac{1}{5}} \tau^{\frac{2}{5}}. \tag{4.108}$$

Again, we should be careful about the effect of the dissipation on the inflow. Let us consider the region away from the current sheet and suppose that the inflow velocity $v'_{\rm in}$ is determined by the drag force. In that region, the energy injection from the magnetic field should balance with the energy dissipation by the drag force [29]. By approximating the relevant terms in Navier–Stokes equation (3.3) as

$$\left|\frac{(\boldsymbol{\nabla}\times\boldsymbol{B})\times\boldsymbol{B}}{\rho+p}\right| \sim \frac{B^2}{(\rho+p)\xi_{\rm M}}, \quad |-\alpha\boldsymbol{v}| \sim \alpha v'_{\rm in} \tag{4.109}$$

and balancing these terms, we obtain an estimate of the inflow velocity

$$v'_{\rm in} = \frac{B^2}{(\rho+p)\alpha\xi_{\rm M}} = \mathrm{Re}_{\rm M}^{\frac{2}{5}} v_{\rm in} \gg v_{\rm in}, \tag{4.110}$$

which supports our assumption that the rate-determining process is magnetic reconnection on the current sheets.

4.5.1.4 Maximally helical and dragged fast reconnection regime

In this regime, magnetic field is maximally helical, drag force dominates over shear viscosity, and the Lundquist number is large. In addition to Eq. (4.59),

$$|\epsilon| = 1, \quad r_{\rm diss}(\delta_{\rm c}) \gg 1, \quad S \gg S_{\rm c} \tag{4.111}$$

are satisfied. The mechanism is basically the fast reconnection described in Sec. 4.5.1.2, but with drag force rather than shear viscosity.

The discussion in Sec. 4.5.1.2 is almost valid except for the estimate of energy budget. We have, macroscopically, Eq. (4.103), assuming Eq. (4.104). Then, we need to solve the set of equations, (4.88), (4.90), (4.103), (4.67), (4.47), and (4.19). As in Sec. 4.5.1.2, the expressions in Eqs. (4.70), (4.91), (4.92), (4.93), (4.94), and (4.95) hold. The only difference comes from Eq. (4.103), which becomes

$$S_{\rm c}^{\frac{1}{2}}(\rho+p)\alpha B^{-2}\xi_{\rm M}^2 = \tau, \tag{4.112}$$

by substituting the expression of the outflow, Eq. (4.91). The energy ratio Γ can be expressed in the same way as Eq. (4.106). We solve Eq. (4.112) with the helicity conservation, Eq. (4.19), and the solutions are

$$B = B_{\rm ini}^{\frac{2}{3}}\xi_{\rm ini}^{\frac{1}{3}} S_{\rm c}^{\frac{1}{12}}(\rho+p)^{\frac{1}{6}}\alpha^{\frac{1}{6}}\tau^{-\frac{1}{6}}, \tag{4.113}$$

$$\xi_{\rm M} = B_{\rm ini}^{\frac{2}{3}} \xi_{\rm ini}^{\frac{1}{3}} S_{\rm c}^{-\frac{1}{6}} (\rho + p)^{-\frac{1}{3}} \alpha^{-\frac{1}{3}} \tau^{\frac{1}{3}}. \tag{4.114}$$

As the final remark in this section, we can discuss how significant the effect of the drag force on the inflow is in exactly the same manner as in Sec. 4.5.1.3. The hierarchy between $v_{\rm in}$ and $v'_{\rm in}$, Eq. (4.110) implies that the rate-determining process is the reconnection process.

4.5.1.5 Non-helical and viscous Sweet–Parker regime

In this regime, magnetic field is non-helical, shear viscosity dominates over drag force, and the Lundquist number is relatively small. In addition to Eq. (4.59),

$$\epsilon = 0, \quad r_{\rm diss}(\xi_{\rm K}) \ll 1, \quad S \ll S_{\rm c} \tag{4.115}$$

are satisfied. The mechanism that governs the evolution of the system is the same as the one in Sec. 4.5.1.1, except for that the dynamics is constrained by the Hosking integral conservation (4.33), instead of the helicity conservation Eq. (4.19).

By solving Eqs. (4.61), (4.62), (4.66), (4.67), and (4.47), together with Eq. (4.19), we obtain

$$B = B_{\rm ini}^{\frac{12}{17}} \xi_{\rm M,ini}^{\frac{15}{17}} (\rho + p)^{\frac{5}{34}} \sigma^{\frac{15}{34}} \eta^{\frac{5}{34}} \tau^{-\frac{10}{17}}, \tag{4.116}$$

$$\xi_{\rm M} = B_{\rm ini}^{\frac{4}{17}} \xi_{\rm M,ini}^{\frac{5}{17}} (\rho + p)^{-\frac{2}{17}} \sigma^{-\frac{6}{17}} \eta^{-\frac{2}{17}} \tau^{\frac{8}{17}}. \tag{4.117}$$

Expressions in Eqs. (4.70), (4.71), (4.72), (4.73), (4.74), (4.75), (4.76), and (4.80) hold independently of the initial conditions, $B_{\rm ini}$ and $\xi_{\rm M,ini}$.

4.5.1.6 Non-helical and viscous fast reconnection regime

In this regime, magnetic field is non-helical, shear viscosity dominates over drag force, and the Lundquist number is large. In addition to Eq. (4.59),

$$\epsilon = 0, \quad r_{\rm diss}(\xi_{\rm K}) \ll 1, \quad S \gg S_{\rm c} \tag{4.118}$$

are satisfied. The only difference from Sec. 4.5.1.2 is that the constraint from the Hosking integral conservation (4.33), instead of the helicity conservation, Eq. (4.19).

By using the same equations as the ones in Sec. 4.5.1.2 except the helicity conservation, expressions in Eqs. (4.70), (4.91), (4.92), (4.93), (4.94), (4.95), (4.96), (4.76), and (4.80) are derived independently of the initial conditions, $B_{\rm ini}$ and $\xi_{\rm M,ini}$. In combination with the Hosking integral conservation, we obtain

$$B = B_{\rm ini}^{\frac{4}{9}} \xi_{\rm ini}^{\frac{5}{9}} S_{\rm c}^{\frac{5}{18}} (\rho+p)^{\frac{5}{18}} \sigma^{\frac{5}{18}} \eta^{\frac{5}{18}} \tau^{-\frac{5}{9}}, \tag{4.119}$$

$$\xi_{\rm M} = B_{\rm ini}^{\frac{4}{9}} \xi_{\rm ini}^{\frac{5}{9}} S_{\rm c}^{-\frac{2}{9}} (\rho+p)^{-\frac{2}{9}} \sigma^{-\frac{2}{9}} \eta^{-\frac{2}{9}} \tau^{\frac{4}{9}}. \tag{4.120}$$

4.5.1.7 Non-helical and dragged Sweet–Parker regime

In this regime, magnetic field is non-helical, drag force dominates over shear viscosity, and the Lundquist number is relatively small. In addition to Eq. (4.59),

$$\epsilon = 0, \quad r_{\rm diss}(\xi_{\rm K}) \gg 1, \quad S \ll S_{\rm c} \tag{4.121}$$

are satisfied. The only difference from Sec. 4.5.1.3 is that the constraint from the Hosking integral conservation (4.33), instead of the helicity conservation Eq. (4.19).

As in Sec. 4.5.1.3, expressions in Eqs. (4.70), (4.71), (4.72), (4.73), (4.74), (4.104), (4.105), (4.106), and (4.110) are derived independently of the initial conditions, $B_{\rm ini}$ and $\xi_{\rm M,ini}$. In combination with the Hosking integral conservation, we obtain

$$B = B_{\rm ini}^{\frac{8}{13}} \xi_{\rm M,ini}^{\frac{10}{13}} (\rho+p)^{\frac{5}{26}} \sigma^{\frac{5}{26}} \alpha^{\frac{5}{26}} \tau^{-\frac{5}{13}}, \tag{4.122}$$

$$\xi_{\rm M} = B_{\rm ini}^{\frac{4}{13}} \xi_{\rm M,ini}^{\frac{5}{13}} (\rho+p)^{-\frac{2}{13}} \sigma^{-\frac{2}{13}} \alpha^{-\frac{2}{13}} \tau^{\frac{4}{13}}. \tag{4.123}$$

4.5.1.8 Non-helical and dragged fast reconnection regime

In this regime, magnetic field is non-helical, drag force dominates over shear viscosity, and the Lundquist number is large. In addition to Eq. (4.59),

$$\epsilon = 0, \quad r_{\rm diss}(\delta_{\rm c}) \gg 1, \quad S \gg S_{\rm c} \tag{4.124}$$

are satisfied. The only difference from Sec. 4.5.1.4 is that the constraint from the Hosking integral conservation (4.33), instead of the helicity conservation, Eq. (4.19).

As in Sec. 4.5.1.4, expressions in Eqs. (4.70), (4.91), (4.92), (4.93), (4.94), (4.95), (4.104), (4.112), (4.106), and (4.110) are derived independently of the initial conditions, $B_{\rm ini}$ and $\xi_{\rm M,ini}$. In combination with the Hosking integral conservation, we obtain

$$B = B_{\rm ini}^{\frac{4}{9}}\xi_{\rm ini}^{\frac{5}{9}}S_{\rm c}^{\frac{5}{36}}(\rho+p)^{\frac{5}{18}}\alpha^{\frac{5}{18}}\tau^{-\frac{5}{18}}, \tag{4.125}$$

$$\xi_{\rm M} = B_{\rm ini}^{\frac{4}{9}}\xi_{\rm ini}^{\frac{5}{9}}S_{\rm c}^{-\frac{1}{9}}(\rho+p)^{-\frac{2}{9}}\alpha^{-\frac{2}{9}}\tau^{\frac{2}{9}}. \tag{4.126}$$

4.5.2 Magnetically dominated and linear regimes

In this branch of regimes, magnetic energy dominates over kinetic energy, but the magnetic Reynolds number is small, and magnetic reconnection is not taking place. Conditions

$$\Gamma \ll 1, \quad {\rm Re_M} \ll 1 \tag{4.127}$$

are satisfied. In these regimes, the magnetic field is dominant and excites fluid motion. However, dissipation of the velocity field inhibits a significant excitation that leads to a large kinetic Reynolds number. Then, the dynamics of the fluid motion is linear and proceeds in a quasi-stationary way [29,82]. Although the system is characterized by four parameters, B, $\xi_{\rm M}$, v, and $\xi_{\rm K}$, since the energy is injected into the velocity field by the magnetic field at the magnetic coherence length, we approximate

$$\xi_{\rm K} = \xi_{\rm M}. \tag{4.128}$$

We extend the analysis in the literature [29], by incorporating the conservation of the Hosking integral, to find three additional equations for each regime [44,45]. We have several regimes according to the helicity fraction ϵ and the ratio of dissipation terms $r_{\rm diss}$, for each of which we find formulas that describe the evolution of the system.

4.5.2.1 Maximally helical and viscous regime

In this regime, magnetic field is maximally helical, and shear viscosity dominates over drag force. In addition to Eq. (4.127),

$$|\epsilon| = 1, \quad r_{\text{diss}}(\xi_{\text{M}}) \ll 1 \tag{4.129}$$

are assumed to hold.

Stationarity implies the balance between terms in the Navier–Stokes equation (3.3) [29],

$$\frac{B^2}{(\rho + p)\xi_{\text{M}}} = \frac{\eta v}{\xi_{\text{K}}^2}, \tag{4.130}$$

just like the evaluation of v'_{in} in Eq. (4.109). As is justified later, we neglected the advection term by assuming a small kinetic Reynolds number

$$\text{Re}_{\text{K}} \ll 1. \tag{4.131}$$

This assumption implies that the characteristic time scale of the process in this regime is the eddy turnover time at the kinetic coherence length given in Eq. (4.37). This estimate is supported by a dedicated study [82]. Then, the condition on decay time scales, Eq. (4.3), implies [29]

$$\tau_{\text{eddy}} = \tau. \tag{4.132}$$

To summarize, we are going to solve Eqs. (4.128), (4.130), and (4.132) with the condition of helicity conservation (4.19). By using Eqs. (4.128) and (4.130), we obtain

$$\Gamma = \text{Re}_{\text{K}} = \text{Pr}_{\text{M}}^{-1}\text{Re}_{\text{M}}, \tag{4.133}$$

which guarantees the assumption of a small kinetic Reynolds number, Eq. (4.131). Equation (4.132) can be rewritten as

$$(\rho + p)\eta B^{-2} = \tau. \tag{4.134}$$

Together with the constraint by the helicity conservation, Eq. (4.18), we obtain

$$B = (\rho + p)^{\frac{1}{2}}\eta^{\frac{1}{2}}\tau^{-\frac{1}{2}}, \tag{4.135}$$

$$\xi_{\mathrm{M}} = B_{\mathrm{ini}}^2 \xi_{\mathrm{M,ini}} (\rho + p)^{-1} \eta^{-1} \tau \tag{4.136}$$

for the magnetic field and $v = \tau^{-1}\xi_{\mathrm{M}}$, $\xi_{\mathrm{K}} = \xi_{\mathrm{M}}$ for the velocity field. If we compare the terms in the left hand side of the induction equation, Eq. (3.2), they balance with the same magnitude $\sim (\rho + p)^{1/2}\eta^{1/2}\tau^{-3/2}$, implying that the magnetic field is not dissipated by the resistivity, although the magnetic Reynolds number is small [29]. It suggests that, even when Eq. (4.21) is violated, magnetic helicity is approximately conserved in this regime, where the magnetic field takes a configuration such that

$$|\nabla^2 \boldsymbol{B}| \ll \frac{B}{\xi_{\mathrm{M}}^2}. \tag{4.137}$$

4.5.2.2 Maximally helical and dragged regime

In this regime, magnetic field is maximally helical, and drag force dominates over shear viscosity. In addition to Eq. (4.127),

$$|\epsilon| = 1, \quad r_{\mathrm{diss}}(\xi_{\mathrm{M}}) \gg 1 \tag{4.138}$$

are satisfied.

The discussion in Sec. 4.5.2.1 holds except the estimate of energy dissipation in Eq. (4.130). Stationarity implies the balance between terms in the Navier–Stokes equation (3.3) [29],

$$\frac{B^2}{(\rho + p)\xi_{\mathrm{M}}} = \alpha v, \tag{4.139}$$

as we did in the evaluation of v'_{in} in Eq. (4.109). We assume a small kinetic Reynolds number, and then the condition on decay time scales becomes Eq. (4.132). We are going to solve Eqs. (4.128), (4.139), and (4.132) with the condition of the helicity conservation (4.19). By using Eqs. (4.128), (4.139), we obtain

$$\Gamma = \mathrm{Re}_{\mathrm{K}} = \mathrm{Pr}_{\mathrm{M}}^{-1} r_{\mathrm{diss}}(\xi_{\mathrm{M}})^{-1} \mathrm{Re}_{\mathrm{M}} \tag{4.140}$$

which guarantees the assumption of a small kinetic Reynolds number, Eq. (4.131). Equation (4.132) can be rewritten as

$$(\rho + p)\alpha B^{-2} \xi_{\mathrm{M}}^2 = \tau \tag{4.141}$$

Together with the constraint by the helicity conservation, Eq. (4.18), we obtain

$$B = B_{\rm ini}^{\frac{2}{3}} \xi_{\rm M,ini}^{\frac{1}{3}} (\rho + p)^{\frac{1}{6}} \alpha^{\frac{1}{6}} \tau^{-\frac{1}{6}}, \tag{4.142}$$

$$\xi_{\rm M} = B_{\rm ini}^{\frac{2}{3}} \xi_{\rm M,ini}^{\frac{1}{3}} (\rho + p)^{-\frac{1}{3}} \alpha^{-\frac{1}{3}} \tau^{\frac{1}{3}} \tag{4.143}$$

for the magnetic field and $v = \tau^{-1}\xi_{\rm M}$, $\xi_{\rm K} = \xi_{\rm M}$ for the velocity field. Because of Eq. (4.132), again, the terms in the left hand side of the induction equation, Eq. (3.2), balance with the same magnitude. Therefore, the magnetic field is not dissipated by the resistivity, although the magnetic Reynolds number is small [29].

4.5.2.3 Non-helical and viscous regime

In this regime, magnetic field is non-helical, and shear viscosity dominates over drag force. In addition to Eq. (4.127),

$$\epsilon = 0, \quad r_{\rm diss}(\xi_{\rm M}) \ll 1 \tag{4.144}$$

are satisfied. The only difference from Sec. 4.5.2.1 is that the constraint from the Hosking integral conservation (4.33), instead of the helicity conservation Eq. (4.19).

Since the equations in Sec. 4.5.2.1 except the helicity conservation are the same as the ones in Sec. 4.5.2.1, we obtain Eqs. (4.133), (4.131), and (4.134). We solve Eq. (4.134) and the Hosking integral conservation to obtain

$$B = (\rho + p)^{\frac{1}{2}} \eta^{\frac{1}{2}} \tau^{-\frac{1}{2}}, \tag{4.145}$$

$$\xi_{\rm M} = B_{\rm ini}^{\frac{4}{5}} \xi_{\rm M,ini} (\rho + p)^{-\frac{2}{5}} \eta^{-\frac{2}{5}} \tau^{\frac{2}{5}} \tag{4.146}$$

for the magnetic field, and $v = \tau^{-1}\xi_{\rm M}$, $\xi_{\rm K} = \xi_{\rm M}$ for the velocity field. Note that the magnetic field is not dissipated by the resistivity, although magnetic Reynolds number is small [29].

4.5.2.4 Non-helical and dragged regime

In this regime, magnetic field is non-helical, and drag force dominates over shear viscosity. In addition to Eq. (4.127),

$$\epsilon = 0, \quad r_{\rm diss}(\xi_{\rm M}) \gg 1 \tag{4.147}$$

are satisfied. The only difference from Sec. 4.5.2.2 is that the constraint from the Hosking integral conservation (4.33), instead of the helicity conservation Eq. (4.19).

Since the equations are the same as those in Sec. 4.5.2.2 except the helicity conservation, we obtain Eqs. (4.140), (4.131), and (4.141). We solve Eq. (4.141) and the Hosking integral conservation to obtain

$$B = B_{\rm ini}^{\frac{4}{9}} \xi_{\rm M,ini}^{\frac{5}{9}} (\rho + p)^{\frac{5}{18}} \alpha^{\frac{5}{18}} \tau^{-\frac{5}{18}}, \tag{4.148}$$

$$\xi_{\rm M} = B_{\rm ini}^{\frac{4}{9}} \xi_{\rm M,ini}^{\frac{5}{9}} (\rho + p)^{-\frac{2}{9}} \alpha^{-\frac{2}{9}} \tau^{\frac{2}{9}} \tag{4.149}$$

for the magnetic field, and $v = \tau^{-1}\xi_{\rm M}$, $\xi_{\rm K} = \xi_{\rm M}$ for the velocity field. Note that the magnetic field is not dissipated by the resistivity, although the magnetic Reynolds number is small [29].

4.5.3 Kinetically dominated and maximally helical regime

In this regime, kinetic energy initially dominates over magnetic energy, and magnetic field is maximally helical. Conditions

$$\Gamma_{\rm ini} \gtrsim 1, \quad |\epsilon| = 1 \tag{4.150}$$

are satisfied. In kinetically dominated regimes, numerical studies [34, 88] have found that dynamo at small scales excites magnetic fields, and almost equipartition

$$\Gamma \sim 1, \quad \xi_{\rm M} \sim \xi_{\rm K} \tag{4.151}$$

is achieved quickly before entering into the scaling regime, even if $\Gamma_{\rm ini} \gg 1$. Hereafter, we suppose an approximate equipartition as the initial condition and classify the regimes according to the magnetic helicity fraction at this stage.

In the subsequent evolution, we have no reason to expect that Eq. (4.151) is maintained. Rather, we expect that the system enters into magnetically dominant regimes [37]. On one hand, we expect that the characteristic time scale is $\tau_{\rm eddy}$, provided that the velocity field governs the decay dynamics and that magnetic field energy is just fed by the small-scale dynamo. On the other hand, the magnetic field can play a crucial role because it involves conserved quantities. For the maximally helical magnetic field, magnetic helicity conservation (4.19) prohibits too fast decay of magnetic field. Contrary to the magnetic field, the velocity field should decay faster, if the Saffman cross helicity integral (4.45) constrains the decay. By dimensional analysis, the constraint becomes

$$B^2 v^2 \xi_{\mathrm{M}}^3 = \text{const.} \tag{4.152}$$

This constraint, the magnetic helicity conservation Eq. (4.19), and the decay time scale imply [43]

$$\Gamma \propto \tau^{-\frac{1}{2}}, \tag{4.153}$$

from which we understand that the system unavoidably enters the magnetically dominant regimes (solid arrows in Fig. 4.9). Therefore, for $\Gamma_{\mathrm{ini}} \sim 1$ with a slight dominance of kinetic energy, the system behaves as if it is initially magnetically dominant.

Let us comment on the use of the Saffman cross helicity integral. First, because of the absence of a magnetogenesis scenario in which generation of cross helicity is the distinctive property, we suppose that the cross helicity is zero on average. Then, the Saffman cross helicity integral is well-defined. However, the conservation of local cross helicity, which guarantees the conservation of the Saffman cross helicity integral, is only marginal. Nevertheless, it is slightly better conserved compared with the total energy because, in the Fourier space, we have

$$\frac{dh_{\mathrm{C}}(k)}{d\tau} = -(\eta k^2 + \alpha + \sigma k^2) h_{\mathrm{C}}(k), \tag{4.154}$$

$$\frac{d\rho_{\mathrm{tot}}(k)}{d\tau} = -2(\eta k^2 + \alpha + \sigma k^2) \rho_{\mathrm{tot}}(k), \tag{4.155}$$

where $h_{\mathrm{C}}(k)$ is the Fourier component of $\langle h_{\mathrm{C}}(\boldsymbol{x}) \rangle$ and $\rho_{\mathrm{tot}}(k) := d\rho_{\mathrm{M}}/d\log k + d\rho_{\mathrm{K}}/d\log k$. Finite dissipation terms imply exponential decay of both of the quantities, but the decay of the total energy is slightly faster. Based on this consideration, we expect the analysis based on the conservation of Saffman cross helicity integral can capture a qualitative behaviour of the system.

4.5.4 Kinetically dominated and non-helical regimes

In this branch of regimes, kinetic energy initially dominates over magnetic energy, and magnetic field is non-helical. Conditions

$$\Gamma_{\text{ini}} \gtrsim 1, \quad \epsilon = 0 \tag{4.156}$$

are satisfied. As is explained in Sec. 4.5.3, quasi-equipartition (4.151) is achieved quickly before entering into the scaling regime.

At this point, we have no reason to expect that Eq. (4.151) is stably maintained. We adopt the eddy turnover time as the decay time scale and use the Hosking integral conservation (4.33) and Saffman cross helicity integral conservation (4.152). Then we obtain

$$\Gamma \propto \tau^{\frac{12}{5}}, \tag{4.157}$$

which implies the entrance into kinetically dominant regimes. Then, it is reasonable to expect that the competition between small-scale dynamo and the above-explained negative feedback maintains the equipartition condition (4.151) [37] (dotted arrows in Fig. 4.9), where the decay dynamics is regarded as a pure hydrodynamics. In the subsequent scaling regimes, we assume Eqs. (4.151), (4.128), and the conservation of kinetic energy at large scales, Eq. (4.42).

In these regimes, Eq. (4.33) is not necessarily satisfied. However, it does not contradict the magnetic helicity conservation for two reasons. First, the magnetic field is enhanced at small scales, where helicity dissipation by the term $\sigma^{-1}\nabla^2\boldsymbol{B}$ is significant. Second, the large velocity field can violate the Gaussianity of magnetic fields through the non-linear term in the induction equation. Then, the estimate in Eq. (4.32) is not so reliable as in the magnetically dominated regimes. Based on these considerations, we ignore Eq. (4.33) in the following subsections.

4.5.4.1 Turbulent regime

In this regime, the kinetic Reynolds number is large and the decay mechanism is the kinetic energy cascade, which is explained in Sec. 4.3.2 [29]. In addition to

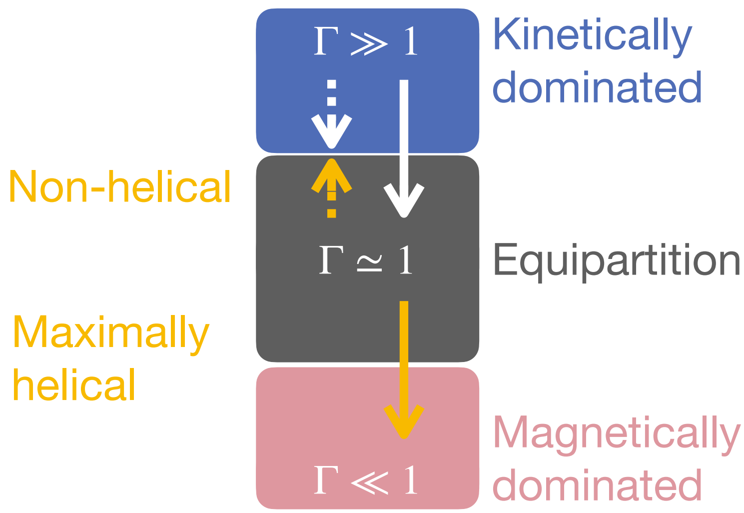

Figure 4.9: The fate of kinetically dominated initial conditions. The small-scale dynamo supports magnetic fields slightly subdominant to the kinetic field (white arrows). If the magnetic field is maximally helical at equipartition, the system enters a magnetically dominant regime (orange solid arrow). If the magnetic field is non-helical at equipartition, the equipartition condition is maintained in the subsequent evolution (orange-dotted arrow).

Eq. (4.156),

$$\mathrm{Re}_{\mathrm{K}} \gg 1 \tag{4.158}$$

is satisfied. We assume the quasi-equipartition conditions, Eqs. (4.151) and (4.128), in the scaling regime.

We solve the conservation of kinetic energy at large scales, Eq. (4.42), and the condition about the decay time, Eq. (4.132), to obtain [29]

$$v = v_{\mathrm{ini}}^{\frac{2}{n+5}} \xi_{\mathrm{K,ini}}^{\frac{2(n+3)}{n+5}} \tau^{-\frac{n+3}{n+5}}, \quad \xi_{\mathrm{K}} = v_{\mathrm{ini}}^{\frac{2}{n+5}} \xi_{\mathrm{K,ini}}^{\frac{2(n+3)}{n+5}} \tau^{\frac{2}{n+5}}, \tag{4.159}$$

or equivalently

$$B = B_{\mathrm{ini}}^{\frac{2}{n+5}} \xi_{\mathrm{M,ini}}^{\frac{2(n+3)}{n+5}} (\rho + p)^{\frac{n+3}{2n+10}} \tau^{-\frac{n+3}{n+5}}, \tag{4.160}$$

$$\xi_{\mathrm{M}} = B_{\mathrm{ini}}^{\frac{2}{n+5}} \xi_{\mathrm{M,ini}}^{\frac{2(n+3)}{n+5}} (\rho + p)^{-\frac{1}{n+5}} \tau^{\frac{2}{n+5}}, \tag{4.161}$$

in terms of magnetic field. These solutions imply the corresponding equation to Eq. (4.3) in this regime,

$$(\rho + p)^{\frac{1}{2}} B^{-1} \xi_{\mathrm{M}} = \tau. \tag{4.162}$$

This relation has been widely employed in the literature [29, 34, 49, 89].

4.5.4.2 Linear and viscous regime

In this regime, the kinetic Reynolds number is small and the decay is governed by the dissipation by shear viscosity at ξ_{K}. In addition to Eq. (4.156),

$$\mathrm{Re}_{\mathrm{K}} \ll 1, \quad r_{\mathrm{diss}}(\xi_{\mathrm{K}}) \ll 1 \tag{4.163}$$

are satisfied. We assume quasi-equipartition conditions, Eqs. (4.151) and (4.128), in the scaling regime.

We solve the energy conservation at large scales, Eq. (4.42), and the condition

$$\tau_{\eta}(\xi_{\mathrm{K}}) = \tau \tag{4.164}$$

for the decay time scale to obtain

$$v = v_{\mathrm{ini}} \xi_{\mathrm{K,ini}}^{\frac{n+3}{2}} \eta^{-\frac{n+3}{4}} \tau^{-\frac{n+3}{4}}, \quad \xi_{\mathrm{K}} = \tau^{\frac{1}{2}} \eta^{\frac{1}{2}}, \tag{4.165}$$

or equivalently

$$B = B_{\mathrm{ini}} \xi_{\mathrm{M,ini}}^{\frac{n+3}{2}} \eta^{-\frac{n+3}{4}} \tau^{-\frac{n+3}{4}}, \tag{4.166}$$

$$\xi_{\mathrm{M}} = \tau^{\frac{1}{2}} \eta^{\frac{1}{2}}, \tag{4.167}$$

in terms of magnetic field. These solutions imply

$$\eta^{-1} \xi_{\mathrm{M}}^2 = \tau, \tag{4.168}$$

which is the corresponding equation to Eq. (4.3) in this regime. Note that, since $\mathrm{Re}_{\mathrm{K}} = \tau_{\eta}(\xi_{\mathrm{K}})/\tau_{\mathrm{eddy}}$, Eqs. (4.132) and (4.164) coindides to give the same solutions in the linear and nonlinear regimes at the boundary, $\mathrm{Re}_{\mathrm{K}} = 1$.

4.5.4.3 Linear and dragged regime

In this regime, the kinetic Reynolds number is small and the decay is governed by the dissipation by drag force at ξ_{K}. In addition to Eq. (4.156),

$$\mathrm{Re}_{\mathrm{K}} \ll 1, \quad r_{\mathrm{diss}}(\xi_{\mathrm{K}}) \gg 1 \tag{4.169}$$

are satisfied.

We would impose $\tau_\alpha = \tau$, if a scaling solution exists in this regime. However, we cannot employ it to determine the scaling behaviour of the system because τ_α, which is defined in Eq. (4.50), is independent of v and ξ_{K}. Contrary to the other regimes in Sec. 4.5.4, the decay of the velocity field cannot slow down the decay process. Since we are assuming that the system is not frozen, we have $\tau_\alpha \ll \tau$. Then, the velocity field exponentially decays within a Hubble time, implying that the system quickly enters the magnetically dominated regimes.

4.6 Consistency among the analyses

In this section, we will combine all the results that we obtained in the last section, Sec. 4.5. Table 4.1 summarizes the results. We suppose that the system has never been frozen and employ Eq. (4.3), as is already stated in the beginning of this chapter. At this point, the analysis for each regime is still patchy. However, by confirming the consistency at the boundaries, we can draw a whole picture of how magnetic fields decay, without worrying about details of intermediate stages between different regimes and possible conflicts between analyses in different regimes.

Let us start from explaining two concerns that will be discussed in what follows. The concerns are originated from that the dichotomous criteria of regime classification explained in Sec. 4.4, as if it is universal for all the regimes, are not universal as conditions of B and ξ_{M}. For instance, a criterion we employed is whether the magnetic Reynolds number Re_{M} is large or not. However, Re_{M} as a function of B and ξ_{M} is not unique. It is the expression in Eq. (4.72) for the Sweet–Parker regimes, while it becomes the expression in Eq. (4.93) for the fast reconnection regimes. Therefore, a concern is that there can exist a configuration characterized by B and $\xi_{\rm M}$ such that it is out of both of the regimes according to the analyses in Sec. 4.5. The other concern is, on the contrary, a configuration such that the regime it belongs to cannot be uniquely determined. However, our regime-wise analyses are consistent and do not leave untouched parameter regions, which the two concerns suggest, in the B-$\xi_{\rm M}$ plain.

We check the consistency at every possible boundary between two regimes, apart from whether such a boundary appears in the early universe (See Fig. 5.2 for the application to the early universe).

The magnetically dominated, nonlinear, and viscous Sweet–Parker regimes are discussed in Secs. 4.5.1.1 and 4.5.1.5. Since Eq. (4.75) is common to these two regimes, we combine it with either of Eq. (4.19) or (4.33) to find the solutions, as we outlined in Sec. 4.1. When the conditions to be in these regimes are violated, the system belongs to other regimes and Eq. (4.75) no longer holds. In the following, we will find the boundary of these regimes.

One of the conditions for being in these regimes is the large magnetic Reynolds number $\mathrm{Re_M} \gg 1$. Equations (4.73) and (4.76) imply that the large magnetic Reynolds number guarantees the smallness of energy ratio Γ and the largeness of Lundquist number S. By using the expression in Eq. (4.72), the largeness of magnetic Reyonlds number is rephrased as

$$\xi_{\rm M} \gg \sigma^{-\frac{1}{2}}\tau^{\frac{1}{2}}, \quad \text{or equivalently,} \quad B \gg (\rho+p)^{\frac{1}{2}}\eta^{\frac{1}{2}}\tau^{-\frac{1}{2}}. \tag{4.170}$$

When these conditions are violated, magnetic reconnection no longer continues, and the system enters the magnetically dominated, linear, and viscous regimes discussed in Secs. 4.5.2.1 and 4.5.2.3.

Another condition is that the Lundquist number is not too large. By using the expression in Eq. (4.94), the condition is rephrased as

$$\xi_{\rm M} \ll S_{\rm c}^{\frac{1}{4}}\sigma^{-\frac{1}{2}}\tau^{\frac{1}{2}}, \quad \text{or equivalently,} \quad B \ll S_{\rm c}^{\frac{3}{4}}(\rho+p)^{\frac{1}{2}}\eta^{\frac{1}{2}}\tau^{-\frac{1}{2}}. \tag{4.171}$$

When these conditions are violated, the Sweet–Parker current sheets become unstable, and the system enters the magnetically dominated, non-linear, and viscous fast reconnection regimes discussed in Secs. 4.5.1.2 and 4.5.1.6.

Also, shear viscosity should be more significant than the drag term at the kinetic coherence length. By using the expression in Eq. (4.94), we rephrase it as

$$\xi_{\rm M} \gg \sigma^{-1}\eta^{-\frac{1}{2}}\alpha^{\frac{1}{2}}\tau, \quad \text{or equivalently,} \quad B \gg (\rho+p)^{\frac{1}{2}}\sigma^{-\frac{3}{2}}\eta^{-1}\alpha^{\frac{3}{2}}\tau. \tag{4.172}$$

When this condition is violated, the system is in the magnetically dominated, non-linear, and dragged Sweet–Parker regimes discussed in Secs. 4.5.1.3 and 4.5.1.7.

We should be careful also about that, when mean free paths of particles are longer than the typical length scales of the system, they contribute as rather the drag term than the shear viscosity [29]. This is because, as opposed to the shear viscosity, which is a macroscopic description of the collision between the constituent particles, the friction between the fluid and the free-streaming particles as the background appears as the drag term. Then, some portion of the contributions to η is switched off and becomes a contribution to α at around $l_{\rm mfp}$, where $l_{\rm mfp}$ is a mean free path of any species of constituent particles of the fluid. In the early universe, neutrinos and photons decouple from the plasma fluid and then contribute as the drag term, as will be explained in Sec. 5. Therefore, we have a possibility that

$$\xi_{\rm K} \gg l_{\rm mfp} \tag{4.173}$$

determines a boundary with the dragged Sweet–Parker regimes. Note that, by using Eqs. (4.74) and (4.72), this condition becomes

$$\xi_{\rm M} \ll \sigma^{-1}\tau l_{\rm mfp}^{-1} \tag{4.174}$$

in terms of the magnetic coherence length. When the magnetic coherence length is large and the magnetic field is strong, the aspect ratio of the current sheet becomes larger and, consequently, shortens the kinetic coherence length. When the condition, Eq. (4.172), is considered, this point should be taken into account as well.

Let us focus on the boundary between the viscous Sweet–Parker regimes and the linear and viscous regimes. The discussion for the former regimes suggests that the boundary is set when the condition, Eq. (4.170), is violated. In the latter regimes, on the other hand, we can find the location of the boundary, independently of the analyses in the former regimes. The expression of the magnetic Reynolds number in Secs. 4.5.2.1 and 4.5.2.3 is $\mathrm{Re}_\mathrm{M} = \sigma v \xi_\mathrm{M} = \sigma \tau^{-1} \xi_\mathrm{M}^2$, and the condition for this regime to be linear becomes

$$\xi_\mathrm{M} \ll \sigma^{-\frac{1}{2}} \tau^{\frac{1}{2}}, \quad \text{or equivalently,} \quad B \ll (\rho+p)^{\frac{1}{2}} \eta^{\frac{1}{2}} \tau^{-\frac{1}{2}}, \tag{4.175}$$

where we used Eq. (4.134). This is complementary to Eq. (4.170), and we can set the boundary at

$$\xi_\mathrm{M} = \sigma^{-\frac{1}{2}} \tau^{\frac{1}{2}}, \quad B = (\rho+p)^{\frac{1}{2}} \eta^{\frac{1}{2}} \tau^{-\frac{1}{2}} \tag{4.176}$$

consistently for both of the regimes.

In a parallel manner, we can find all the possible boundaries. The viscous Sweet–Parker regimes (Secs. 4.5.1.1 and 4.5.1.5) and the viscous fast reconnection regimes (Secs. 4.5.1.2 and 4.5.1.6) are connected at

$$\xi_\mathrm{M} = S_\mathrm{c}^{\frac{1}{4}} \sigma^{-\frac{1}{2}} \tau^{\frac{1}{2}}, \quad B = S_\mathrm{c}^{\frac{3}{4}} (\rho+p)^{\frac{1}{2}} \eta^{\frac{1}{2}} \tau^{-\frac{1}{2}}, \tag{4.177}$$

when the Lundquist number becomes the critical value, $S = S_\mathrm{c}$. The viscous Sweet–Parker regimes and the dragged Sweet–Parker regimes (Secs. 4.5.1.3 and 4.5.1.7) are connected at

$$\xi_\mathrm{M} = \sigma^{-1} \eta^{-\frac{1}{2}} \alpha^{\frac{1}{2}} \tau, \quad B = (\rho+p)^{\frac{1}{2}} \sigma^{-\frac{3}{2}} \eta^{-1} \alpha^{\frac{3}{2}} \tau \tag{4.178}$$

when the ratio of dissipation terms at the kinetic coherence length becomes unity, $r_\mathrm{diss}(\xi_\mathrm{K}) = 1$. The viscous fast reconnection regimes (Secs. 4.5.1.2 and 4.5.1.6) and the dragged fast reconnection regimes (Secs. 4.5.1.4 and 4.5.1.8) are not complementary from the construction, because we have a hierarchy of larger to smaller current sheets in these regimes. When $r_\mathrm{diss}(\delta_\mathrm{c}) \ll 1 \ll r_\mathrm{diss}(\xi_\mathrm{K})$, the largest structure feels the drag force, but the critical current sheets feel shear viscosity. Such an intermediate fast reconnection regime is not established, as far as we understand, and also not addressed in Sec. 4.5. However, conversely to the basic motivation we have in this section, we employ the consistency at the regime boundaries as the requirement that supports the reasonableness of analyses and conservatively choose $r_{\rm diss}(\xi_{\rm K}) = 1$, corresponding to a condition

$$\alpha\tau = S_{\rm c}^{\frac{1}{2}} {\rm Pr}_{\rm M}, \tag{4.179}$$

as the boundary because Eqs. (4.96) and (4.112) coincide when this condition holds. The dragged Sweet–Parker regimes (Secs. 4.5.1.3 and 4.5.1.7) and the dragged fast reconnection regimes (Secs. 4.5.1.4 and 4.5.1.8) are connected at

$$\xi_{\rm M} = S_{\rm c}^{\frac{1}{4}} \sigma^{-\frac{1}{2}} \tau^{\frac{1}{2}}, \quad B = S_{\rm c}^{\frac{1}{2}} (\rho + p)^{\frac{1}{2}} \sigma^{-\frac{1}{2}} \alpha^{\frac{1}{2}}, \tag{4.180}$$

when the Lundquist number takes the critical value. The magnetically dominated linear viscous regimes (Secs. 4.5.2.1 and 4.5.2.3) and the magnetically dominated linear dragged regimes (Secs. 4.5.2.2 and 4.5.2.4) are connected at

$$\xi_{\rm M} = \eta^{\frac{1}{2}} \alpha^{-\frac{1}{2}}, \quad B = (\rho + p)^{\frac{1}{2}} \eta^{\frac{1}{2}} \tau^{-\frac{1}{2}}, \tag{4.181}$$

when the dissipation terms become comparable at the kinetic coherence length becomes unity, $r_{\rm diss}(\xi_{\rm K}) = 1$. The magnetically dominated linear dragged regimes (Secs. 4.5.2.2 and 4.5.2.4) and the dragged Sweet–Parker regimes (Secs. 4.5.1.3 and 4.5.1.7) are connected at

$$\xi_{\rm M} = \sigma^{-\frac{1}{2}} \tau^{\frac{1}{2}}, \quad B = (\rho + p)^{\frac{1}{2}} \sigma^{-\frac{1}{2}} \alpha^{\frac{1}{2}}, \tag{4.182}$$

when the magnetic Reynolds number becomes unity.

See the red-shaded region in Fig. 4.10. We summarized the possible transitions between magnetically dominant regimes (gray solid arrows). Importantly, the network of the transitions is closed and no transition from a magnetically dominated regime to a kinetically dominated regime exists because small energy ratio, $\Gamma \ll 1$, is always satisfied in magnetically dominant regimes, even at their boundaries.

Let us discuss the cases where the kinetic energy is initially dominant. The non-helical and turbulent regime (Sec. 4.5.4.1) and the non-helical, linear, and viscous regime (Sec. 4.5.4.2) have scaling solutions. These regimes are consistent at their boundary

$$\xi_{\rm M} = \eta^{\frac{1}{2}} \tau^{\frac{1}{2}}, \quad B = (\rho + p)^{\frac{1}{2}} \eta^{\frac{1}{2}} \tau^{\frac{3}{2}}, \tag{4.183}$$

when the kinetic Reynolds number becomes unity. We have another important boundary for the kinetically dominated regimes at

$$\alpha\tau = 1. \tag{4.184}$$

When $\alpha\tau \gg 1$, the non-helical, linear, and viscous regime becomes the non-helical, linear, and dragged regime (Sec. 4.5.4.3) and quickly enters a magnetically dominant regime because $r_{\text{diss}} = \alpha\tau$. The non-helical and turbulent regime also becomes the non-helical, linear, and dragged regime and is quickly dominated by the magnetic energy because $\text{Re}_{\text{K}} = (\alpha\tau)^{-1}$. These transitions into the magnetically dominated regimes are represented by the blue-dashed arrows in Fig. 4.10.

Finally, suppose that the magnetic field is partially helical with a tiny helicity fraction, $0 < |\epsilon| \ll 1$. Then there exists a possibility that the non-helical evolution terminates at some point, when the inequality (4.17) is saturated. This is likely to happen, assuming a constant enthalpy density $\rho + p$ and the reasonable slope of the velocity IR spectrum $n > -2$, because $B^2\xi_{\text{M}}$ decreases as the magnetic field decays. After that, the magnetic field becomes maximally helical and enters the maximally helical regime (Sec. 4.5.3). Then, the system quickly becomes magnetically dominant (blue-dotted arrows in Fig. 4.10).

4.7 Applicability

Now we are almost ready to apply the analysis in the early universe, which is the topic in Chap. 5. Before that, however, let us figure out the range of applicability. Regimes out of the applicability range are beyond the scope of this thesis.

First, we assumed a large electric conductivity. We have two conditions on this point. One is that a large magnetic Prandtl number is necessary to justify the approximations we have made in Sec. 4.5. This condition is always satisfied in the early universe before the recombination. Because of the large magnetic Prandtl number in the early universe, we have safely approximated in the reconnection regimes that a large fraction of the injected magnetic energy is almost dissipated in the current

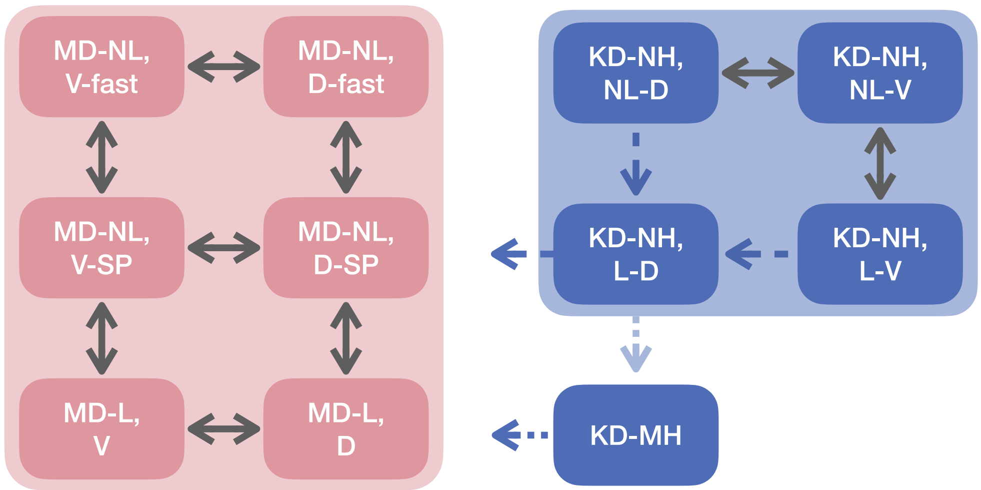

Figure 4.10: Summary of Sec. 4.6. As for the possible transitions between different regimes, our regime-wise analyses are consistent at the boundaries of the regimes (gray solid arrows). When $\alpha\tau \gg 1$, one-way transitions from kinetically dominated regimes to a magnetically dominated regime is expected (blue-dashed arrows). When magnetic field becomes maximally helical in a kinetically dominated regime, one-way transitions to a magnetically dominated regime are expected (blue-dotted arrows).

sheet. The other is that, to treat magnetic helicity as a conserved quantity and employ Eqs. (4.19) and (4.33), the condition in Eq. (4.21) is necessary unless Eq. (4.137) holds. If this condition is violated, we do not have any trustable conserved quantity in magneto-hydrodynamics. To be conservative, a possible option may be employing the magnetic energy at large scales as a conserved quantity [29], since we do not have any reasons to expect the inverse transfer without helicity conservation.

Second, the fluid approximation we made is violated if the length scales involved in the analysis are too small. The smallest length scales that appeared in our analysis are δ_c for the fast reconnection regimes and ξ_K for the other regimes. Before the recombination epoch, these length scales are to be compared with the mean free paths of electrons and positrons. If the mean free paths are longer, the fluid approximation completely breaks down, and the system is no longer within the framework of magneto-hydrodynamics. After the recombination epoch, these length scales are to be compared with the ion inertial length. If protons decouple from the fluid of electrons and violate the single-fluid approximation, then the system becomes the so-called kinetic or collisionless regime [69]. The reconnection time scale in the collisionless regime is empirically known to be $\tau_{\text{collisionless}} \sim 10\rho^{\frac{1}{2}}B^{-1}\xi_{\text{M}}$ [43, 69]. In Ref. [43], they considered such a regime and concluded that this reconnection is faster than the photon drag on the inflow discussed around Eq. (4.110), implying that the photon drag determines the time scale of the decay in this regime.

Finally, our analysis could be updated, with the strategy kept the same. While we are conservative in this thesis, a trial of discussing the effect of strong magnetic fields on the tranport coefficients [90] and taking the collisionless regime into account can be found in the literature [43]. Also, apart from the Sweet–Parker model, theoretical understandings of magnetic reconnection are not well-established [80]. Numerical or experimental studies will provide us with both support of the existing understanding and hints for deeper theoretical understandings, and magnetic reconnection models that are not established may turn out to play a crucial role in the evolution of primordial magnetic fields. If some regimes that are not considered in Chap. 4 turn out to be important, they could be incorporated into the analysis.

Chapter 5

Implications on primordial magnetic fields

In this chapter, we combine the pieces of description in Chap. 4 and apply them to discuss primordial magnetic fields based on our work [44, 45]. We first integrate the regime-wise analyses and give a comprehensive overview of how the evolution of primordial magnetic fields is described, by taking into account the dissipation coefficient in the early universe (See Appendix A for their values). Then, we demonstrate a few examples of how primordial magnetic fields evolve for specific initial conditions. We also demonstrate the usefulness of our study. Namely, we propose an inflationary magnetogenesis scenario with the new description of subsequent evolution, based on our work [28].

5.1 Integration of the analyses

In this section, we draw lines in the $\xi_{\rm M}$-B plain that are determined by the condition of decay time scales, Eq. (4.4). At this point, we finally take into account the frozen regime, which makes the difference between Eqs. (4.3) and (4.4). We explain representative snapshots at some radiation temperatures of the universe. Based on that, we explain how one can make use of our analysis to understand the time evolution of primordial magnetic fields.

See Fig. 5.1. Thin gray solid lines are the lines of decay time scales, determined by Eq. (4.4), at every temperature discretized by a 0.1 order of magnitude, $\Delta \log_{10}(T/\mathrm{GeV}) = 0.1$, below the electroweak scale. We take the initial time to be at the electroweak scale, $T(\tau_{\rm ini}) = 100\,\mathrm{GeV}$. The heavy orange solid lines are for

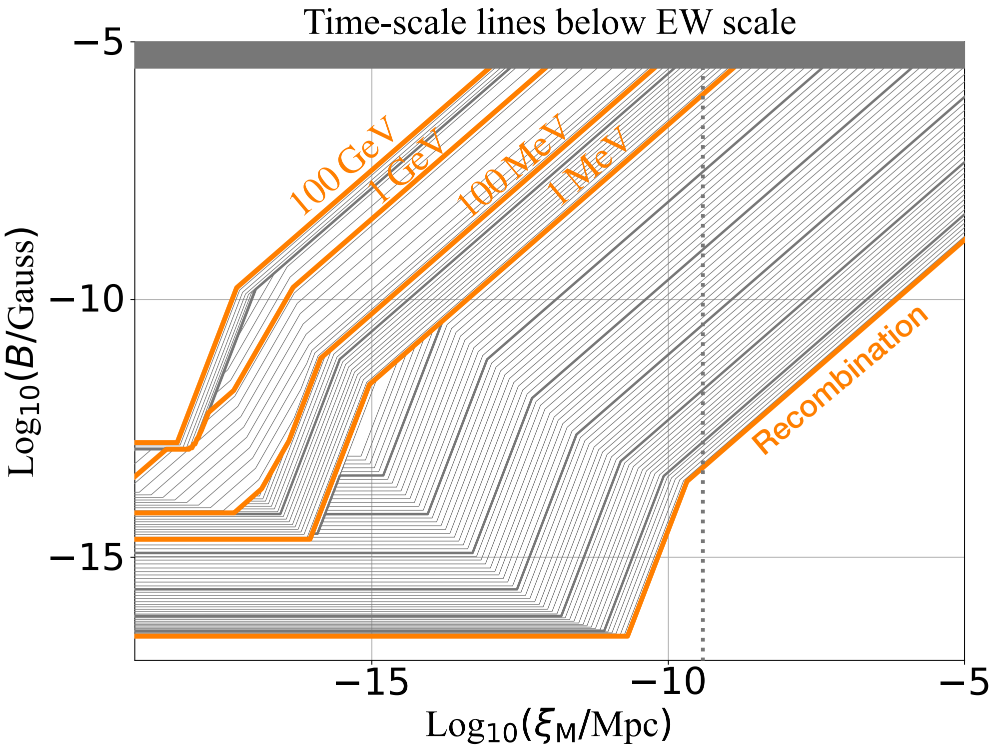

Figure 5.1: Time-scale lines (thin gray solid lines), on which Eq. (4.4) is satisfied, with taking the initial time to be at the electroweak scale, $T(\tau_{\rm ini}) = 100\,\mathrm{GeV}$. Thick gray solid lines are drawn for temperatures at every order of magnitude. Heavy orange solid lines are for $T = 100\,\mathrm{GeV}$, $1\,\mathrm{GeV}$, $100\,\mathrm{MeV}$, $1\,\mathrm{MeV}$, and $0.1\,\mathrm{eV}$ (recombination), as labeled in the plot. The gray-shaded region is excluded by the critical energy density of the universe. The gray-dotted line is the Hubble horizon at the electroweak scale. B and $\xi_{\rm M}$ are described in the comoving unit.

some specific choices of temperatures, $T = 100\,\mathrm{GeV}$, $1\,\mathrm{GeV}$, $100\,\mathrm{MeV}$, $1\,\mathrm{MeV}$, and $0.1\,\mathrm{eV}$, respectively from the top one down to the bottom one. Although this figure is complicated, it is useful as a tool to find the rough evolution history of primordial magnetic fields for an arbitrary initial condition, as explained in the following.

Suppose that magnetic fields are generated at the electroweak scale. If the initial condition $(\xi_{\rm M,ini}, B_{\rm ini})$ is below the line labeled as $100\,\mathrm{GeV}$, it implies that the magnetic field is frozen because any magneto-hydrodynamic processes are slower than the Hubble expansion. On the other hand, if the initial condition is above the line, relevant magneto-hydrodynamic processes are fast enough to decrease magnetic field down onto the line within a Hubble time. Hereafter, we assume that the initial condition is exactly on the line. If the coherence length is smaller than the boundary given by Eq. (4.176), then the viscosity dissipation of the subdominant velocity field is the rate-determining process. Longer coherence lengths are subject to the magnetic reconnection processes. The boundary, Eq. (4.177), separates the Sweet–Parker and the fast reconnection regimes. Drag force is absent in this epoch because any particles have small mean free paths, and therefore the shear viscosity is the dominant dissipation term. The relationship between $B_{\rm ini}$ and $\xi_{\rm M,ini}$ is

$$B_{\rm ini} = \begin{cases} 4\times 10^{-8}\,{\rm G}\left(\dfrac{\xi_{\rm M,ini}}{10^{-16}\,{\rm Mpc}}\right), & \xi_{\rm M,ini} > 5\times 10^{-18}\,{\rm Mpc} \\ 2\times 10^{-7}\,{\rm G}\left(\dfrac{\xi_{\rm M,ini}}{10^{-16}\,{\rm Mpc}}\right)^3, & 5\times 10^{-19}\,{\rm Mpc} < \xi_{\rm M,ini} < 5\times 10^{-18}\,{\rm Mpc} \\ 2\times 10^{-13}\,{\rm G}, & \xi_{\rm M,ini} < 5\times 10^{-19}\,{\rm Mpc}, \end{cases} \tag{5.1}$$

where the first line is for the viscous fast reconnection regime, the second line is for the viscous Sweet–Parker reconnection regime, and the third line is for the magnetically dominated viscous linear regime.

The magnetic field decays as the line moves downward. Below the electroweak scale, the mean free path of neutrinos begins to grow, and they act on the plasma as a drag force at around GeV scale. According to Eq. (4.3), B and $\xi_{\rm M}$ are related as

$$B = \begin{cases} 3\times 10^{-10}\,{\rm G}\left(\dfrac{\xi_{\rm M}}{10^{-16}\,{\rm Mpc}}\right), & \xi_{\rm M} > 5\times 10^{-17}\,{\rm Mpc} \\ 6\times 10^{-10}\,{\rm G}\left(\dfrac{\xi_{\rm M}}{10^{-16}\,{\rm Mpc}}\right)^2, & 5\times 10^{-18}\,{\rm Mpc} < \xi_{\rm M} < 5\times 10^{-17}\,{\rm Mpc} \\ 3\times 10^{-11}\,{\rm G}\left(\dfrac{\xi_{\rm M}}{10^{-16}\,{\rm Mpc}}\right), & 7\times 10^{-20}\,{\rm Mpc} < \xi_{\rm M} < 5\times 10^{-18}\,{\rm Mpc}, \\ 2\times 10^{-14}\,{\rm G}, & \xi_{\rm M} < 7\times 10^{-20}\,{\rm Mpc} \end{cases} \tag{5.2}$$

at GeV scale. The first line is for the neutrino-drag fast reconnection regime, the second line is for the neutrino-drag Sweet–Parker reconnection regime, the third line is for the magnetically dominated neutrino-drag linear regime, and the final line is for the magnetically dominated viscous linear regime. However, we see a small dip of the time-scale line at $10^{-18.3}\,\mathrm{Mpc} < \xi_{\mathrm{M}} < 10^{-17.8}\,\mathrm{Mpc}$, which is not accounted for by Eq. (5.2). This feature originates from the fact that the strength of the magnetic field determined by Eq. (4.134) does not decrease monotonically. This is because the contribution from neutrinos to the viscosity coefficient increases below the electroweak temperature. This contribution $\sim G_{\mathrm{F}} T^{-4}$, where G_{F} is the Fermi constant, becomes dominant after $\sim 40\,\mathrm{GeV}$ until neutrinos decouple from the fluid, the right hand side of Eq. (4.134) increases as $\sim T^{-3}$. Therefore, the line of Eq. (4.3) moves downward first and upward later. The line sweeps the magnetic field downward first, but it leaves the magnetic field frozen when it goes upward. Equation (4.4) takes this frozen regime into account, and the dip feature is nothing but the difference between the two conditions in Eqs. (4.3) and (4.4).

At the QCD scale $\sim 100\,\mathrm{MeV}$, we have five regimes. B and ξ_{M} are related as

$$B = \begin{cases} 2\times 10^{-11}\,\mathrm{G}\left(\dfrac{\xi_{\mathrm{M}}}{10^{-16}\,\mathrm{Mpc}}\right), & \xi_{\mathrm{M}} > 1\times 10^{-16}\,\mathrm{Mpc} \\ 2\times 10^{-11}\,\mathrm{G}\left(\dfrac{\xi_{\mathrm{M}}}{10^{-16}\,\mathrm{Mpc}}\right)^{3}, & 1\times 10^{-17}\,\mathrm{Mpc} < \xi_{\mathrm{M}} < 1\times 10^{-16}\,\mathrm{Mpc} \\ 2\times 10^{-12}\,\mathrm{G}\left(\dfrac{\xi_{\mathrm{M}}}{10^{-16}\,\mathrm{Mpc}}\right)^{2}, & 1.0\times 10^{-17}\,\mathrm{Mpc} < \xi_{\mathrm{M}} < 1.3\times 10^{-17}\,\mathrm{Mpc}, \\ 2\times 10^{-13}\,\mathrm{G}\left(\dfrac{\xi_{\mathrm{M}}}{10^{-16}\,\mathrm{Mpc}}\right), & 8\times 10^{-18}\,\mathrm{Mpc} < \xi_{\mathrm{M}} < 1\times 10^{-17}\,\mathrm{Mpc}, \\ 2\times 10^{-14}\,\mathrm{G}, & \xi_{\mathrm{M}} < 8\times 10^{-18}\,\mathrm{Mpc}, \end{cases} \tag{5.3}$$

where the first line is for the viscous fast reconnection regime, the second line is for the viscous Sweet–Parker reconnection regime, the third line is for the neutrino-drag Sweet–Parker reconnection regime, the fourth line is for the magnetically dominated neutrino-drag linear regime, and the final line is for the magnetically dominated viscous linear regime.

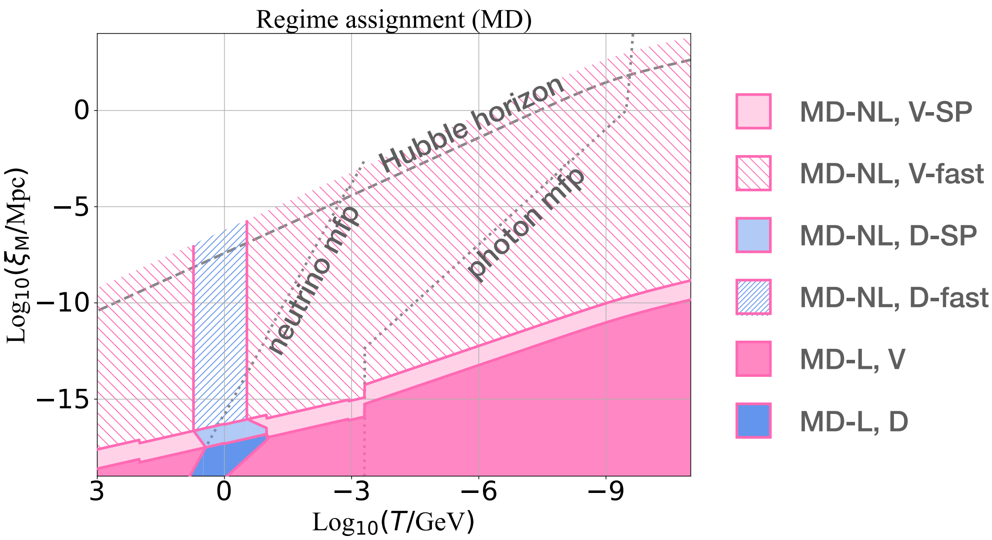

Figure 5.2: Regime assignment of magnetic fields that satisfy the condition Eq. (4.3). Pink solid lines are the boundaries of different regimes. At every temperature, the decay process is the magnetically dominated viscous linear one in the pink-shaded region, the viscous Sweet–Parker reconnection in the pale pink-shaded region, the viscous fast reconnection in the pink-hatched region, the magnetically dominated dragged linear one in the blue-shaded region, the dragged Sweet–Parker reconnection in the pale blue-shaded region, and the viscous fast reconnection in the blue-hatched region. The gray dashed line is the Hubble horizon, and the gray-dotted lines are mean free paths of neutrinos and photons.

Just before the BBN at $\sim 1\,\mathrm{MeV}$, B and ξ_M are related as

$$B = \begin{cases} 4\times 10^{-13}\,\mathrm{G}\left(\dfrac{\xi_\mathrm{M}}{10^{-16}\,\mathrm{Mpc}}\right), & \xi_\mathrm{M} > 9\times 10^{-16}\,\mathrm{Mpc} \\[2ex] 6\times 10^{-15}\,\mathrm{G}\left(\dfrac{\xi_\mathrm{M}}{10^{-16}\,\mathrm{Mpc}}\right)^3, & 9\times 10^{-17}\,\mathrm{Mpc} < \xi_\mathrm{M} < 9\times 10^{-16}\,\mathrm{Mpc} \\[2ex] 3\times 10^{-15}\,\mathrm{G}, & \xi_\mathrm{M} < 9\times 10^{-17}\,\mathrm{Mpc}, \end{cases} \tag{5.4}$$

where the first line is for the viscous fast reconnection regime, the second line is for the viscous Sweet–Parker reconnection regime, and the third line is for the magnetically dominated viscous linear regime. At $\sim 0.5\,\mathrm{MeV}$, electrons become massive and the mean free path of photons grows. However, $r_{\rm diss}$ is always smaller than unity below this scale, although photons decouple from the fluid and contribute as the drag term.

At the recombination epoch $\sim 0.1\,\mathrm{eV}$, B and $\xi_{\rm M}$ are related as

$$B = \begin{cases} 1 \times 10^{-14}\,\mathrm{G}\left(\dfrac{\xi_{\rm M}}{10^{-10}\,\mathrm{Mpc}}\right), & \xi_{\rm M} > 9 \times 10^{-16}\,\mathrm{Mpc} \\ 3 \times 10^{-15}\,\mathrm{G}\left(\dfrac{\xi_{\rm M}}{10^{-10}\,\mathrm{Mpc}}\right)^3, & 2 \times 10^{-10}\,\mathrm{Mpc} < \xi_{\rm M} < 2 \times 10^{-11}\,\mathrm{Mpc} \\ 3 \times 10^{-17}\,\mathrm{G}, & \xi_{\rm M} < 2 \times 10^{-11}\,\mathrm{Mpc}, \end{cases} \tag{5.5}$$

where the first line is for the viscous fast reconnection regime, the second line is for the viscous Sweet–Parker reconnection regime, and the third line is for the magnetically dominated viscous linear regime. When the recombination completes, the viscosity coefficient increases because of the neutral hydrogen, and the line of decay time scales goes upward. After that, the magnetic field freezes on the line at the recombination.

As is indicated from the above snapshots, which regimes exist depends on the temperatures, which determines not only the time scale τ but also the values of dissipation coefficients. We plot which regime the system belongs to, assuming that the system is processed with Eq. (4.3), in Fig. 5.2.

In most of the temperature ranges, magnetic fields with shorter coherence length than $\sigma^{-\frac{1}{2}}\tau^{\frac{1}{2}}$ (Eq. (4.176)) are in the magnetically dominated viscous linear regime, magnetic fields with longer coherence length than $S_{\rm c}^{\frac{1}{4}}\sigma^{-\frac{1}{2}}\tau^{\frac{1}{2}}$ (Eq. (4.177)) are in the viscous fast reconnection regime, and the intermediate regime is the viscous Sweet–Parker regime. At temperatures below $\sim$ GeV, neutrino mean free paths become longer than $\min(\xi_{\rm M}, \xi_{\rm K})$, and their contribution to the shear viscosity vanishes. Similarly, at temperatures below $\sim$ MeV, photon mean free paths become longer than $\min\{\xi_{\rm M}, \xi_{\rm K}\}$, and their contribution to the shear viscosity vanishes.

Only around the GeV scales, dragged regimes appear. Magnetic fields with shorter coherence length than $\sigma^{-\frac{1}{2}}\tau^{\frac{1}{2}}$ (Eq. (4.182)) are in the magnetically dominated dragged linear regime, magnetic fields with longer coherence length than $S_{\rm c}^{\frac{1}{4}}\sigma^{-\frac{1}{2}}\tau^{\frac{1}{2}}$ (Eq. (4.180)) are in the dragged fast reconnection regime, and the intermediate regime is the dragged Sweet–Parker regime. The range of temperatures with these regimes is limited because neutrino mean free paths are so short that their contribution as the drag term vanishes for higher temperatures, and because the amplitude of their drag term becomes smaller and negligible for lower temperatures.

5.2 Description of the magnetic field evolution in the early universe

In this section, we provide explicit examples of magnetic field evolution in the early universe based on the discussion in the last section, and discuss how we can employ our analysis for an arbitrary initial condition. Figure 5.4 is the summary plot of this thesis.

5.2.1 Case study

We take four initial conditions, (A–D), given in Table 5.1. We first consider primordial magnetic fields generated above the electroweak scale. Then, at the electroweak symmetry breaking, the magnetic fields should satisfy the condition, Eq. (2.7), to avoid the baryon isocurvature problem (blue-dotted line in Fig. 5.4 represents the upper limit). On the other hand, the magneto-hydrodynamic processes make the magnetic fields on or below the line determined by the condition, Eq. (4.4), evaluated at the electroweak scale (the leftmost blue solid line in Fig. 5.4 represents the upper limit). We choose the initial strength and coherence length

$$B_{\rm ini}^{\rm (A/B)} = 8 \times 10^{-10}\,{\rm G}, \quad \xi_{\rm M,ini}^{\rm (A/B)} = 3 \times 10^{-17}\,{\rm Mpc} \tag{5.6}$$

for $T_{\rm ini}^{\rm (A/B)} = 100\,{\rm GeV}$, so that they are as strong as possible below the upper limits. As the extreme choices, we consider (A) non-helical and (B) maximally helical magnetic fields. The other initial conditions are based on an idea that magnetogenesis scenarios in the broken phase of the electroweak symmetry are free from the baryon isocurvature problem [28]. We introduced the Chern-Simons coupling between the inflaton and the gauge field, through which the inflaton velocity amplifies helical magnetic fields. See Appendix D for more explanation about the model. For

	$T_{\rm ini}$	$B_{\rm ini}$	$\xi_{\rm M,ini}$	$\epsilon_{\rm ini}$	$B_{\rm rec}$	$\xi_{\rm M,rec}$
(A)	$100\,\mathrm{GeV}$	$8\times10^{-10}\,\mathrm{G}$	$3\times10^{-17}\,\mathrm{Mpc}$	0	$3\times10^{-17}\,\mathrm{G}$	$3\times10^{-11}\,\mathrm{Mpc}$
(B)	$100\,\mathrm{GeV}$	$8\times10^{-10}\,\mathrm{G}$	$3\times10^{-17}\,\mathrm{Mpc}$	1	$1\times10^{-13}\,\mathrm{G}$	$1\times10^{-9}\,\mathrm{Mpc}$
(C)	$100\,\mathrm{GeV}$	$7\times10^{-7}\,\mathrm{G}$	$3\times10^{-14}\,\mathrm{Mpc}$	3×10^{-6}	$2\times10^{-12}\,\mathrm{G}$	$1\times10^{-8}\,\mathrm{Mpc}$
(D)	$1\,\mathrm{MeV}$	$7\times10^{-7}\,\mathrm{G}$	$1\times10^{-11}\,\mathrm{Mpc}$	1	$8\times10^{-10}\,\mathrm{G}$	$6\times10^{-6}\,\mathrm{Mpc}$

Table 5.1: Four choices of initial conditions and the resultant magnetic fields at the recombination epoch. (A) Magnetic fields generated before or at the electroweak scale. The strength is taken as strong as possible for the baryon isocurvature problem not to arise. Non-helical magnetic field is assumed as an extreme choice. (B) the same as (A) except that the magnetic field is maximally helical. (C) A low-scale inflationary magnetogenesis scenario at the electroweak scale. (D) Another low-scale inflationary magnetogenesis scenario at just above the big-bang nucleosynthesis.

a choice of parameters, the model has a potential to generate a magnetic field with

$$B_{\rm ini}^{\rm (C)} = 7\times10^{-7}\,\mathrm{G}, \quad \xi_{\rm M,ini}^{\rm (C)} = 3\times10^{-14}\,\mathrm{Mpc}, \quad \epsilon_{\rm ini}^{\rm (C)} = 3\times10^{-6} \tag{5.7}$$

at $T_{\rm ini}^{\rm (C)} = 100\,\mathrm{GeV}$, by taking the magnetogenesis temperature as high as possible, avoiding the baryon isocurvature problem. The helicity fraction becomes unexpectedly small because rather the parametric resonance just after the inflation, which produces non-helical magnetic fields, than the tachyonic amplification of helical fields during inflation was observed to be dominant [28]. We modify the inflaton potential to make the tachyonic amplification dominant, and then the model has a potential to generate a magnetic field with

$$B_{\rm ini}^{\rm (D)} = 7\times10^{-7}\,\mathrm{G}, \quad \xi_{\rm M,ini}^{\rm (D)} = 1\times10^{-11}\,\mathrm{Mpc}, \quad \epsilon_{\rm ini}^{\rm (D)} = 1 \tag{5.8}$$

at $T_{\rm ini}^{\rm (D)} = 1\,\mathrm{MeV}$, by taking the magnetogenesis temperature as low as possible [28].

See Fig. 5.3. For each initial condition, we solved the conservation laws, Eqs. (4.19) and (4.33), and the B-$\xi_{\rm M}$ relation determined by the lines of time scales in Fig. 5.1. The left panel describes the evolution of magnetic field strength, and the right panel is for the evolution of magnetic coherence length. By comparing the right panel with Fig. 5.2, we can read off what mechanism is operating at each temperature. Magnetic fields for the initial conditions (A–C) are almost frozen before the neutrino-drag fast reconnection is involved at around GeV scale. The decay of magnetic field strength is milder for the maximally helical field (B) compared with the non-helical fields (A, C). For (B, C) after that, and for (D), the viscous fast reconnection regime is the only relevant decay process. The flat regions in the plots imply that magnetic fields sometimes freeze before the reconnection rate becomes fast enough again. The bending of the plots for (C) at around 100 eV reflects the transition from the non-helical to the maximally helical regime. The magnetic field (C) initially has only a tiny magnetic helicity fraction, but the magnetic field decays so much, while magnetic helicity is conserved, that it becomes maximally helical. For (A), the magnetic field enters the Sweet–Parker regime at MeV scale when electrons become massive and the electric conductivity drops. The resultant magnetic fields at the recombination epoch are estimated as

$$B_{\rm rec}^{(\rm A)} = 3\times 10^{-17}\,{\rm G}, \quad \xi_{\rm M,rec}^{(\rm A)} = 3\times 10^{-11}\,{\rm Mpc}, \tag{5.9}$$

$$B_{\rm rec}^{(\rm B)} = 1\times 10^{-13}\,{\rm G}, \quad \xi_{\rm M,rec}^{(\rm B)} = 1\times 10^{-9}\,{\rm Mpc}, \tag{5.10}$$

$$B_{\rm rec}^{(\rm C)} = 2\times 10^{-12}\,{\rm G}, \quad \xi_{\rm M,rec}^{(\rm C)} = 1\times 10^{-8}\,{\rm Mpc}, \tag{5.11}$$

$$B_{\rm rec}^{(\rm D)} = 8\times 10^{-10}\,{\rm G}, \quad \xi_{\rm M,rec}^{(\rm D)} = 6\times 10^{-6}\,{\rm Mpc}. \tag{5.12}$$

An important consequence is that, the resultant magnetic fields for (A,B) do not explain the observed strength of the intergalactic magnetic fields in void regions. This fact implies that any magnetogenesis scenario above the electroweak scale is not a viable option. On the other hand, magnetogenesis scenarios at or below the electroweak scale is promising in the sense that they are both safe from the baryon isocurvature constraint and able to account for the origin of the intergalactic magnetic field. We plot the evolution paths of these initial conditions, (A–D), in the $\xi_{\rm M}$-B plain in Fig. 5.4. A remark is that, for strong magnetic fields, the estimate of the viscosity coefficient could be modified, and also the kinetic reconnection regime could be taken into account because the width of reconnection current sheets become comparable to typical scales of particle collision. We show a possibility of these modifications proposed in Ref. [43] with a faint blue solid line in the figure. If we

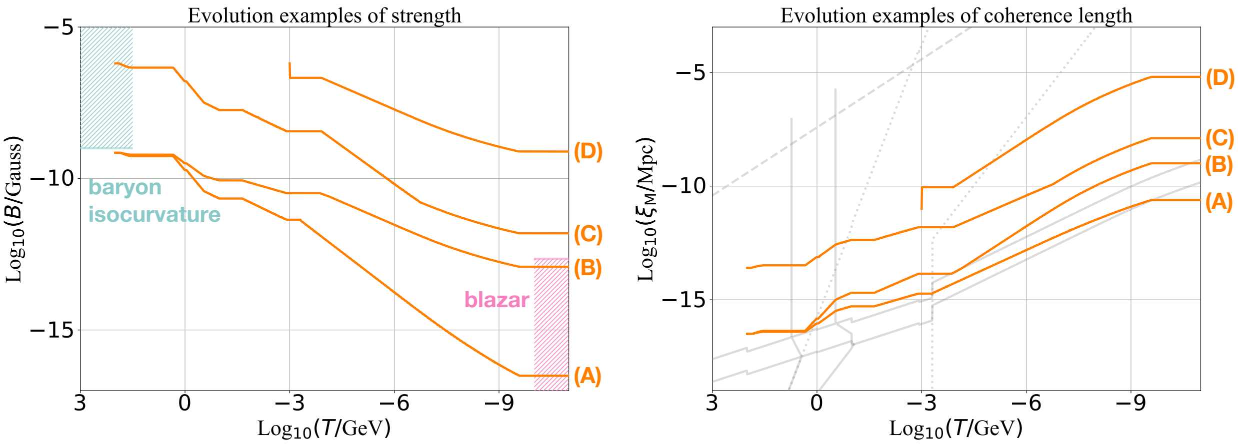

Figure 5.3: Evolution of the strength (orange solid lines in the left panel) and the coherence length (orange solid lines in the right panel) of magnetic fields for the initial conditions (A–D). The pale blue-hatched region is the exclusion at the electroweak temperature by the baryon isocurvature problem. Pale pink-hatched regions are below the observational lower limit of the intergalactic magnetic fields in void regions. The pale gray lines in the right panel are for the comparison with Fig. 5.2.

accept this estimate, the estimate of the resultant magnetic fields for (C,D) changes, but the conclusion that magnetogenesis scenarios at or below the electroweak scale are promising is the same.

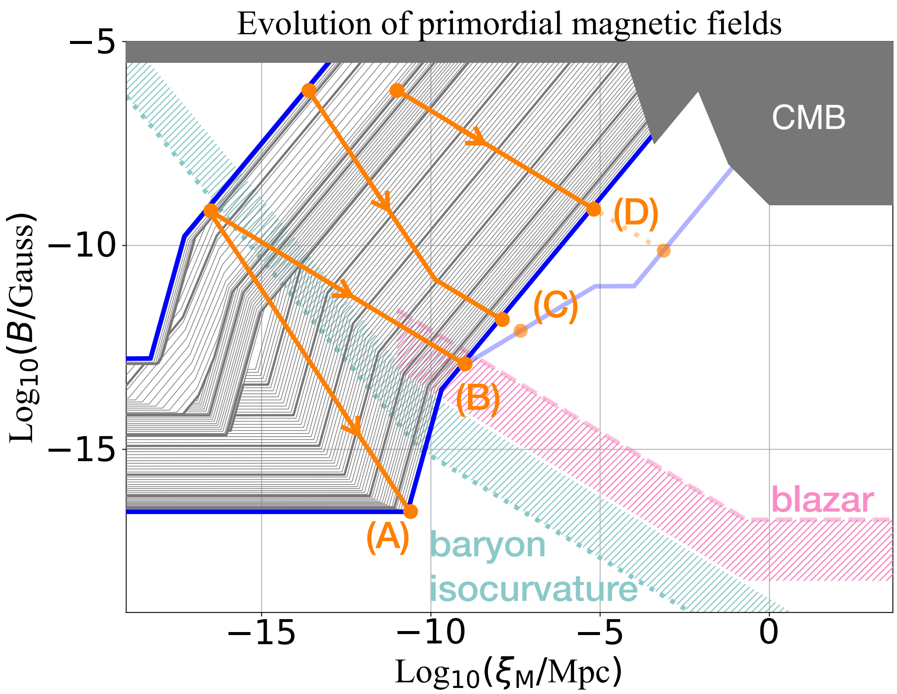

Figure 5.4: The summary plot in the ξ_M-B plain. Shaded or hatched regions imply the constraints on primordial magnetic fields (same as Fig. 2.3). CMB upper bounds on the magnetic field strength (gray-shaded region), lower bound on the strength of the observed intergalactic magnetic fields in void regions (pink-hatched region), and the upper bound at the electroweak scale that arises from the baryon isocurvature problem (blue-hatched region) are shown together with the evolution paths for the initial conditions (A–D) (orange solid arrows, essentially the same as Fig. 5.3) and the time-scale lines at temperatures of every 0.1 order of magnitude (thin gray solid lines, same as Fig. 5.1). In particular, the time-scale lines at the electroweak scale and the recombination epoch are highlighted by the thick blue solid lines. A possible extension of the analysis at the recombination epoch [43] is also shown (faint blue solid line).

Finally, apart from the implication on magnetogenesis scenarios, let us explain thoroughly what is the physics that governs the evolution of primordial magnetic fields, by choosing the initial condition (C) as a representative example.

See Fig. 5.5. The top panel shows the evolution of the helicity fraction ϵ. The magnetic field is almost non-helical, initially, but it becomes more and more helical as it decays because the net magnetic helicity density $\epsilon B^2 \xi_\mathrm{M}$ is conserved (Eq. (4.54)). At around 100 eV, it becomes maximally helical, and the relevant conservation law changes from Eq. (4.33) to Eq. (4.19). Because of this transition, the slopes of the lines for (C) in Fig. 5.3 change at the temperature.

Actually, the system for the initial condition (C) is always magnetically dominant, non-linear, and governed by fast magnetic reconnection. Then, only whether the shear viscosity or the drag force is dominant matters, according to the classification criteria. The second top panel of Fig. 5.5 shows the ratio between the mean free paths of neutrinos or photons and the kinetic coherence length. The neutrino mean free path becomes longer at around $5\,\mathrm{GeV}$, meaning that neutrino contribution to shear viscosity vanishes and the one to drag force turns on at the temperature. Similarly, photons begin to contribute as a drag term, when electrons become massive. Now we can compare the time scales of viscosity dissipation and frictional dissipation, by evaluating r_{diss}. From the second bottom panel, we understand that viscosity dissipation is dominant almost all the time except $5\,\mathrm{GeV} \gtrsim T \gtrsim 0.3\,\mathrm{GeV}$.

Then, the physical processes that dissipate the magnetic energy are viscous fast reconnection (discussed in Sec. 4.5.1.6) due to the lepton-lepton collision including neutrinos when $T \gtrsim 5\,\mathrm{GeV}$, dragged fast reconnection (Sec. 4.5.1.8) due to neutrino drag force when $5\,\mathrm{GeV} \gtrsim T \gtrsim 0.3\,\mathrm{GeV}$, viscous fast reconnection (Sec. 4.5.1.6) due to photon viscosity when $0.3\,\mathrm{GeV} \gtrsim T \gtrsim 500\,\mathrm{keV}$, and finally viscous fast reconnection (Secs. 4.5.1.6 and 4.5.1.2) due to proton viscosity after that until recombination.

In the bottom panel of Fig. 5.5, we compare the relevant decay time scales with the conformal time. Equation (4.3) or, equivalently, $\tau_{\mathrm{decay}}/\tau = 1$ implies that the magnetic field is decaying at the temperature. On the other hand, when Eq. (4.2) or, equivalently, $\tau_{\mathrm{decay}}/\tau > 1$ is satisfied, the magnetic field is frozen, as can be seen by the flat lines for (C) in Fig. 5.3.

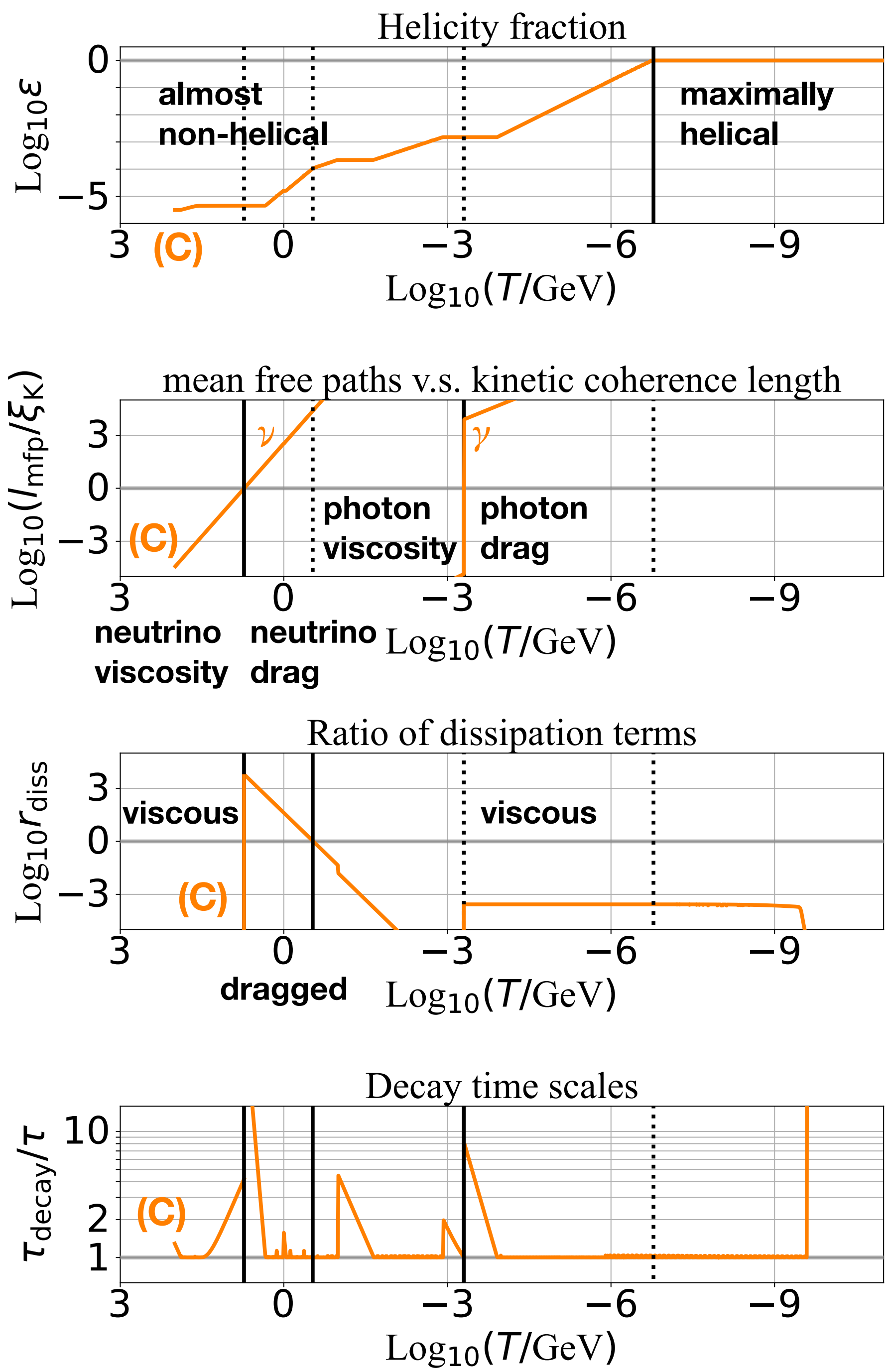

Figure 5.5: Transition of the regimes for the initial condition (C). Top: Evolution of helicity fraction ϵ, Second top: Comparison between mean free paths of neutrinos and photons and the kinetic coherence length. Second bottom: Ratio of dissipation terms. Bottom: Comparison between decay time scales and the conformal time.

5.2.2 Prescription for the usage

For the practical purpose, one can use Fig. 5.4 in the following way.

1. Specify the initial conditions $B_{\rm ini}, \xi_{\rm ini}, \epsilon_{\rm ini}$, and $T_{\rm ini}$.

2. Put a point at $(\xi_{\rm M,ini}, B_{\rm ini})$ in the $\xi_{\rm M}$-B plain in the figure.

3. Draw a line $B^2\xi_{\rm M} = \epsilon_{\rm ini}B_{\rm ini}^2\xi_{\rm M,ini}$.

4. Look for the time-scale line (thin gray line) corresponding to the temperature $T < T_{\rm ini}$ of interest.

5. If $\epsilon_{\rm ini} = 1$ initially, find the intersection of the line $B^2\xi_{\rm M} = B_{\rm ini}^2\xi_{\rm M,ini}$ and the time-scale line at T.

6. Otherwise, draw a line $B^4\xi_{\rm M}^5 = B_{\rm ini}^4\xi_{\rm M,ini}^5$ and find the intersection of this line and the time-scale line at T. If the intersection is below the line $B^2\xi_{\rm M} = \epsilon_{\rm ini}B_{\rm ini}^2\xi_{\rm M,ini}$, forget about that intersection and rather find the intersection of the line $B^2\xi_{\rm M} = \epsilon_{\rm ini}B_{\rm ini}^2\xi_{\rm M,ini}$ and the time-scale line at T.

Then, the point in the $\xi_{\rm M}$-B plain that one finds as the intersection of two lines represents the solution, $B(T), \xi_{\rm M}(T)$, which may be discussed in connection with whatever conditions one has at temperature T. For the analytic expression, one should consult Table 4.1 and find the formula for the relevant regime.

Chapter 6

Conclusion

In conclusion, we analyzed the evolution of primordial magnetic fields before the recombination epoch by classifying different magneto-hydrodynamic regimes and by integrating them consistently. The analysis is available for a given initial condition and makes a quantitative discussion on primordial magnetic fields possible. As a demonstration, we described the evolution of primordial magnetic fields for several specific choices of initial conditions, from which an implication is obtained. Namely, the low-scale inflationary magnetogenesis scenario with low reheating temperatures below the electroweak scale is a viable option to explain the origin of the intergalactic magnetic fields.

Let us summarize what is discussed on each point, by going through every chapter.

In Chap. 2, we overviewed the history of the early universe and constraints on primordial magnetic fields. In particular, the baryon isocurvature problem puts a strong constraint on primordial magnetic fields at the electroweak scale. To connect such discussions in the early universe with the observations in the present universe, we have to understand their time evolution.

In Chap. 3, we reviewed the basic formalism of magneto-hydrodynamics. Despite the difficulty of solving the non-linear system, the self-similar decay of the energy spectrum in the homogeneous and isotropic turbulence approximately holds, which reduces the problem to just determining the time dependences of the typical strength and the coherence length of the magnetic field. For this, however, an issue to be solved existed until very recently. When magnetic energy is dominant and the magnetic field is non-helical, any convincing reasons why the magnetic energy at large scales is enhanced was not known, although such a behavior has been observed numerically. However, the Hosking integral turned out to be conserved and to constrain the decay laws of magnetic fields, which solved the issue. Based on this discovery, we organized the comprehensive description of the scaling evolution of primordial magnetic fields in the subsequent chapters.

In Chap. 4, we carried out general discussions with the application in the early universe left for Chap. 5, based on our work [44, 45]. According to our strategy, the combination of two conditions, namely conserved quantities and decay time scales, determines the evolution of the properties of primordial magnetic fields. Two conserved quantities in magnetically dominated regimes are the net magnetic helicity and the Hosking integral, which quantifies the spatial fluctuation of magnetic helicity distribution. The usage of them as conserved quantities is exclusive. The conservation law of the net magnetic helicity density gives a constraint in Eq. (4.19) for maximally helical magnetic fields and that of the Hosking integral gives a constraint in Eq. (4.33) for non-helical magnetic fields. In addition, the kinetic energy at large scales plays a role in kinetically dominated regimes, but it turned out that kinetically dominated regimes easily enter the magnetically dominated regimes. In contrast to this, the magnetically dominated regimes never become kinetically dominated. As for the decay time scales, we derived formulas that relate B and ξ_{M} independently of the initial conditions. We have sixteen regimes in total, which are consistent with each other and are summarized in Table 4.1. As mentioned in Sec. 4.7, we admit that our analysis has a limitation of the applicable range. However, completing all the possibilities within that range is worth carrying out. Details of the analysis may be updated if a deeper understanding of magneto-hydrodynamics is established in the future, but still the basic strategy can be taken over.

In Chap. 5, we combined all the regimes and discussed the application to primordial magnetic fields, based on our work [27, 28, 44, 45]. The summary plot is Fig. 5.4. From this figure, we conclude that a low-scale inflationary magnetogenesis model can account for the origin of the intergalactic magnetic fields, while models above the electroweak scale are generally ruled out. This is just a demonstration of the applicability of our analysis. If one sets an initial condition of primordial magnetic fields, one can discuss their effect on events in the early universe at an arbitrary temperature afterward. Conversely, if one gets an implication of the existence of primordial magnetic fields, one can trace back their evolution and discuss possible magnetogenesis scenarios. In this way, our work has the potential to contribute widely to quantitative studies on primordial magnetic fields.

Appendix A

Dissipation coefficients

In this appendix, we list up the expressions of dissipation coefficients employed in Sec. 5. Values of these coefficients are shown in Fig. A.1. In particular, in the bottom-right panel of Fig A.1, we plot the magnetic Prandtl number as a function of temperature. It is always larger than unity before recombination. In addition, we plot the time dependence of the coefficients of the B-ξ_{M} relations, Eqs. (4.75), (4.96), (4.105), (4.112), (4.134), and (4.141), in panels of Fig. A.2.

Electric conductivity. The electric conductivity in the early universe before electrons become massive is approximated as [91]

$$\sigma_Y = \frac{6^4 \zeta(3)^2 \pi^{-3}}{\frac{\pi^2}{8} + \frac{20}{3} + \frac{2}{3}} \frac{a(T)T}{g'^2 \ln g'^{-1}}, \qquad T > T_{\mathrm{EW}}, \tag{A.1}$$

$$\sigma = \frac{12^4 \zeta(3)^2 \pi^{-3} N_{\mathrm{leptons}}}{3\pi^2 + 32 N_{\mathrm{species}}} \frac{a(T)T}{e^2 \ln e^{-1}}, \quad m_e < T < T_{\mathrm{EW}}, \tag{A.2}$$

where $e = 0.30$ and $g' = 0.36$ are the coupling constant of the $\mathrm{U}(1)_{\mathrm{em}}$ and $\mathrm{U}(1)_Y$ gauge fields, respectively. $m_e = 0.5\,\mathrm{MeV}$ is the electron mass, and $T_{\mathrm{EW}} \sim 0.1\,\mathrm{TeV}$ is the electroweak scale. N_{leptons} and N_{species} count the number of relevant charge careers, which are summarized in Table A.1. At lower temperatures, nonrelativistic electron-ion scattering is modeled by the Spitzer theory [43]

$$\sigma = \frac{4\pi e^2 a(T) n_{e,\mathrm{p}}(T)}{\nu_{ei,\mathrm{p}}(T) m_e} = \frac{4\pi a(T) T^{\frac{3}{2}}}{e^2 m_e^{\frac{1}{2}} \ln \Lambda_{ei}}, \qquad T < m_e, \tag{A.3}$$

where $n_{e,\mathrm{p}}$ is the physical electron number density, ν_{ei} is the electron-ion collision frequency, and $\ln \Lambda_{ei} \simeq 20$ is the Coulomb logarithm. σ as a function of temperature is plotted in the top-left panel of Fig A.1.

Shear viscosity. The shear viscosity in the early universe above $T > m_e$ is estimated in Ref. [91], which neglected the contribution from neutrinos. When the mean free path of neutrinos is shorter than the characteristic scales of the system, they contribute to the shear viscosity as well. In that case, the dimensionful Fermi constant $G_F = 1.17 \times 10^{-5}\,\mathrm{GeV}^{-2}$ comes into the expression, introducing non-trivial T dependence [92, 93]. When neutrinos contribute to the shear viscosity, their contribution becomes dominant.

$$\eta = \frac{1}{5}\frac{g_\nu}{g_{\text{fluid}}} l_{\nu\text{mfp}}, \qquad \text{with neutrinos included,} \tag{A.4}$$

$$\eta = \frac{\frac{45}{2\pi^2}\left(\frac{5}{2}\right)^3 \zeta(5)^2 \left(\frac{12}{\pi}\right)^5 \cdot \frac{3}{2}}{9\pi^2 + 224\left(5 + \frac{1}{2}\right)} \frac{1}{g'^4 \ln g'^{-1}} \frac{1}{g_{\text{fluid}} a(T) T}, \qquad T > T_{\text{EW}} \quad \text{without neutrinos,} \tag{A.5}$$

$$\eta = \frac{\frac{45}{2\pi^2}\left(\frac{5}{2}\right)^3 \zeta(5)^2 \left(\frac{12}{\pi}\right)^5 N_{\text{leptons}}}{9\pi^2 + 224 N_{\text{species}}} \frac{1}{e^4 \ln e^{-1}} \frac{1}{g_{\text{fluid}} a(T) T}, \qquad m_e < T < T_{\text{EW}} \quad \text{without neutrinos,} \tag{A.6}$$

where the neutrino mean free path is [93]

$$l_{\nu\text{mfp}} = \frac{1}{a(T) G_{\text{F}}^2 T^5}. \tag{A.7}$$

After electrons become massive, non-relativistic ion-ion scattering [43] and scattering between neutral hydrogens [29] are relevant before and after recombination, respectively. Similarly to neutrinos, photons contribute to the shear viscosity when their mean free path is shorter than the characteristic scales of the system.

$$\eta = \frac{1}{5}\frac{g_\gamma}{g_{\text{fluid}}} l_{\gamma\text{mfp}}, \qquad \text{with photons included,} \tag{A.8}$$

$$\eta = \frac{T^{\frac{5}{2}}}{a(T) e^4 n_{i,\text{p}}(T) m_p^{\frac{1}{2}} \ln \Lambda_{ii}}, \qquad T_{\text{rec}} < T < m_e \quad \text{without photons,} \tag{A.9}$$

$$\eta = \frac{T^{\frac{1}{2}}}{\pi a_{\text{B}}^2 a(T) n_{H,\text{p}}(T) m_p^{\frac{1}{2}}}, \qquad T < T_{\text{rec}} \quad \text{without photons,} \tag{A.10}$$

(A.11)

where the mean free path of photons is

$$l_{\gamma\mathrm{mfp}} = \frac{a(T)^2}{\sigma_{\mathrm{T}} n_e(T)}. \tag{A.12}$$

In the above expressions, $m_p \cong 1\,\mathrm{GeV}$ is the proton mass, $\ln \Lambda_{ii} \simeq 20$ is the Coulomb logarithm, $a_{\mathrm{B}} := 4\pi/(e^2 m_e)$ is the Bohr radius, and $\sigma_{\mathrm{T}} := (8\pi/3)(e^2/4\pi m_e)^2$ is the Thomson cross section. η as a function of temperature is plotted in the top-right panel of Fig A.1.

Drag force. When the mean free paths of particles, *i.e.,* photons and neutrinos, are larger than the characteristic length scales of the system, the particles act as a homogeneous background on which the fluid is dissipated via drag (friction) term, $-\alpha \boldsymbol{v}$. The drag coefficients due to neutrinos and photons are given by [29]

$$\alpha_\nu = \frac{g_\nu}{g_{\mathrm{fluid}} - 5.25} l_{\nu\mathrm{mfp}}^{-1}, \tag{A.13}$$

$$\alpha_\gamma = \frac{4}{3} \frac{\rho_\gamma}{\rho_{\mathrm{b}}} l_{\gamma\mathrm{mfp}}^{-1}. \tag{A.14}$$

Also, when the hydrogen atoms decouple from the plasma because of their neutralness, they account for the ambipolar drag [29, 94],

$$\alpha_{\mathrm{amb}} = 2\pi \left(\frac{e^2 a_{\mathrm{B}}^3}{m_p} \right)^{\frac{1}{2}} a(T) n_{H,p}. \tag{A.15}$$

In the matter-dominated era, the Hubble friction should also be taken into account,

$$\alpha_{\mathrm{Hubble}} := aH. \tag{A.16}$$

α as a function of temperature is plotted in the bottom-left panel of Fig A.1.

Table of degrees of freedom

T	T_0- $0.1\,\text{meV}-$	$T_{\text{rec}}, T_{\gamma\text{dec}}-$ $1\,\text{eV}-$	$m_e, T_{\nu\text{dec}}-$ $1\,\text{MeV}-$	$m_\mu, m_u, m_d,$ $m_s, T_{\text{QCD}}-$ $0.1\,\text{GeV}-$	m_τ, m_c, m_b $-$ $1\,\text{GeV}-$	$m_t, m_W,$ $T_{\text{EW}}-$ $0.1\,\text{TeV}-$
Relativistic contents of the plasma	$-$	γ	$\cdots,$ e, ν	$\cdots,$ μ, u, d, s, g	$\cdots,$ τ, c, b	$\cdots,$ t, H, W, Z
g g_s g_{fluid}	3.36 3.91 0	3.36 3.91 2	10.75	61.75	86.25	106.75
N_{leptons} N_{species}	0 0	0 0	1 1	2 4	3 20/3	(3/2) (5 + 1/2)

Table A.1: The values of $N_{\text{leptons}}, N_{\text{species}}$ from Ref. [91] as well as the values of g, g_s, g_{fluid}, as functions of the radiation temperature T. Both of $N_{\text{leptons}}, N_{\text{species}}$ count the number of fermions but are weighted by their lepton charges and electromagnetic charges. The symmetric phase belongs to a different regime but substitution of the values in the table into Eq. (A.2) with replacing the coupling coefficient $e \to g'$ reproduces Eq. (A.1) [91].

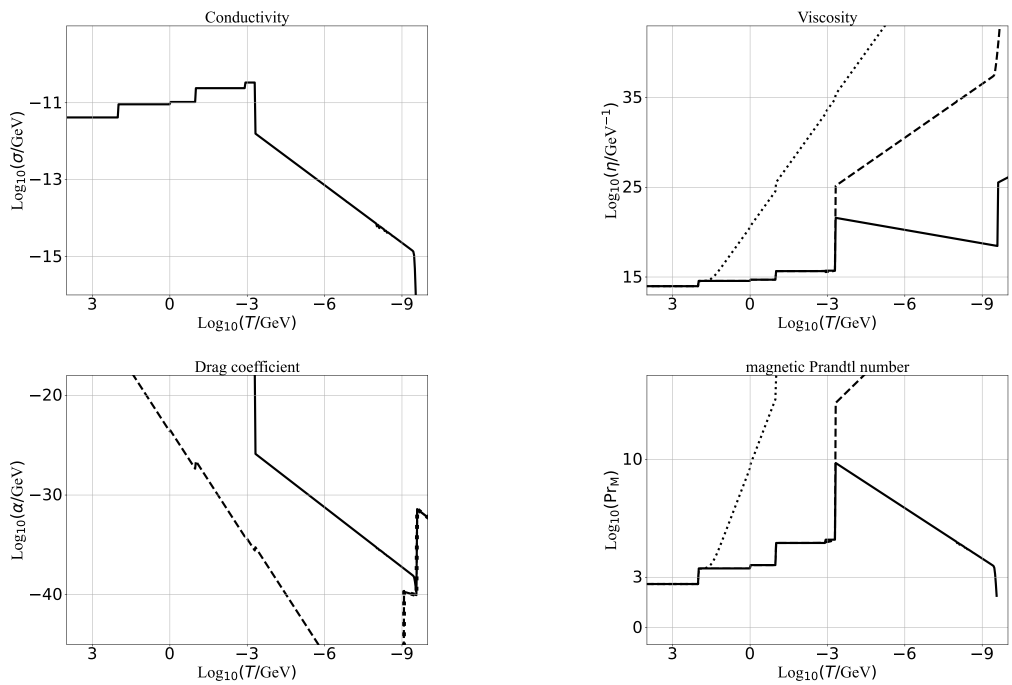

Figure A.1: Values of the dissipation coefficients, namely the electric conductivity σ (top left), the shear viscosity η (top right), and the drag coefficient α (bottom left). In addition, the magnetic Prandtl number Pr_M is plotted (bottom right). For each plot, the solid line is for the case when both neutrinos and photons decouple from the fluid, the dashed line is for the cases when only neutrinos decouple, and the dotted line is for the cases when both neutrinos and photons are still coupled with the fluid.

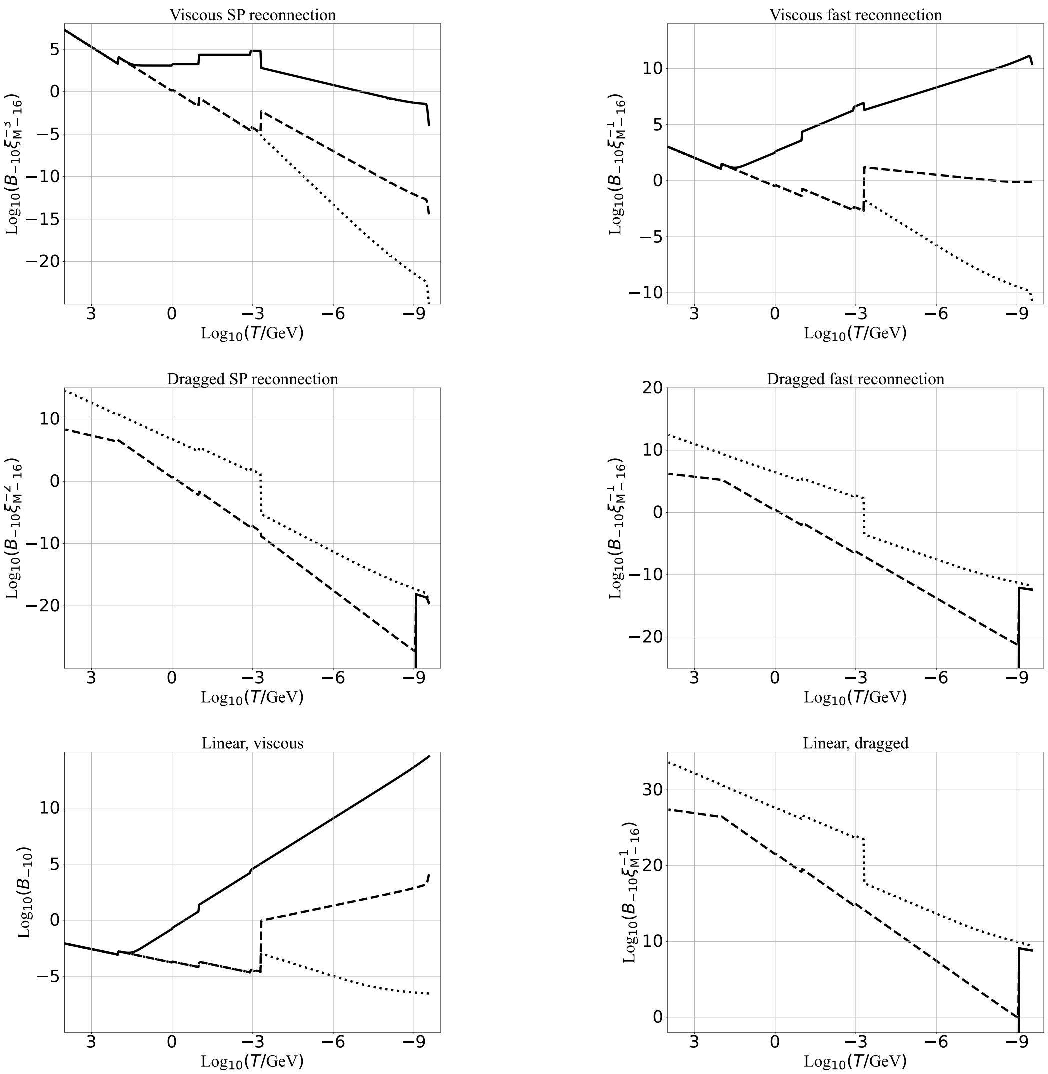

Figure A.2: The coefficients of the relation between B and ξ_{M} in the magnetically dominated regimes. $B_{-10} := B/10^{-10}\,\mathrm{G}$ and $\xi_{\mathrm{M}-16} := \xi_{\mathrm{M}}/10^{-16}\,\mathrm{Mpc}$. $B\xi_{\mathrm{M}}^{-3}$ for the viscous Sweet–Parker regime (top left), $B\xi_{\mathrm{M}}^{-1}$ for the viscous fast reconnection regime (top right), $B\xi_{\mathrm{M}}^{-2}$ for the dragged Sweet–Parker regime (middle left), $B\xi_{\mathrm{M}}^{-1}$ for the dragged fast reconnection regime (middle right), B for the linear and viscous regime (bottom left), and $B\xi_{\mathrm{M}}^{-1}$ for the linear and dragged regime (bottom right) are plotted. For each plot, the solid line is for the case when both neutrinos and photons decouple from the fluid, the dashed line is for the cases when only neutrinos decouple, and the dotted line is for the cases when both neutrinos and photons are still coupled with the fluid.

Appendix B

Blazar observation

In this appendix, we provide more information about the blazar lower limit on the strength of the intergalactic magnetic fields.

As explained in Sec. 2.2.2, the blazar constraints are based on the effect of intergalactic magnetic fields in voids on the paths of electron-positron pairs (See Fig. 2.1). Actually, the effect is two-fold. Namely,

- pair-halo [95–98]

and

- pair-echo [98–100]

have been expected to be observed.

Pair-halo refers to the effect that secondary GeV photons can arrive even from off-axis directions because the Lorentz force can redirect the cascade electron-positron pairs that are emitted in off-axis directions. Therefore, there is a possibility to observe GeV halos around the point-source TeV flux. Such halos were once claimed to be observed [7], but it was controversial because of the uncertainty that Fermi's point spread function had. Recent analysis by the Fermi group [16] conclude that they could not confirm the existence of GeV halos.

The redirection of cascade electron-positron pairs also takes some portion of on-axis flux away to completely random directions. Therefore, if we observe the energy spectrum of the arriving flux, a deficit in GeV range is observed. Most of the existing constraints are based on this effect [5, 6, 8–13, 15–17].

Pair-echo refers to the delay of the arrival of secondary GeV photons compared to the arrival of TeV photons or neutrinos. Only the GeV flux makes a detour because the Lorentz force bends paths of electron-positron pairs. This can be effective when we observe transient events, and some constraints are based on this effect [14, 18].

Moreover, pair-echo has been taken into account in most of the recent analyses on stable blazars. If the activity duration of a blazar is extremely long, GeV photons emitted from the past pile up the GeV flux that arrives today. Therefore, the observed GeV deficit places severer constraints if we assume longer activity duration of blazars. Conservatively, duration of blazar activity is assumed to be ~ 10 yrs [16].

Appendix C

Baryon isocurvature constraint

In this appendix, we summarize how we obtain the estimate in Eq. (2.5) based on Refs. [51, 52] and our work [27]. The quantities in this section are expressed in the physical unit rather than the comoving unit.

Suppose that primordial magnetic fields are generated before the electroweak symmetry breaking. We initially have a $\mathrm{U}(1)_Y$ gauge field configuration $Y_\mu(t, \boldsymbol{x})$. During the electroweak symmetry breaking, Y_μ and the weak boson W^3_μ mix to become the ordinary electromagnetic field A_μ. Let us take a time-dependent ansatz

$$W^3_\mu = \sin\theta_{\mathrm{w}}(t) A^{\mathrm{intermediate}}_\mu, \quad Y_\mu = \cos\theta_{\mathrm{w}}(t) A^{\mathrm{intermediate}}_\mu, \tag{C.1}$$

where $A^{\mathrm{intermediate}}_\mu$ is the "electromagnetic field" in the intermediate stage during the electroweak symmetry breaking. Before the electroweak symmetry breaking, $\theta_{\mathrm{w}} = 0$, and $A^{\mathrm{intermediate}}_\mu = Y_\mu$. On the other hand, after the electroweak symmetry braking, $\theta_{\mathrm{w}} = \theta_{\mathrm{w0}}$, where θ_{w0} is the weak mixing angle, and $A^{\mathrm{intermediate}}_\mu = A_\mu$. With this ansatz, the chiral anomaly of the Standard Model of particle physics implies

$$\begin{aligned}\dot{Q}_B &= 3\left(\dot{N}_{\mathrm{CS}} - \frac{g'^2}{16\pi^2}\dot{H}_Y\right) \\ &= \frac{3(g^2+g'^2)}{32\pi^2}\int d^3x \left[4(\sin^2\theta_{\mathrm{w0}} - \sin^2\theta_{\mathrm{w}})\boldsymbol{E}\cdot\boldsymbol{B} + 2\dot{\theta}_{\mathrm{w}}\sin 2\theta_{\mathrm{w}}\boldsymbol{A}\cdot\boldsymbol{B},\right]\end{aligned} \tag{C.2}$$

where $Q_B = \int d^3x n_B$ is the baryon number, $N_{\mathrm{CS}} := (g^2/8\pi^2)\int d^3x \epsilon_{ijk}\mathrm{Tr}(W_i\partial_j W_k + (2ig/3)W_iW_jW_k)$ is the Chern–Simons number, and $H_Y := \int d^3x \boldsymbol{A}_Y\cdot\boldsymbol{B}_Y$ is the hyper-magnetic helicity. We adopt the analytic formula for $\theta_{\mathrm{w}}(t)$ [101]

$$\cos^2\theta_{\mathrm{w}}(T) = \cos^2\theta_{\mathrm{w0}}\left(1 + \frac{11}{12}\frac{g^2\sin^2\theta_{\mathrm{w0}}T}{\pi M_W(T)}\right), \tag{C.3}$$

where a fitting formula [51]

$$M_W(T) := \frac{gv(T)}{2}, \quad v(T) = 0.23T\sqrt{162 - \frac{T}{\mathrm{GeV}}} \tag{C.4}$$

can be substituted. Then, the baryon number is sourced mainly by the second term in the integrand of Eq. (C.2) at around $\sim 160\,\mathrm{GeV}$. At this temperature range, the electroweak sphaleron also contribute as $\dot{Q}_B \sim$ Eq. (C.2) $- \gamma_{\mathrm{sph}} Q_B$, schematically. The balance between the sourcing effect and the spharelon washout, if evaluated at the sphaleron freeze-out, gives an approximate baryon abundance generated during the electroweak symmetry breaking [52]. By substituting $\dot{Q}_B \simeq 0$ and $\gamma_{\mathrm{sph}} \simeq H(130\,\mathrm{GeV})$, we obtain an approximate formula, Eq. (2.4), or

$$\eta_B = a(130\,\mathrm{GeV})^{-3} \mathcal{C} \boldsymbol{A} \cdot \boldsymbol{B} \quad \text{at} \sim 130\,\mathrm{GeV}, \tag{C.5}$$

where $\eta_B := n_B/s$ is the baryon-to-entropy ratio, and the coefficient is approximately given by $\mathcal{C} \simeq 0.1 \times (10^{-16}\,\mathrm{Mpc})^{-1}(10^{-8}\,\mathrm{G})^{-2}$, if the sphaleron process is properly taken into account [27]. If we interpret this baryon number production as a local process, we can relate $\delta\eta_B(\boldsymbol{x})$ and $\boldsymbol{A}(\boldsymbol{x}) \cdot \boldsymbol{B}(\boldsymbol{x})$, locally. Note that the gauge dependence is not problematic, if we integrate the quantities over small and magnetically closed volumes, as we discussed around Eq. (4.7). By taking into account the neutron diffusion, the baryon density distribution at the big-bang nucleosynthesis becomes

$$\delta\eta_B(T_{\mathrm{BBN}}, \boldsymbol{x}) = \int d^3y \delta\eta_B(130\,\mathrm{GeV}, \boldsymbol{y}) W(|\boldsymbol{y} - \boldsymbol{x}|), \tag{C.6}$$

where W is a window function that accounts for the smearing effect by neutrons. We take a normalized Gaussian function, $W(r) \propto \exp(-3r^2 k_{\mathrm{diffusion}}^2/2)$, where $k_{\mathrm{diffusion}} \simeq (0.0025\,\mathrm{pc})^{-1}$ is the diffusion length scale of neutrons [54]. Then, calculating the baryon isocurvature perturbations $\sqrt{\langle(\delta\eta_B/10^{-10})^2\rangle}(T_{\mathrm{BBN}})$, at the big-bang nucleosynthesis in terms of the magnetic power spectrum is a tedious but straightforward task.

The constraint is as shown in Fig. 2.3. It may appear non-trivial that even small scale magnetic fields are constrained, although the suppression by W at these scales is exponential. As already explained in Sec. 2.2.3, the trick is the non-linearity,

$\eta_B(130\,\mathrm{GeV}) \sim h \sim \boldsymbol{A}\cdot\boldsymbol{B} \sim B^2$, where $\sim$ stands for equalities of the power of B. Here we will give an explicit example of how small scale modes of the magnetic field couple and generate a large scale mode of baryon isocurvature perturbations. If we assume a monochromatic and globally non-helical magnetic field spectrum,

$$P_B(k) \propto \delta(k-k_0), \quad A_B(k) = 0, \tag{C.7}$$

then the power spectrum of magnetic helicity density becomes

$$\langle h(\boldsymbol{k})h(\boldsymbol{k}')\rangle \propto (2\pi)^3\delta^3(\boldsymbol{k}+\boldsymbol{k}')\Theta(2k_0-k)k\left(1-\frac{k^2}{4k_0^2}\right)^2, \tag{C.8}$$

where Θ is the Heaviside theta function. From this, we understand that magnetic helicity density has corresponding modes with finite amplitudes $\propto k$ for small k. This k dependence is the origin of the proportionality to ξ_{M} of the suppression factor.

It might be more intuitive to discuss the two point function of magnetic helicity density. It becomes [27]

$$\langle h(\boldsymbol{x})h(\boldsymbol{x}+\boldsymbol{r})\rangle \propto \frac{2}{k_0^2r^2}+\frac{2}{k_0^4r^4}+\frac{3}{k_0^6r^6}-\frac{6}{k_0^5r^5}\sin(2k_0r)+\left(\frac{4}{k_0^4r^4}-\frac{3}{k_0^6r^6}\right)\cos(2k_0r), \tag{C.9}$$

which has an infrared tail $\propto r^{-2}$, implying that magnetic helicity density has a long-range mode. If we assume more realistic power spectra of the magnetic field, the two point function of magnetic helicity density is typically more suppressed at large scales. The suppression is still a power-law, and hence small-scale magnetic fields are constrained as well.

Appendix D

Low-scale inflationary magnetigenesis

In this appendix, we summarize the low-scale inflationary magnetogenesis introduced in Sec. 5.2, based on our work [28]. The quantities in this section are expressed mostly in the physical unit rather than the comoving unit.

The scenario is the combination of two ideas. One is the introduction of a pseudo-scalar inflaton ϕ coupled with the electromagnetic field as

$$\sqrt{-g_{\mathrm{M}}}\mathcal{L} \supset -\frac{g}{4}\phi F_{\mu\nu}\tilde{F}^{\mu\nu}, \tag{D.1}$$

where $\tilde{F}^{\mu\nu} := (1/2)\epsilon^{\mu\nu\rho\sigma}F_{\mu\nu}$, $F_{\mu\nu} := \partial_\mu A_\nu - \partial_\nu A_\mu$, and g is a dimensionful coupling constant. With the canonical kinetic term for the photon field, the equation of motion for each circular polarization mode function becomes

$$\ddot{A}_\pm(k) + H\dot{A}_\pm(k) + \frac{k}{a}\left(\frac{k}{a} \mp g\dot{\phi}\right)A_\pm(k) = 0. \tag{D.2}$$

When $|\dot{\phi}|$ is large enough, the third term acts as a negative mass term, and only either of the modes is amplified by the tachyonic instability [22]. Therefore, the model has a possibility to generate helical magnetic fields, which has the advantage of leaving stronger magnetic fields at the recombination epoch. The other idea is the use of a flat inflection point. We choose the GMSSM potential [102, 103]

$$V(\phi) := \Lambda^4\left[\frac{1}{2}\left(\frac{\phi}{\phi_0}\right)^2 - \frac{\alpha}{3}\left(\frac{\phi}{\phi_0}\right)^6 + \frac{\alpha}{10}\left(\frac{\phi}{\phi_0}\right)^{10}\right], \tag{D.3}$$

where α is taken to be almost unity. When $\alpha = 1$, $\phi = \phi_0$ becomes the flat inflection point, so that the slow-roll parameters vanish at the same time. We slightly deviate

α from unity to realize low-scale inflation in a consistent manner with the CMB observations. Λ is chosen so that the model reproduces the observed spectral amplitude, and ϕ_0 controls the reheating temperature. Since the potential in Eq. (D.3) is symmetric under the transformation $\phi \to -\phi$, we can combine these two ideas.

According to our numerical calculation, if we lower the reheating temperature $T_{\rm reh}$, the produced magnetic field tends to be non-helical as

$$
\begin{aligned}
&B = 7.0 \times 10^{-7}\,\mathrm{G}, \quad \xi_{\rm M} = 2.7 \times 10^{-14}\,\mathrm{Mpc}\left(\frac{T_{\rm reh}}{100\,\mathrm{GeV}}\right)^{-0.68}, \\
&\epsilon = 3.1 \times 10^{-6}\left(\frac{T_{\rm reh}}{100\,\mathrm{GeV}}\right)^{0.55}, \qquad \text{(D.4)}
\end{aligned}
$$

reflecting our finding that rather the parametric resonance, which enhances both of the polarization modes, after the inflation end than the tachyonic instability becomes the dominant contribution for low reheating temperatures. Based on this, we switch the potential to the much flat one after the inflation end. It inhibits the rapid oscillation of the inflaton field and realizes extended tachyonic instability to generate maximally helical field

$$
\begin{aligned}
&B = 7.0 \times 10^{-7}\,\mathrm{G}, \quad \xi_{\rm M} = 1.4 \times 10^{-14}\,\mathrm{Mpc}\left(\frac{T_{\rm reh}}{100\,\mathrm{GeV}}\right)^{-0.57}, \\
&\epsilon = 1, \qquad \text{(D.5)}
\end{aligned}
$$

even for low reheating temperatures. Although we should mention that our results are extrapolations from the range $10^{11}\,\mathrm{GeV} < T_{\rm reh} < 10^{12-13}\,\mathrm{GeV}$ due to the difficulty of carrying out numerical simulations, our results demonstrate that these scenarios with both low reheating temperatures and the helical magnetic fields are advantageous as the magnetogenesis scenario, as explained in the main text.

Appendix E

Numerical results in the literature

In this appendix, we compare the numerical results in the literature with the theoretical evolution laws obtained in Sec. 4.5. Following the convention in the literature [34], we parametrize the evolution of the system as

$$B^2(\tau) \propto \tau^{-p_{\mathrm{M}}}, \quad \xi_{\mathrm{M}}(\tau) \propto \tau^{q_{\mathrm{M}}}, \tag{E.1}$$

for the magnetic field and

$$v^2(\tau) \propto \tau^{-p_{\mathrm{K}}}, \quad \xi_{\mathrm{K}}(\tau) \propto \tau^{q_{\mathrm{K}}}, \tag{E.2}$$

for the velocity field.

In Table E.1, we summarize the results of direct numerical simulations in the literature [29,31,33,34,40] in comparison with the theoretical expectations in Ref. [29] and the one in Secs. 4.5.1.5, 4.5.1.1, and 4.5.4.1.

By plotting residuals of numerical values of $p_{\mathrm{M}}, q_{\mathrm{M}}, p_{\mathrm{K}}$, and q_{K} in Fig. E.1, we see that non-helical simulations suggest a better description of numerical results by our analyses compared to Ref. [29]. The large dots, which scatter closely around the origin, represent our results for non-helical magnetic turbulences, and the large crosses, which scatter off the origin, represent the results according to Ref. [29].

It is unclear that maximally helical runs reach the scaling regimes in the limited simulation run time, and the residuals from both analytic expectations scatter off the origin (small dots and crosses in Fig. E.1). We should wait for further numerical investigations to obtain more reliable support for analytic analyses.

Run	$\frac{E_{\rm K}}{E_{\rm M}}$	$n_{\rm M}$	$\lvert\epsilon\rvert$	$(p_{\rm M}, q_{\rm M}, p_{\rm K}, q_{\rm K})_{\rm num}$	$(p_{\rm M} = p_{\rm K}, q_{\rm M} = q_{\rm K})_{\rm BJ}$	$(p_{\rm M}, q_{\rm M}, p_{\rm K}, q_{\rm K})_{\rm th}$
BJ-NH3	–	3	0	$(1.05, -, -, -)$	$(1.20, 0.40)$	$(1.18, 0.47, 1.12, 0.53)^{*1}$
BJ-NH4	–	4	0	$(1.12, -, -, -)$	$(1.33, 0.33)$	$(1.18, 0.47, 1.12, 0.53)^{*1}$
BJ-NH5	–	5	0	$(1.19, -, -, -)$	$(1.43, 0.29)$	$(1.18, 0.47, 1.12, 0.53)^{*1}$
BJ-MH3	–	3	1	$(0.50, -, -, -)$	$(0.67, 0.67)$	$(0.57, 0.57, 0.71, 0.43)^{*1}$
BJ-MH4	–	4	1	$(0.55, -, -, -)$	$(0.67, 0.67)$	$(0.57, 0.57, 0.71, 0.43)^{*1}$
BJ-MH5	–	5	1	$(0.57, -, -, -)$	$(0.67, 0.67)$	$(0.57, 0.57, 0.71, 0.43)^{*1}$
BKT (BK-ii)	$0 \to 0.36$	5	0	$(1.02, 0.47, 0.97, 0.41)$	$(1.43, 0.29)$	$(0.92, 0.37, 1.09, 0.30)^{*2}$
BK-iii	$0 \to 0.24$	5	> 0	$(0.62, 0.59, 0.71, 0.63)$	$(0.67, 0.67)$	$(0.45, 0.45, 0.78, 0.24)^{*2}$
BKM+-A	$0.1 \to 0.40$	5	0	$(1.04, 0.37, 1.08, 0.37)$	$(1.43, 0.29)$	$(0.92, 0.37, 1.09, 0.30)^{*2}$
BKM+-B	$1 \to 0.42$	5	0	$(1.03, 0.36, 1.10, 0.33)$	$(1.43, 0.29)$	$(0.92, 0.37, 1.09, 0.30)^{*2}$
BKM+-C	$10 \to 1.0$	5	0	$(1.26, 0.31, 1.34, 0.28)$	$(1.43, 0.29)$	$(1.43, 0.29, 1.43, 0.29)$
BKM+-D	$1 \to 0.31$	3	0	$(1.03, 0.38, 1.06, 0.36)$	$(1.20, 0.40)$	$(1.06, 0.42, 1.11, 0.42)^{*3}$
BKM+-E	$1 \to 0.38$	3	0	$(0.95, 0.36, 1.01, 0.36)$	$(1.20, 0.40)$	$(1.06, 0.42, 1.11, 0.42)^{*3}$
BKM+-F	$0 \to 0.38$	3	0	$(0.94, 0.35, 0.97, 0.36)$	$(1.20, 0.40)$	$(1.06, 0.42, 1.11, 0.42)^{*3}$
BKM+-G	$1 \to 0.31$	3	$0.06 \to 1$	$(0.73, 0.55, 1.03, 0.49)$	$(0.67, 0.67)$	$(0.51, 0.51, 0.74, 0.34)^{*3}$
BKM+-H	$1 \to 0.77$	5	$0 \to^{*4} 1$	$(0.76, 0.46, 0.79, 0.22)$	$(0.67, 0.67)$	$(0.45, 0.45, 0.78, 0.24)^{*2}$
BKM+-I	$1 \to 0.43$	5	$1 \to^{*4} 1$	$(0.58, 0.49, 0.67, 0.36)$	$(0.67, 0.67)$	$(0.45, 0.45, 0.78, 0.24)^{*2}$
BKM+-J	$1 \to 0.34$	5	$1 \to^{*4} 1$	$(0.57, 0.48, 0.80, 0.46)$	$(0.67, 0.67)$	$(0.45, 0.45, 0.78, 0.24)^{*2}$
ZSB-K60D1c	< 1	5	0	$(0.84, 0.38, -, -)$	$(1.43, 0.29)$	$(1.18, 0.47, 1.12, 0.53)^{*5}$
ZSB-K60D1bt	< 1	5	0	$(1, 0.4, -, -)$	$(1.43, 0.29)$	$(0.92, 0.37, 1.09, 0.30)^{*2}$
ZSB-K60D1bc	< 1	5	0	$(1.07, 0.43, -, -)$	$(1.43, 0.29)$	$(1.18, 0.47, 1.12, 0.53)^{*5}$

Table E.1: Numerical results read off from the figures or taken from tables and main text in the literature [29, "BJ"], [31, "BKT"], [33, "BK"], [34, "BKM+"], and [40, "ZSB"] (fifth column) and theoretical predictions base on the anlyses in Ref. [29, "BJ"] (sixth column) and our analyses (last column). From the second to fourth columns show the conditions of each run. Namely, the initial and final energy ratio, the IR spectral tilt of the magnetic field, and the initial and final magnetic helicity fraction. *1: It is not explicit how the values of dissipation coefficients are set in the runs. In the table, we show the theoretical predictions, assuming constant dissipation coefficients. *2: They set $\sigma^{-1}, \eta \propto \tau^{-0.43}$. *3: They set $\sigma^{-1}, \eta \propto \tau^{-0.20}$. *4: In these runs, the velocity field is helical. Kinetic helicity is converted to magnetic helicity at large scales, and magnetic helicity with the opposite sign at small scales are selectively dissipated, resulting in the nontrivial evolution of magnetic helicity fraction [104]. At the end of the runs when the values of scaling exponents are measured, the magnetic field is (at least almost) maximally helical. *5: They set constant dissipation coefficients.

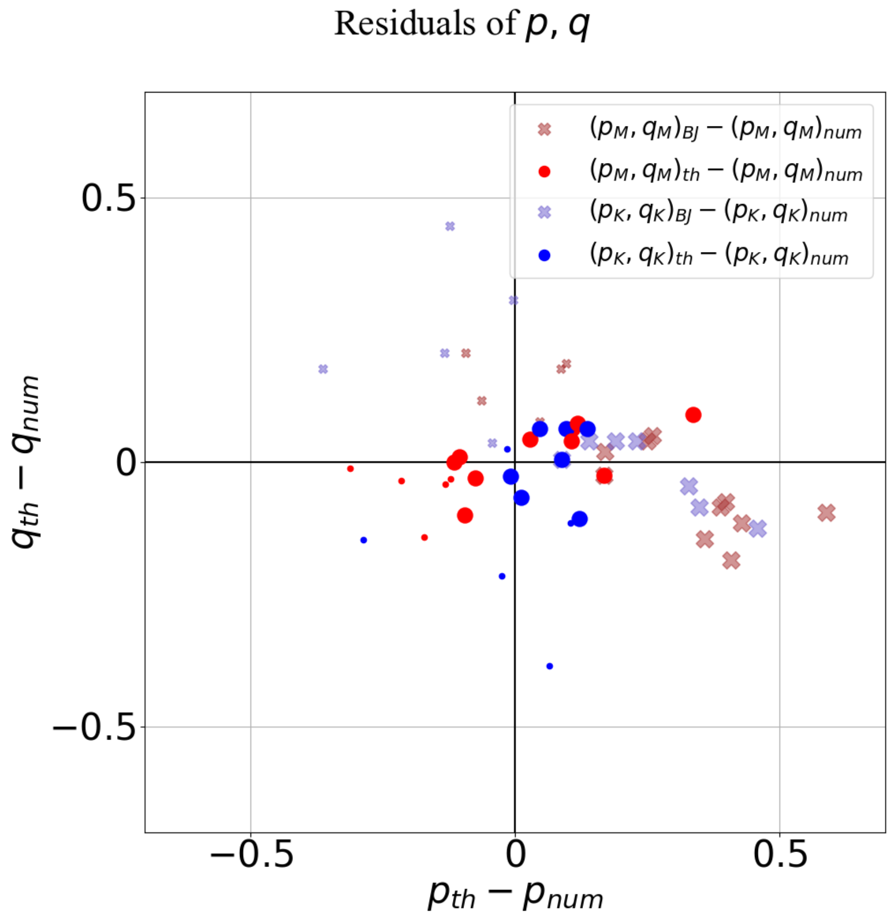

Figure E.1: Residuals of numerical values of $p_{\rm M}, q_{\rm M}, p_{\rm K}, q_{\rm K}$ obtained by Refs. [29, 31, 33, 34, 40]. Dots are the residuals from our analyses, and crosses are residuals from the analysis by Ref. [29]. Red symbols are for the magnetic field, and blue ones are for the velocity field. Large ones are for non-helical simulations, and small ones are for maximally helical simulations.

Appendix F

Matrix form of the equations

In this section, we summarize the set of equations we solved in each magnetically dominated regime discussed in Sec. 4.5. It might be helpful for solving the set of equations at once.

Visous Sweet–Parker regimes. For maximally helical fields (Sec. 4.5.1.1), the set of equations to solve is

$$M^{\mathrm{MD-NL}}_{\mathrm{MH-V-SP}} \boldsymbol{\xi} = \boldsymbol{b}^{\mathrm{MD-NL}}_{\mathrm{MH-V-SP}}, \tag{F.1}$$

where we define

$$M^{\mathrm{MD-NL}}_{\mathrm{MH-V-SP}} := \begin{pmatrix} 0 & +1 & 0 & -1 & +1 & -1 \\ 0 & 0 & 0 & +1 & +1 & 0 \\ +2 & 0 & 0 & 0 & 0 & -2 \\ 0 & +1 & 0 & 0 & -1 & 0 \\ 0 & +1 & +2 & -1 & 0 & -2 \\ +2 & +1 & 0 & 0 & 0 & 0 \end{pmatrix}, \ \boldsymbol{b}^{\mathrm{MD-NL}}_{\mathrm{MH-V-SP}} := \begin{pmatrix} 0 \\ -\log\sigma \\ \log(\rho+p)\sigma\eta \\ \log\tau \\ 0 \\ \log B_{\mathrm{ini}}^2 \xi_{\mathrm{ini}} \end{pmatrix}, \tag{F.2}$$

and

$$\boldsymbol{\xi} := \begin{pmatrix} \log B \\ \log \xi_{\mathrm{M}} \\ \log v \\ \log \xi_{\mathrm{K}} \\ \log v_{\mathrm{in}} \\ \log v_{\mathrm{out}} \end{pmatrix}.. \tag{F.3}$$

For non-helical fields (Sec. 4.5.1.5),

$$M^{\mathrm{MD-NL}}_{\mathrm{NH-V-SP}} \boldsymbol{\xi} = \boldsymbol{b}^{\mathrm{MD-NL}}_{\mathrm{NH-V-SP}}, \tag{F.4}$$

where we define

$$M^{\mathrm{MD-NL}}_{\mathrm{NH-V-SP}} := \begin{pmatrix} 0 & +1 & 0 & -1 & +1 & -1 \\ 0 & 0 & 0 & +1 & +1 & 0 \\ +2 & 0 & 0 & 0 & 0 & -2 \\ 0 & +1 & 0 & 0 & -1 & 0 \\ 0 & +1 & +2 & -1 & 0 & -2 \\ +4 & +5 & 0 & 0 & 0 & 0 \end{pmatrix}, \ \boldsymbol{b}^{\mathrm{MD-NL}}_{\mathrm{NH-V-SP}} := \begin{pmatrix} 0 \\ -\log\sigma \\ \log(\rho+p)\sigma\eta \\ \log\tau \\ 0 \\ \log B^4_{\mathrm{ini}}\xi^5_{\mathrm{ini}} \end{pmatrix}.. \tag{F.5}$$

Visous fast reconnection regimes. For maximally helical magnetic fields (Sec. 4.5.1.2),

$$M^{\mathrm{MD-NL}}_{\mathrm{MH-V-fast}}\boldsymbol{\xi} = \boldsymbol{b}^{\mathrm{MD-NL}}_{\mathrm{MH-V-fast}}, \tag{F.6}$$

where we define

$$M^{\mathrm{MD-NL}}_{\mathrm{MH-V-fast}} := \begin{pmatrix} 0 & -1 & 0 & +2 & 0 & +1 \\ 0 & 0 & 0 & 0 & +2 & -2 \\ +2 & 0 & 0 & 0 & 0 & -2 \\ 0 & +1 & 0 & 0 & -1 & 0 \\ 0 & +1 & +2 & -1 & 0 & -2 \\ +2 & +1 & 0 & 0 & 0 & 0 \end{pmatrix}, \ \boldsymbol{b}^{\mathrm{MD-NL}}_{\mathrm{MH-V-fast}} := \begin{pmatrix} -\log\sigma \\ -\log S_{\mathrm{c}} \\ \log(\rho+p)\sigma\eta \\ \log\tau \\ 0 \\ \log B^2_{\mathrm{ini}}\xi_{\mathrm{ini}} \end{pmatrix}. \tag{F.7}$$

For non-helical fields (Sec. 4.5.1.5),

$$M^{\mathrm{MD-NL}}_{\mathrm{NH-V-fast}}\boldsymbol{\xi} = \boldsymbol{b}^{\mathrm{MD-NL}}_{\mathrm{NH-V-fast}}, \tag{F.8}$$

where we define

$$M^{\mathrm{MD-NL}}_{\mathrm{NH-V-fast}} := \begin{pmatrix} 0 & -1 & 0 & +2 & 0 & +1 \\ 0 & 0 & 0 & 0 & +2 & -2 \\ +2 & 0 & 0 & 0 & 0 & -2 \\ 0 & +1 & 0 & 0 & -1 & 0 \\ 0 & +1 & +2 & -1 & 0 & -2 \\ +4 & +5 & 0 & 0 & 0 & 0 \end{pmatrix}, \ \boldsymbol{b}^{\mathrm{MD-NL}}_{\mathrm{NH-V-fast}} := \begin{pmatrix} -\log\sigma \\ -\log S_{\mathrm{c}} \\ \log(\rho+p)\sigma\eta \\ \log\tau \\ 0 \\ \log B^4_{\mathrm{ini}}\xi^5_{\mathrm{ini}} \end{pmatrix}. \tag{F.9}$$

Dragged Sweet–Parker regimes. For maximally helical fields (Sec. 4.5.1.3),

$$M^{\mathrm{MD-NL}}_{\mathrm{MH-D-SP}}\boldsymbol{\xi} = \boldsymbol{b}^{\mathrm{MD-NL}}_{\mathrm{MH-D-SP}}, \tag{F.10}$$

where we define

$$M^{\mathrm{MD-NL}}_{\mathrm{MH-D-SP}} := \begin{pmatrix} 0 & +1 & 0 & -1 & +1 & -1 \\ 0 & 0 & 0 & +1 & +1 & 0 \\ +2 & -1 & 0 & 0 & 0 & -1 \\ 0 & +1 & 0 & 0 & -1 & 0 \\ 0 & +1 & +2 & -1 & 0 & -2 \\ +2 & +1 & 0 & 0 & 0 & 0 \end{pmatrix}, \quad \boldsymbol{b}^{\mathrm{MD-NL}}_{\mathrm{MH-D-SP}} := \begin{pmatrix} 0 \\ -\log\sigma \\ \log(\rho+p)\alpha \\ \log\tau \\ 0 \\ \log B^2_{\mathrm{ini}}\xi_{\mathrm{ini}} \end{pmatrix}. \tag{F.11}$$

For non-helical fields (Sec. 4.5.1.7),

$$M^{\mathrm{MD-NL}}_{\mathrm{NH-D-SP}}\boldsymbol{\xi} = \boldsymbol{b}^{\mathrm{MD-NL}}_{\mathrm{NH-D-SP}}, \tag{F.12}$$

where we define

$$M^{\mathrm{MD-NL}}_{\mathrm{NH-D-SP}} := \begin{pmatrix} 0 & +1 & 0 & -1 & +1 & -1 \\ 0 & 0 & 0 & +1 & +1 & 0 \\ +2 & -1 & 0 & 0 & 0 & -1 \\ 0 & +1 & 0 & 0 & -1 & 0 \\ 0 & +1 & +2 & -1 & 0 & -2 \\ +4 & +5 & 0 & 0 & 0 & 0 \end{pmatrix}, \quad \boldsymbol{b}^{\mathrm{MD-NL}}_{\mathrm{NH-D-SP}} := \begin{pmatrix} 0 \\ -\log\sigma \\ \log(\rho+p)\alpha \\ \log\tau \\ 0 \\ \log B^4_{\mathrm{ini}}\xi^5_{\mathrm{ini}} \end{pmatrix}. \tag{F.13}$$

Dragged fast reconnection regimes. For maximally helical fields (Sec. 4.5.1.4),

$$M^{\mathrm{MD-NL}}_{\mathrm{MH-D-fast}}\boldsymbol{\xi} = \boldsymbol{b}^{\mathrm{MD-NL}}_{\mathrm{MH-D-fast}}, \tag{F.14}$$

where we define

$$M^{\mathrm{MD-NL}}_{\mathrm{MH-D-fast}} := \begin{pmatrix} 0 & -1 & 0 & +2 & 0 & +1 \\ 0 & 0 & 0 & 0 & +2 & -2 \\ +2 & -1 & 0 & 0 & 0 & -1 \\ 0 & +1 & 0 & 0 & -1 & 0 \\ 0 & +1 & +2 & -1 & 0 & -2 \\ +2 & +1 & 0 & 0 & 0 & 0 \end{pmatrix}, \quad \boldsymbol{b}^{\mathrm{MD-NL}}_{\mathrm{MH-D-fast}} := \begin{pmatrix} -\log\sigma \\ -\log S_{\mathrm{c}} \\ \log(\rho+p)\alpha \\ \log\tau \\ 0 \\ \log B^2_{\mathrm{ini}}\xi_{\mathrm{ini}} \end{pmatrix}. \tag{F.15}$$

For non-helical fields (Sec. 4.5.1.8),

$$M^{\mathrm{MD-NL}}_{\mathrm{NH-D-fast}}\boldsymbol{\xi} = \boldsymbol{b}^{\mathrm{MD-NL}}_{\mathrm{NH-D-fast}}, \tag{F.16}$$

where we define

$$M^{\mathrm{MD-NL}}_{\mathrm{NH-D-fast}} := \begin{pmatrix} 0 & -1 & 0 & +2 & 0 & +1 \\ 0 & 0 & 0 & 0 & +2 & -2 \\ +2 & -1 & 0 & 0 & 0 & -1 \\ 0 & +1 & 0 & 0 & -1 & 0 \\ 0 & +1 & +2 & -1 & 0 & -2 \\ +4 & +5 & 0 & 0 & 0 & 0 \end{pmatrix}, \ \boldsymbol{b}^{\mathrm{MD-NL}}_{\mathrm{NH-D-fast}} \quad := \begin{pmatrix} -\log\sigma \\ -\log S_{\mathrm{c}} \\ \log(\rho+p)\alpha \\ \log\tau \\ 0 \\ \log B^4_{\mathrm{ini}}\xi^5_{\mathrm{ini}} \end{pmatrix}. \tag{F.17}$$

Linear and viscous regimes. For maximally helical fields (Sec. 4.5.2.1),

$$M^{\mathrm{MD-L}}_{\mathrm{MH-V}}\boldsymbol{\xi}' = \boldsymbol{b}^{\mathrm{MD-L}}_{\mathrm{MH-V}}, \tag{F.18}$$

where we define

$$M^{\mathrm{MD-L}}_{\mathrm{MH-V}} := \begin{pmatrix} 0 & +1 & 0 & -1 \\ +2 & -1 & -1 & +2 \\ 0 & 0 & -1 & +1 \\ +2 & +1 & 0 & 0 \end{pmatrix}, \quad \boldsymbol{b}^{\mathrm{MD-L}}_{\mathrm{MH-V}} := \begin{pmatrix} 0 \\ \log(\rho+p)\eta \\ \log\tau \\ \log B^2_{\mathrm{ini}}\xi_{\mathrm{ini}} \end{pmatrix}, \tag{F.19}$$

and

$$\boldsymbol{\xi}' := \begin{pmatrix} \log B \\ \log\xi_{\mathrm{M}} \\ \log v \\ \log\xi_{\mathrm{K}} \end{pmatrix}. \tag{F.20}$$

For non-helical fields (Sec. 4.5.2.3),

$$M^{\mathrm{MD-L}}_{\mathrm{NH-V}}\boldsymbol{\xi}' = \boldsymbol{b}^{\mathrm{MD-L}}_{\mathrm{NH-V}}, \tag{F.21}$$

where we define

$$M^{\mathrm{MD-L}}_{\mathrm{NH-V}} := \begin{pmatrix} 0 & +1 & 0 & -1 \\ +2 & -1 & -1 & +2 \\ 0 & 0 & -1 & +1 \\ +4 & +5 & 0 & 0 \end{pmatrix}, \quad \boldsymbol{b}^{\mathrm{MD-L}}_{\mathrm{NH-V}} := \begin{pmatrix} 0 \\ \log(\rho+p)\eta \\ \log\tau \\ \log B^4_{\mathrm{ini}}\xi^5_{\mathrm{ini}} \end{pmatrix}. \tag{F.22}$$

Linear and dragged regimes. For maximally helical fields (Sec. 4.5.2.2),

$$M^{\mathrm{MD-L}}_{\mathrm{MH-D}}\boldsymbol{\xi}' = \boldsymbol{b}^{\mathrm{MD-L}}_{\mathrm{MH-D}}, \tag{F.23}$$

where we define

$$M^{\mathrm{MD-L}}_{\mathrm{MH-D}} := \begin{pmatrix} 0 & +1 & 0 & -1 \\ +2 & -1 & -1 & 0 \\ 0 & 0 & -1 & +1 \\ +2 & +1 & 0 & 0 \end{pmatrix}, \quad \boldsymbol{b}^{\mathrm{MD-L}}_{\mathrm{MH-D}} := \begin{pmatrix} 0 \\ \log(\rho+p)\alpha \\ \log\tau \\ \log B^2_{\mathrm{ini}}\xi_{\mathrm{ini}} \end{pmatrix}. \tag{F.24}$$

For non-helical fields (Sec. 4.5.2.4),

$$M^{\mathrm{MD-L}}_{\mathrm{NH-D}}\boldsymbol{\xi}' = \boldsymbol{b}^{\mathrm{MD-L}}_{\mathrm{NH-D}}, \tag{F.25}$$

where we define

$$M^{\mathrm{MD-L}}_{\mathrm{NH-D}} := \begin{pmatrix} 0 & +1 & 0 & -1 \\ +2 & -1 & -1 & 0 \\ 0 & 0 & -1 & +1 \\ +4 & +5 & 0 & 0 \end{pmatrix}, \quad \boldsymbol{b}^{\mathrm{MD-L}}_{\mathrm{NH-D}} := \begin{pmatrix} 0 \\ \log(\rho+p)\alpha \\ \log\tau \\ \log B^4_{\mathrm{ini}}\xi^5_{\mathrm{ini}} \end{pmatrix}. \tag{F.26}$$

References

[1] E. W. Kolb and M. S. Turner, *The Early Universe*, vol. 69. 1990.

[2] V. Mukhanov, *Physical Foundations of Cosmology*. Cambridge University Press, Oxford, 2005.

[3] D. Baumann, *Inflation,* in *Theoretical Advanced Study Institute in Elementary Particle Physics: Physics of the Large and the Small*, pp. 523–686. 2011. arXiv:0907.5424 [hep-th].

[4] **Planck** Collaboration, N. Aghanim *et al.*, *Planck 2018 results. VI. Cosmological parameters*, *Astron. Astrophys.* **641** (2020) A6, arXiv:1807.06209 [astro-ph.CO]. [Erratum: Astron.Astrophys. 652, C4 (2021)].

[5] A. Neronov and I. Vovk, *Evidence for strong extragalactic magnetic fields from fermi observations of tev blazars*, *Science* **328** (2010) 73–75, arXiv:1006.3504 [astro-ph.HE].

[6] F. Tavecchio, G. Ghisellini, L. Foschini, G. Bonnoli, G. Ghirlanda, and P. Coppi, *The intergalactic magnetic field constrained by fermi/large area telescope observations of the tev blazar 1es0229+200*, *Monthly Notices of the Royal Astronomical Society: Letters* **406** (July, 2010) L70–L74, arXiv:1004.1329 [astro-ph.CO].

[7] S. Ando and A. Kusenko, *Evidence for gamma-ray halos around active galactic nuclei and the first measurement of intergalactic magnetic fields*, *Astrophysical Journal Letters* **722** (Oct., 2010) L39–L44, arXiv:1005.1924 [astro-ph.HE].

[8] F. Tavecchio, G. Ghisellini, G. Bonnoli, and L. Foschini, *Extreme tev blazars and the intergalactic magnetic field*, *Monthly Notices of the Royal Astronomical Society: Letters* **414** (July, 2011) 3566–3576, arXiv:1009.1048 [astro-ph.HE].

[9] K. Dolag, M. Kachelriess, S. Ostapchenko, and R. Tomàs, *Lower limit on the strength and filling factor of extragalactic magnetic fields*, *Astrophysical Journal Letters* **727** (Jan., 2011) L4, arXiv:1009.1782 [astro-ph.HE].

[10] W. Essey, S. Ando, and A. Kusenko, *Determination of intergalactic magnetic fields from gamma ray data*, *Astroparticle Physics* **35** (Oct., 2011) 135–139, arXiv:1012.5313 [astro-ph.HE].

[11] A. M. Taylor, I. Vovk, and A. Neronov, *Extragalactic magnetic fields constraints from simultaneous gev-tev observations of blazars*, *Astronomy & Astrophysics* **529** (May, 2011) A144, arXiv:1101.0932 [astro-ph.HE].

[12] C. D. Dermer, M. Cavadini, S. Razzaque, J. D. Finke, J. Chiang, and B. Lott, *Time delay of cascade radiation for tev blazars and the measurement of the intergalactic magnetic field*, *Astrophysical Journal Letters* **733** (June, 2011) L21, arXiv:1011.6660 [astro-ph.HE].

[13] I. Vovk, A. M. Taylor, D. Semikoz, and A. Neronov, *Fermi/lat observations of 1es 0229+200: Implications for extragalactic magnetic fields and background light*, *Astrophysical Journal Letters* **747** (Mar., 2012) L14, arXiv:1112.2534 [astro-ph.CO].

[14] K. Takahashi, M. Mori, K. Ichiki, S. Inoue, and H. Takami, *Lower bounds on magnetic fields in intergalactic voids from long-term gev-tev light curves of the blazar mrk 421*, *Astrophys. J. Lett.* **771** (2013) L42, arXiv:1303.3069 [astro-ph.CO].

[15] J. D. Finke, L. C. Reyes, M. Georganopoulos, K. Reynolds, M. Ajello, S. J. Fegan, and K. McCann, *Constraints on the intergalactic magnetic field with gamma-ray observations of blazars*, *Astrophysical Journal* **814** (Nov., 2015) 20, arXiv:1510.02485 [astro-ph.HE].

[16] M. Ackermann *et al.*, *The search for spatial extension in high-latitude sources detected by the fermi large area telescope*, *ApJS* **237** (2018) 32, arXiv:1804.08035 [astro-ph.HE].

[17] **MAGIC** Collaboration, V. A. Acciari *et al.*, *A lower bound on intergalactic magnetic fields from time variability of 1ES 0229+200 from MAGIC and Fermi/LAT observations*, *Astron. Astrophys.* **670** (2023) A145, arXiv:2210.03321 [astro-ph.HE].

[18] R. Alves Batista and A. Saveliev, *Multimessenger constraints on intergalactic magnetic fields from the flare of txs 0506+056*, *Astrophysical Journal Letters* **902** (Oct., 2020) L11, arXiv:2009.12161 [astro-ph.HE].

[19] K. Bondarenko, A. Boyarsky, A. Korochkin, A. Neronov, D. Semikoz, and A. Sokolenko, *Account of the baryonic feedback effect in γ-ray measurements of intergalactic magnetic fields*, *Astron. Astrophys.* **660** (2022) A80, arXiv:2106.02690 [astro-ph.CO].

[20] M. S. Turner and L. M. Widrow, *Inflation-produced, large-scale magnetic fields*, *Physical Review D* **37** (May, 1988) 2743–2754.

[21] B. Ratra, *Cosmological "seed" magnetic field from inflation*, *Astrophysical Journal Letters* **391** (May, 1992) L1.

[22] W. D. Garretson, G. B. Field, and S. M. Carroll, *Primordial magnetic fields from pseudo goldstone bosons*, *Physical Review D* **46** (Dec., 1992) 5346–5351, arXiv:hep-ph/9209238.

[23] C. J. Hogan, *Magnetohydrodynamic effects of a first-order cosmological phase transition*, *Phys. Rev. Lett.* **51** (Oct, 1983) 1488–1491.

[24] J. M. Quashnock, A. Loeb, and D. N. Spergel, *Magnetic field generation during the cosmological qcd phase transition*, *Astrophysical Journal Letters* **344** (Sept., 1989) L49.

[25] B. Cheng and A. V. Olinto, *Primordial magnetic fields generated in the quark-hadron transition*, *Phys. Rev. D* **50** (Aug, 1994) 2421–2424.

[26] T. Vachaspati, *Magnetic fields from cosmological phase transitions*, *Physics Letters B* **265** (Aug., 1991) 258–261.

[27] K. Kamada, F. Uchida, and J. Yokoyama, *Baryon isocurvature constraints on the primordial hypermagnetic fields*, *Journal of Cosmology and Astroparticle Physics* **2021** (2021) 034.

[28] K. Yanagihara, F. Uchida, T. Fujita, and S. Tsujikawa, *Low-Scale Inflationary Magnetogenesis without Baryon Isocurvature Problem*, arXiv:2312.07938 [astro-ph.CO].

[29] R. Banerjee and K. Jedamzik, *The evolution of cosmic magnetic fields: From the very early universe, to recombination, to the present*, *Phys. Rev. D* **70** (2004) 123003, arXiv:astro-ph/0410032.

[30] J. Zrake, *Inverse cascade of nonhelical magnetic turbulence in a relativistic fluid*, *Astrophysical Journal Letters* **794** (Oct., 2014) L26, arXiv:1407.5626 [astro-ph.HE].

[31] A. Brandenburg, T. Kahniashvili, and A. G. Tevzadze, *Nonhelical inverse transfer of a decaying turbulent magnetic field*, *Physical Review Letters* **114** (Feb., 2015) 075001, arXiv:1404.2238 [astro-ph.CO].

[32] M. Christensson, M. Hindmarsh, and A. Brandenburg, *Inverse cascade in decaying 3-D magnetohydrodynamic turbulence*, *Phys. Rev. E* **64** (2001) 056405, arXiv:astro-ph/0011321.

[33] A. Brandenburg and T. Kahniashvili, *Classes of hydrodynamic and magnetohydrodynamic turbulent decay*, *Phys. Rev. Lett.* **118** (2017) 055102, arXiv:1607.01360 [physics.flu-dyn].

[34] A. Brandenburg, T. Kahniashvili, S. Mandal, A. R. Pol, A. G. Tevzadze, and T. Vachaspati, *Evolution of hydromagnetic turbulence from the electroweak phase transition*, *Physical Review D* **96** (2017) 123528.

[35] J. Reppin and R. Banerjee, *Nonhelical turbulence and the inverse transfer of energy: A parameter study*, *Physical Review E* **96** (Nov., 2017) 053105, arXiv:1708.07717 [astro-ph.CO].

[36] K. Park, *On the inverse transfer of (non-)helical magnetic energy in a decaying magnetohydrodynamic turbulence*, *Monthly Notices of the Royal Astronomical Society: Letters* **472** (Dec., 2017) 1628–1640, arXiv:1709.06526 [physics.plasm-ph].

[37] D. N. Hosking and A. A. Schekochihin, *Reconnection-controlled decay of magnetohydrodynamic turbulence and the role of invariants*, *Phys. Rev. X* **11** (2021) 041005.

[38] L. Woltjer, *A Theorem on Force-Free Magnetic Fields*, *Proceedings of the National Academy of Science* **44** (June, 1958) 489–491.

[39] U. Frisch, A. Pouquet, J. Leorat, and A. Mazure, *Possibility of an inverse cascade of magnetic helicity in magnetohydrodynamic turbulence*, *Journal of Fluid Mechanics* **68** (Apr., 1975) 769–778.

[40] H. Zhou, R. Sharma, and A. Brandenburg, *Scaling of the saffman helicity integral in decaying magnetically-dominated turbulence*, *arXiv preprint arXiv:2206.07513* (2022) .

[41] A. Brandenburg and G. Larsson, *Turbulence with Magnetic Helicity That Is Absent on Average*, *Atmosphere* **14** (May, 2023) 932, arXiv:2305.08769 [physics.plasm-ph].

[42] A. Brandenburg, R. Sharma, and T. Vachaspati, *Inverse cascading for initial mhd turbulence spectra between saffman and batchelor*, *arXiv preprint arXiv:2307.04602* (2023) .

[43] D. N. Hosking and A. A. Schekochihin, *Cosmic-void observations reconciled with primordial magnetogenesis*, *arXiv preprint arXiv:2203.03573* (2022) , arXiv:2203.03573 [astro-ph.CO].

[44] F. Uchida, M. Fujiwara, K. Kamada, and J. Yokoyama, *New description of the scaling evolution of the cosmological magneto-hydrodynamic system*, *Phys. Lett. B* **843** (2023) 138002, arXiv:2212.14355 [astro-ph.CO].

[45] F. Uchida, M. Fujiwara, K. Kamada, and J. Yokoyama. in preperation.

[46] J. Sánchez Almeida and M. Martínez González, *Cosmic magnetic fields*,.

[47] M. Kawasaki, K. Kohri, and N. Sugiyama, *MeV scale reheating temperature and thermalization of neutrino background*, *Phys. Rev. D* **62** (2000) 023506, arXiv:astro-ph/0002127.

[48] M. Kawasaki, K. Kohri, and T. Moroi, *Big-Bang nucleosynthesis and hadronic decay of long-lived massive particles*, *Phys. Rev. D* **71** (2005) 083502, arXiv:astro-ph/0408426.

[49] R. Durrer and A. Neronov, *Cosmological magnetic fields: their generation, evolution and observation*, *The Astronomy and Astrophysics Review* **21** (2013) 1–109.

[50] K. Jedamzik, V. Katalinić, and A. V. Olinto, *Limit on Primordial Small-Scale Magnetic Fields from Cosmic Microwave Background Distortions*, *Physical Review Letters* **85** (July, 2000) 700–703, arXiv:astro-ph/9911100.

[51] K. Kamada and A. J. Long, *Baryogenesis from decaying magnetic helicity*, *Phys. Rev. D* **94** (2016) 063501, arXiv:1606.08891 [astro-ph.CO].

[52] K. Kamada and A. J. Long, *Evolution of the Baryon Asymmetry through the Electroweak Crossover in the Presence of a Helical Magnetic Field*, *Phys. Rev. D* **94** (2016) 123509, arXiv:1610.03074 [hep-ph].

[53] A. D. Sakharov, *Violation of CP Invariance, C asymmetry, and baryon asymmetry of the universe*, *Pisma Zh. Eksp. Teor. Fiz.* **5** (1967) 32–35.

[54] J. H. Applegate, C. J. Hogan, and R. J. Scherrer, *Cosmological Baryon Diffusion and Nucleosynthesis*, *Phys. Rev. D* **35** (1987) 1151–1160.

[55] K. Inomata, M. Kawasaki, A. Kusenko, and L. Yang, *Big Bang Nucleosynthesis Constraint on Baryonic Isocurvature Perturbations*, *JCAP* **12** (2018) 003, arXiv:1806.00123 [astro-ph.CO].

[56] R. Durrer and C. Caprini, *Primordial magnetic fields and causality*, *JCAP* **11** (2003) 010, arXiv:astro-ph/0305059.

[57] A. Brandenburg, K. Enqvist, and P. Olesen, *Large-scale magnetic fields from hydromagnetic turbulence in the very early universe*, *Phys. Rev. D* **54** (Jul, 1996) 1291–1300.

[58] H. K. Moffatt, *Magnetic field generation in electrically conducting fluids*, vol. 2. 1978.

[59] P. Olesen, *On inverse cascades in astrophysics*, *Phys. Lett. B* **398** (1997) 321–325, arXiv:astro-ph/9610154.

[60] D. Biskamp, *Nonlinear magnetohydrodynamics*. Cambridge University Press, 1993.

[61] A. Pouquet, U. Frisch, and J. Leorat, *Strong MHD helical turbulence and the nonlinear dynamo effect*, *Journal of Fluid Mechanics* **77** (Sept., 1976) 321–354.

[62] A. Llor, *Langevin equation of big structure dynamics in turbulence: Landau' s invariant in the decay of homogeneous isotropic turbulence*, *European Journal of Mechanics-B/Fluids* **30** (2011) 480–504.

[63] H. Alfvén, *Existence of Electromagnetic-Hydrodynamic Waves*, *Nature* **150** (Oct., 1942) 405–406.

[64] H. Alfvén, *On the Existence of Electromagnetic-Hydrodynamic Waves*, *Arkiv for Matematik, Astronomi och Fysik* **29B** (Jan., 1943) 1–7.

[65] H. K. Moffatt, *The degree of knottedness of tangled vortex lines*, *Journal of Fluid Mechanics* **35** (Jan., 1969) 117–129.

[66] J. J. Moreau, *Constantes d'un îlot tourbillonnaire en fluide parfait barotrope*, *Comptes rendus hebdomadaires des séances de l'Académie des sciences* **252** (1961) 2810–2812.

[67] R. J. Moreau, *Magnetohydrodynamics*, vol. 3. Springer Science & Business Media, 1990.

[68] J. P. Goedbloed and S. Poedts, *Principles of magnetohydrodynamics: with applications to laboratory and astrophysical plasmas*. Cambridge university press, 2004.

[69] S. Galtier, *Introduction to modern magnetohydrodynamics*. Cambridge University Press, 2016.

[70] M. A. Berger and G. B. Field, *The topological properties of magnetic helicity*, *Journal of Fluid Mechanics* **147** (Oct., 1984) 133–148.

[71] P. G. Saffman, *The large-scale structure of homogeneous turbulence*, *Journal of Fluid Mechanics* **27** (Jan., 1967) 581–593.

[72] L. F. Richardson, *Weather prediction by numerical process*. Cambridge University Press, 1922.

[73] P. A. Davidson, *On the decay of Saffman turbulence subject to rotation, stratification or an imposed magnetic field*, *Journal of Fluid Mechanics* **663** (Nov., 2010) 268–292.

[74] G. Birkhoff, *Fourier synthesis of homogeneous turbulence*, *Communications on Pure and Applied Mathematics* **7** (1954) 19–44.

[75] G. K. Batchelor and I. Proudman, *The Large-Scale Structure of Homogeneous Turbulence*, *Philosophical Transactions of the Royal Society of London Series A* **248** (Jan., 1956) 369–405.

[76] L. D. Landau and E. M. Lifshitz, *Fluid Mechanics*. 1987.

[77] P. A. Sweet, *The neutral point theory of solar flares*, *Electromagnetic phenomena in cosmical physics* **6** (1958) 123.

[78] E. N. Parker, *Sweet's mechanism for merging magnetic fields in conducting fluids*, *Journal of Geophysical Research* **62** (1957) 509–520.

[79] W. Park, D. A. Monticello, and R. B. White, *Reconnection rates of magnetic fields including the effects of viscosity*, *The Physics of fluids* **27** (1984) 137–149.

[80] H. Ji and W. Daughton, *Phase diagram for magnetic reconnection in heliophysical, astrophysical, and laboratory plasmas*, *Physics of Plasmas* **18** (2011) 111207.

[81] M. Christensson, M. Hindmarsh, and A. Brandenburg, *Scaling laws in decaying helical hydromagnetic turbulence*, *Astronomische Nachrichten* **326** (July, 2005) 393–399, arXiv:astro-ph/0209119.

[82] K. Jedamzik, V. Katalinic, and A. V. Olinto, *Damping of cosmic magnetic fields*, *Phys. Rev. D* **57** (1998) 3264–3284, arXiv:astro-ph/9606080.

[83] A. A. Schekochihin, *MHD Turbulence: A Biased Review*, arXiv:2010.00699 [physics.plasm-ph].

[84] D. Biskamp, *Magnetic reconnection via current sheets*, *Physics of Fluids* **29** (May, 1986) 1520–1531.

[85] N. F. Loureiro, S. C. Cowley, W. D. Dorland, M. G. Haines, and A. A. Schekochihin, *X-Point Collapse and Saturation in the Nonlinear Tearing Mode Reconnection*, *Physical Review Letters* **95** (Dec., 2005) 235003, arXiv:physics/0507206 [physics.plasm-ph].

[86] N. F. Loureiro, A. A. Schekochihin, and S. C. Cowley, *Instability of current sheets and formation of plasmoid chains*, *Physics of Plasmas* **14** (Oct., 2007) 100703–100703, arXiv:astro-ph/0703631.

[87] K. Shibata and S. Tanuma, *Plasmoid-induced-reconnection and fractal reconnection*, *Earth, Planets and Space* **53** (June, 2001) 473–482, arXiv:astro-ph/0101008.

[88] P. Bhat, M. Zhou, and N. F. Loureiro, *Inverse energy transfer in decaying, three-dimensional, non-helical magnetic turbulence due to magnetic reconnection*, *Monthly Notices of the Royal Astronomical Society: Letters* **501** (Feb., 2021) 3074–3087, arXiv:2007.07325 [astro-ph.CO].

[89] T. Fujita, K. Kamada, and Y. Nakai, *Gravitational Waves from Primordial Magnetic Fields via Photon-Graviton Conversion*, *Phys. Rev. D* **102** (2020) 103501, arXiv:2002.07548 [astro-ph.CO].

[90] S. I. Braginskii, *Transport Processes in a Plasma*, *Reviews of Plasma Physics* **1** (Jan., 1965) 205.

[91] P. Arnold, G. D. Moore, and L. G. Yaffe, *Transport coefficients in high temperature gauge theories (i): leading-log results*, *Journal of High Energy Physics* **2000** (2000) 001.

[92] S. Weinberg, *Entropy generation and the survival of protogalaxies in an expanding universe*, *Astrophys. J.* **168** (1971) 175.

[93] A. Heckler and C. J. Hogan, *Neutrino heat conduction and inhomogeneities in the early universe*, *Physical Review D* **47** (1993) 4256.

[94] D. E. Osterbrock, *On ambipolar diffusion in h i regions.*, *Astrophysical Journal* **134** (July, 1961) 270–272.

[95] F. A. Aharonian, P. S. Coppi, and H. J. Voelk, *Very high-energy gamma-rays from AGN: Cascading on the cosmic background radiation fields and the formation of pair halos*, *Astrophys. J. Lett.* **423** (1994) L5–L8, arXiv:astro-ph/9312045.

[96] A. Neronov and D. V. Semikoz, *A method of measurement of extragalactic magnetic fields by TeV gamma ray telescopes*, *JETP Lett.* **85** (2007) 473–477, arXiv:astro-ph/0604607.

[97] A. Elyiv, A. Neronov, and D. V. Semikoz, *Gamma-ray induced cascades and magnetic fields in intergalactic medium*, *Phys. Rev. D* **80** (2009) 023010, arXiv:0903.3649 [astro-ph.CO].

[98] A. Neronov and D. V. Semikoz, *Sensitivity of gamma-ray telescopes for detection of magnetic fields in intergalactic medium*, *Phys. Rev. D* **80** (2009) 123012, arXiv:0910.1920 [astro-ph.CO].

[99] K. Murase, K. Takahashi, S. Inoue, K. Ichiki, and S. Nagataki, *Probing Intergalactic Magnetic Fields in the GLAST Era through Pair Echo Emission from TeV Blazars*, *Astrophys. J. Lett.* **686** (2008) L67, arXiv:0806.2829 [astro-ph].

[100] R. Plaga, *Detecting intergalactic magnetic fields using time delays in pulses of γ-rays*, *Nature* **374** (1995) 430–432.

[101] K. Kajantie, M. Laine, K. Rummukainen, and M. E. Shaposhnikov, *A Nonperturbative analysis of the finite T phase transition in SU(2) x U(1) electroweak theory*, *Nucl. Phys. B* **493** (1997) 413–438, arXiv:hep-lat/9612006.

[102] J. Martin, C. Ringeval, and V. Vennin, *Encyclopædia Inflationaris*, *Phys. Dark Univ.* **5-6** (2014) 75–235, arXiv:1303.3787 [astro-ph.CO].

[103] D. H. Lyth, *MSSM inflation*, *JCAP* **04** (2007) 006, arXiv:hep-ph/0605283.

[104] A. Brandenburg, T. Kahniashvili, S. Mandal, A. Roper Pol, A. G. Tevzadze, and T. Vachaspati, *The dynamo effect in decaying helical turbulence*, *Phys. Rev. Fluids.* **4** (2019) 024608, arXiv:1710.01628 [physics.flu-dyn].